

# **Accelerating Jitter and BER Qualifications of High Speed Serial Communication Interfaces**

Yongquan Fan

Department of Electrical and Computer Engineering  
McGill University, Montreal

February 2010

---

A Thesis submitted to McGill University in partial fulfillment of the requirements for the degree of Doctor of Philosophy in Electrical Engineering

© Yongquan Fan, 2010

---

# Abstract

---

High-Speed Serial Interface (HSSI) devices have witnessed an increased use in communications. As a measure of how often bit errors happen, Bit Error Rate (BER) performance is of paramount importance in any communication interface. The bit errors in HSSIs are in large part due to jitter. This thesis investigates the topic of accelerating the jitter and BER testing and characterization [1].

The thesis first proposes a new algorithm, suitable for extrapolating the receiver jitter tolerance performance from higher BER regions down to the  $10^{-12}$  level or lower [2]. This algorithm enables us to perform the jitter tolerance characterization and production test more than 1000 times faster [3]. Then an under-sampling based transmitter test scheme is presented. The scheme can accurately extract the transmitter jitter and finish the whole transmitter test within 100ms [4] while the test usually takes seconds. All the receiver and transmitter testing schemes have been successfully used on Automatic Test Equipment (ATE) to qualify millions of HSSIs with speed up to 6 Gigabits per second (Gbps).

The thesis also presents an external loopback-based testing scheme, where a novel jitter injection technique is proposed using the state-of-the-art phase delay lines. The scheme can be applied to test HSSIs with data rate up to 12.5 Gbps. It is also suitable for multi-lane HSSI testing with a lower cost than pure ATE solutions. By using high-speed relays, we combine the proposed ATE based approaches and the loopback approach along with an FPGA-based BER tester to provide a more versatile scheme for HSSI post-silicon validation, testing and debugging [5]. In addition, we further explore the unparallel advantages of our digital Gaussian noise generator in low BER evaluation [6].

---

# Résumé

---

Les interfaces sérieelles à haute vitesse (interfaces HSSI) ont connu une utilisation accrue dans les télécommunications. Le taux d'erreur sur les bits (BER), mesure de la fréquence des erreurs, est d'une importance cruciale dans les interfaces modernes de télécommunication. Cette thèse traite de l'accélération de la caractérisation du vacillement et des tests BER.

Cette thèse propose tout d'abord un nouvel algorithme, approprié pour l'extrapolation de la performance de la tolérance au vacillement d'un récepteur pour un taux d'erreur sur les bits (BER) à un niveau de  $10^{-12}$  ou moins. Cet algorithme permet de caractériser la tolérance au vacillement dans les tests de production plus de 1000 fois plus rapidement. Ensuite, une conception de transmetteur à sous-échantillonnage est présentée. Cette conception permet d'extraire précisément le vacillement du transmetteur et de compléter les tests de ce dernier en moins de 100 ms alors que ces tests durent normalement plusieurs secondes. Toutes les méthodes de test de récepteurs et de transmetteurs ont été utilisées avec succès sur un équipement d'essai automatique (ATE) pour qualifier des millions d'interfaces HSSI à des vitesses allant jusqu'à 6 gigabits par seconde (6 Gbps).

Cette thèse présente aussi une conception de test en bouclage où une nouvelle méthode d'injection de vacillement est proposée en utilisant des lignes de délai de phase. Cette méthode peut être appliquée pour tester des interfaces HSSI avec un taux de transfert allant jusqu'à 12.5 Gbps. Elle permet aussi de tester des interfaces HSSI multi-lignes à un coût moindre qu'une solution utilisant un ATE. En utilisant des relais à haute vitesse, les approches sur ATE et par test en bouclage peuvent être combinées en incorporant un testeur de BER sur circuit intégré prédéfini programmable (FPGA), ce qui permet une méthode de tests HSSI polyvalente pour la validation post-fabrication, les tests et le

débogage. Finalement, nous explorons les avantages de notre générateur de bruit Gaussien dans l'évaluation de BER à bas niveau.

---

# Acknowledgments

---

First and foremost, I would like to thank my supervisor, Professor Zeljko Zilic. His guidance, encouragement and support throughout the research are greatly appreciated. He is highly insightful in directing the academic research to solve current challenges in the industry. His guidance and help in preparing my thesis, papers and presentations are especially appreciated. I am truly fortunate to have such an excellent supervisor.

I also would like to thank my former co-supervisor, Dr. Yi Cai, for his support in the research. As a renowned expert in high-speed testing, he provided me with invaluable guidance and support in establishing research topics and publishing two papers. My thanks also go to Liming Fang, Anant Verma, Bill Burcanowski, and Sandeep Kumar for co-authoring one paper. I also appreciate the technical support and help from the whole PHY and Storage team at Agere/LSI, especially from Angshu Bhattacharyya, Joe Martone, John Janney, Suri Basharapandiyani, Bernhard Lanchiski, Tom Gibson, Kahn Neguen, Bob Hein and Ken Paist.

In addition, I thank the many people who have given me valuable advice and feedback at conferences and various occasions. Special thanks are extended to Gordon Roberts and Warren Gross at McGill University, Mohamed Hafed at DFT Microsystems, Yang Liang at Maxim, Steve Sunter at Logic Vision, Mike Li at Wavecrest and Xu Fang at Teradyne. Also, I would like to thank students in the MACS lab who have helped me with the research. In particular, I thank Jean-Samuel Chenard for translating the thesis abstract into French.

Last but not least, I would like to thank my whole family, especially my wife Ji Lei, for their love and support over the years.

---

# Table of Contents

---

<b>Abstract.....</b>	<b>i</b>
<b>Résumé.....</b>	<b>ii</b>
<b>Acknowledgments .....</b>	<b>iv</b>
<b>Table of Contents .....</b>	<b>v</b>
<b>List of Figures .....</b>	<b>ix</b>
<b>List of Tables .....</b>	<b>xiii</b>
<b>List of Acronyms.....</b>	<b>xiv</b>
<b>Chapter 1 - Introduction.....</b>	<b>1</b>
1.1 Motivation.....	1
1.1.1 HSSI Technology Trends .....	3
1.1.2 Qualification Challenges .....	5
1.1.3 ATE Perspectives .....	7
1.2 Contributions .....	9
1.3 Overview of the Thesis .....	11
<b>Chapter 2 - Background.....</b>	<b>12</b>
2.1. High-Speed Serial Communication .....	12
2.1.1 HSSI Structure .....	16
2.1.2 CDR Characteristics .....	17
2.1.3 BER Mechanisms.....	23
2.1.4 Jitter and Noise Impacts to BER .....	27
2.2 Timing Jitter.....	29
2.2.1 Jitter Overview .....	29
2.2.2 Jitter and BER .....	31

2.2.3 Jitter Testing and Jitter Injection.....	34
<b>2.3 Amplitude Noise .....</b>	<b>37</b>
2.3.1 BER and SNR .....	38
2.3.2 Simulation and Emulation.....	43
2.3.3 AWGN Emulation.....	45
<b>Chapter 3 – Accelerating Receiver Jitter Tolerance Testing on ATE....</b>	<b>49</b>
3.1 Introduction.....	49
3.1.1 Jitter Tolerance Testing.....	49
3.1.2 Proposed New Method.....	51
3.2 Jitter Test Signal Generation .....	56
3.2.1 Choosing Test Signal Parameters.....	57
3.2.2 Periodic Jitter Injection .....	60
3.2.2.1 Creating Jitter-Free Data Signal.....	60
3.2.2.2 Creating a Digitized Jitter Signal.....	61
3.2.2.3 Modulating the Data Signal .....	62
3.2.2.4 Generating Bandwidth Limited Signals.....	63
3.2.2.5 Downsampling to Get AWG Samples .....	65
3.2.3 Fractional Sampling .....	66
3.2.4 Jitter Calibration.....	67
3.2.5 Random Jitter Control .....	71
3.3 Receiver Bit Error Monitoring .....	72
3.3.1 ATE-based Error Detection.....	72
3.3.2 DFT-based Error Detection.....	74
3.4 Jitter Tolerance Extrapolation.....	76
3.4.1 Jitter Tolerance Extrapolation Algorithm .....	76
3.4.2 Accelerating Jitter Tolerance Characterization.....	80
3.4.3 Accelerating Jitter Tolerance Compliance Testing.....	86
3.4.4 Discussions.....	88
<b>Chapter 4 – Transmitter Jitter Extraction on ATE.....</b>	<b>90</b>
4.1 Introduction.....	90

4.1.1 Transmitter Jitter Testing Overview .....	90
4.1.2 Proposed Solution .....	92
4.2. Test Setup for Data Acquisition .....	93
4.2.1 Overview of the Test Setup.....	93
4.2.2 Principles of Clock Settings .....	94
4.2.3 Test Setting Parameter Calculations .....	97
4.3. Jitter Extraction.....	101
4.3.1 Generating Edge Displacement.....	101
4.3.2 Time Domain Approach.....	104
4.3.2.1 RJ Extraction.....	105
4.3.2.2 DJ Extraction .....	106
4.3.2.4 TJ Calculation .....	107
4.3.3 Frequency Domain Approach .....	110
4.3.3.1 RJ Extraction.....	110
4.3.3.2 DJ Extraction .....	112
4.3.4 Hybrid Approach.....	113
4.3.5 Limitations of Each Approach .....	115
4.4 Experimental Results .....	116
4.4.1 Bench Correlation .....	116
4.4.2 Correlating Two RJ Approaches.....	117
4.4.3 Impact of Test Patterns.....	119
4.4.4 Impact of the Reference Clock.....	120
4.4.5 Extending to 6 Gbps Applications .....	122
4.5 Summary .....	123
<b>Chapter 5 – Testing HSSIs with or without ATE Instruments.....</b>	<b>125</b>
5.1 FPGA-based Bit Error Detection.....	126
5.1.1 Implementing a Serial BERT .....	127
5.1.2 Implementing a Parallel BERT .....	128
5.1.3. HSSI Testing Demonstration .....	129
5.2 Loopback Testing with Jitter Injection.....	131



5.2.1 Testing Setup.....	131
5.2.2 Phase Delay Based jitter Injection .....	133
5.2.3 Experimental Results .....	136
5.3 A Versatile HSSI Testing Scheme.....	139
5.3.1 Major Functions of our Setup .....	140
5.3.2 High Speed Relays .....	143
5.3.3 Limitations and Further Considerations.....	148
5.4 BER Testing Under Noise .....	149
5.4.1 Our AWGN Generator .....	150
5.4.1.1 Hardware Implementation .....	150
5.4.1.2 Statistical Properties.....	152
5.4.2 BER Testing Demonstration .....	154
5.4.3 Advantages of Our AWGN Generator .....	158
<b>Chapter 6 – Conclusions and Future Work.....</b>	<b>161</b>
6.1 Conclusions.....	161
6.2 Future Investigations .....	163
6.2.1 PLL and CDR Characteristics Analysis .....	163
6.2.2 Further Phase Delay Line Performance Evaluation .....	166
6.2.3 AWGN Generator Implementation .....	167
<b>References.....</b>	<b>168</b>

---

# List of Figures

---

<b>Figure 1-1:</b> HSSIs in communication infrastructure.....	3
Figure 1-2: High speed serial interface technology trend.....	8
<b>Figure 2-1:</b> CDR transmission mechanism.....	12
Figure 2-2: Applications of multiple HSSIs .....	13
Figure 2-3: Current-mode LVDS driver .....	14
Figure 2-4: Block diagram of an HSSI .....	16
Figure 2-5: Block diagram of the CDR with a typical linear PLL.....	18
Figure 2-6: Phase transfer characteristics of the PLL .....	19
Figure 2-7: Jitter transfer function of the receiver .....	19
Figure 2-8: BBPD PLL sampling .....	20
Figure 2-9: First order model of a BBPD PLL .....	21
Figure 2-10: Graph of the binomial distribution ( $n = 10^8$ , $p = 10^{-7}$ ) .....	25
Figure 2-11: Test time vs. BER confidence level .....	27
Figure 2-12: Ideal digital signal.....	28
Figure 2-13: Timing and amplitude deviations in an actual data signal. ....	28
<b>Figure 2-14:</b> Jitter components .....	30
Figure 2-15: Jitter and BER in the receiver .....	32
Figure 2-16: AWGN channel model.....	38
Figure 2-17: Binary matched filter receiver.....	39
Figure 2-18: Probability densities of $y$ .....	41
Figure 2-19: BER vs. SNR for baseband transmission.....	43
Figure 3-1: Jitter tolerance specifications .....	50
Figure 3-2: Conceptual illustration of the jitter tolerance extrapolation.....	51
Figure 3-3: Transmitter BER scan .....	52
Figure 3-4: Receiver BER scan.....	54

Figure 3-5: Jitter PDFs for curve fitting .....	55
Figure 3-6: Test setup for jitter tolerance testing.....	55
Figure 3-7: The 128-PRBS sequence.....	58
Figure 3-8: Oversampled jitter-free data signal .....	61
Figure 3-9: Jitter signal and modulated data signal .....	63
Figure 3-10: Adding edge transition time.....	64
Figure 3-11: Frequency spectrum of the oversampled data signal .....	64
Figure 3-12: Time domain data after the inverse FFT .....	65
Figure 3-13: AWG waveform – data after under-sampling.....	65
Figure 3-14: The eye diagram of the AWG samples with 300ps PJ injected.....	68
Figure 3-15: Test setup for jitter calibration on ATE .....	69
Figure 3-16: Jitter injection calibration curves with the digitizer.....	70
Figure 3-17: Jitter injection calibration curves with Wavecrest SIA-3000 .....	70
Figure 3-18: RJ vs. AWG output amplitude .....	71
Figure 3-19: ATE-based BERT .....	73
Figure 3-20: Pattern alignment between the serial data and the parallel data .....	74
Figure 3-21: Conceptual illustration of the DFT-based BERT.....	75
Figure 3-22: Overview of the jitter tolerance extrapolation .....	76
Figure 3-23: Jitter sources to the CDR .....	77
Figure 3-24: Linear regression of Q factor as a function of the injected PJ .....	81
Figure 3-25: A comparison between the two fitting results.....	81
Figure 3-26: A comparison of BER curve fitting results.....	82
Figure 3-27: Bathtub curve prediction.....	83
Figure 3-28: 3Gbps test signal calibration results.....	84
Figure 3-29: Q factor vs. PJ .....	85
Figure 3-30: BER extrapolation.....	85
Figure 3-31: The offset between PJ and TJ at different testers.....	87
Figure 4-1: Transmitter test setup for data acquisition .....	93
Figure 4-2: Captured transmitter output signal .....	101
Figure 4-3: Actual edge transitions and curve fitting .....	102
Figure 4-4: Derived edge positions from curve fitting .....	102

Figure 4-5: Edge displacement data after interpolation.....	103
Figure 4-6: One cycle of the test pattern.....	104
Figure 4-7: Histograms and DJ of all eight edges.....	105
Figure 4-8: The PDF and CDF of the device TJ.....	109
Figure 4-9: TJ spectrum.....	110
Figure 4-10: RJ spectrum.....	111
Figure 4-11: Histograms with low frequency DJ: SD = 4.08Ps .....	114
Figure 4-12: Histograms after removing low frequency DJ: RJ = SD = 1.70Ps .....	114
Figure 4-13: DJ leakage.....	115
Figure 4-14: RJ repeatability and correlation .....	118
Figure 4-15: Jitter distribution across PVT corners.....	119
Figure 4-16: Captured 6G waveform (only 45 bits shown).....	122
Figure 4-17: RJ and DJ at 6G data rate.....	123
Figure 5-1: Block diagram of a serial BERT .....	127
Figure 5-2: Block diagram of the parallel BERT.....	129
Figure 5-3: HSSI testing setup to verify BERT functionality .....	130
Figure 5-4: Loopback-based jitter testing.....	132
Figure 5-5: Block diagram of iT4036 .....	134
Figure 5-6: Delay vs. delay control.....	135
Figure 5-7: RJ degradation vs. Vcm (courtesy of GigOptix).....	135
Figure 5-8: Phase delay line iT4036 evaluation board (courtesy of GigOptix).....	136
Figure 5-9: Phase delay evaluation setup.....	136
Figure 5-10: The transmitter output waveform after the delay line.....	137
Figure 5-11: Extracted DJ profile from captured data signal. ....	137
Figure 5-12: Extracted DJ from the phase delay output .....	138
Figure 5-13: A versatile scheme for HSSI validation and test.....	139
Figure 5-14: Testing HSSIs on ATE.....	140
Figure 5-15: Characterizing the relay and the phase delay using the digitizer .....	141
Figure 5-16: Characterizing the relay using the digitizer .....	142
<b>Figure 5-17: TT1244 functional block diagram .....</b>	<b>143</b>
Figure 5-18: TT1244 measured performance by TeraVicta .....	144

Figure 5-19: Charge-pump circuit for the MEMS .....	145
Figure 5-20: GRF300 relay (Courtesy of Teledyne).....	146
Figure 5-21: Typical signal integrity performance at 10Gbps (courtesy of Teledyne) ...	146
Figure 5-22: GRF300 relay evaluation setup.....	147
Figure 5-23: Captured waveforms on ATE .....	147
Figure 5-24: Block diagram of the Polar method .....	151
Figure 5-25: Our CLT method ( $N=4$ ) .....	151
Figure 5-26: Setup of testing BER under noise .....	155
Figure 5-27: BER testing setup for digital baseband transmission.....	155
Figure 5-28: Measured BER vs. theoretical BER.....	157
Figure 6-1: Test setup for the PLL jitter transfer characterization .....	164
Figure 6-2: Measured PLL jitter transfer characteristics .....	164
Figure 6-3: Jitter tolerance frequency response .....	165

---

# List of Tables

---

Table 2-1: SATA Physical Layer General Specifications [22].....	15
Table 2-2: VCO Judgments in BBPD PLL.....	20
Table 2-3: An Example of BER Estimation ( $CL=99\%$ and $p=10^{-10}$ ).....	26
Table 2-4: Transmitter Jitter Specifications for SATA.....	31
Table 2-5: Receiver Jitter Tolerance Specifications for SATA.....	31
Table 3-1: High BER Data for Jitter Tolerance Extrapolation .....	84
Table 4-1: Transmitter Jitter Specifications for SATA Gen2 .....	91
Table 4-2: Parameter Settings for 20-bit Pattern 3Gbps Data Capture.....	98
Table 4-3: Actual Clock Frequencies for the 3Gbps Data Application .....	99
Table 4-4: Parameter Settings for 6Gbps Data Capture.....	99
Table 4-5: Parameter Settings for 5.5Gbps Data Capture.....	100
Table 4-6: RJ and DJ Values in Figure 4-7.....	107
Table 4-7: Jitter Measurement Results between ATE and Bench .....	117
Table 4-8: Jitter Measurement Results Using Different Test Patterns .....	120
Table 4-9: Reference Clock Impacts to Transmitter Jitter Measurement. ....	121
Table 5-1: 6Gbps Signal Parameters in Different Signal Paths.....	148
Table 5-2: $Q(x)$ Relative Error of Our Generators.....	153
Table 5-3: BER Measurements for Digital Baseband.....	156

---

# List of Acronyms

---

AC: Alternating Current

A-D: Anderson-Darling

ADC: Analog to Digital Converter

ATE: Automatic Test Equipment

AWG: Arbitrary Waveform Generator

AWGN: Additive White Gaussian Noise

BBPD: Bang Bang Phase Detector

BER: Bit Error Rate

BERT: Bit Error Rate Tester

BIST: Built-in-Self-Test

BUJ: Bounded Uncorrelated Jitter

CDF: Cumulative Distribution Function

CDR: Clock Data Recovery

CL: Confidence Level

CMOS: Complementary Metal-Oxide Semiconductor

CTL: Central Limit Theorem

DAC: Digital Analogy Converter

DCD: Duty Cycle Distortion

DDJ: Data Dependant Jitter

DFT: Design-For-Test

DJ: Deterministic Jitter

DSP: Digital Signal Processing

DUT: Device Under Test

ECL: Emitter Coupled Logic

FC: Fiber Channel

FFT: Fast Fourier Transform

FIFO: First-In-First-Out  
FM: Frequency Modulation  
FPGA: Field Programmable Gate Array  
Gbps: Gigabits per second  
HBT: Heterostructure Bipolar Transistor  
HSD: High Speed Digital  
HSSI: High Speed Serial Interface  
I/O: Input/Output  
ISI: Inter-Symbol Interference  
K-S: Kolmogorov-Smirnov  
LF: Loop Filter  
LFSR: Linear Feedback Shift Register  
LSB: Least Significant Bit  
LVDS: Low Voltage Differential Signaling  
MEMS: Micro-Electro-Mechanical System  
MSB: Most Significant Bit  
NRZ: Non Return Zero  
NRZI: Non Return Zero Inverted  
OE: Output Enabled  
OOB: Out of Band  
ORC: Optical Reference Clock  
PCB: Printed Circuit Board  
PDF: Probability Distribution Function  
PFD: Phase Frequency Detector  
PJ: Periodic Jitter  
PLL: Phase Lock Loop  
PRBS: Pseudo Random Bit Sequence  
PRWS: Pseudo Random Word Sequence  
PVT: Process, Voltage and Temperature  
RAM: Random Access Memory  
RJ: Random Jitter



RO: Ring Oscillator  
ROM: Read Only Memory  
Rx: Receiver  
RZ: Return Zero  
SAS: Serial Attached SCSI  
SATA: Serial Advanced Technology Attachment  
SCSI: Small Computer System Interface  
SD: Standard Deviation  
SerDes: Serializer Deserializer  
SMA: Sub-Miniature type-A  
SNR: Signal-to-Noise Ratio  
SoC: System-on-Chip  
TIA: Time Interval Analysis  
TJ: Total Jitter  
Tx: Transmitter  
UI: Unit Interval  
VCDL: Voltage-Controlled Delay Line  
VCO: Voltage-Controlled Oscillator  
VHDL: VHSIC Hardware Description Language  
VHSIC: Very High Speed Integrated Circuit  
XAUI: 10 Gigabit Attached Unit Interface

---

# Chapter 1 - Introduction

---

## 1.1 Motivation

The High-Speed Serial Interface (HSSI), which is interchangeably referred to as Serializer/Deserializer (SerDes) or transceiver, is a cornerstone of modern communication. As the HSSI data rate reaches a few Gbps and continues increasing, the room for its timing deviation, i.e., jitter, is getting tighter and tighter. To achieve high data rates, sophisticated techniques such as equalization and pre-compensation have now become common in HSSIs. With the concurrent increase in design complexity and decrease in the timing budget, the traditional “Guaranteed by Design” paradigm is not valid anymore. It is becoming imperative to qualify the tight timing specifications in silicon in order to guarantee the design quality.

The post-silicon qualification usually consists of three processes: validation of the first set of fabricated devices, characterization of the devices under all settings across Process, Voltage and Temperature (PVT) corners, and production testing. *Validation* emphasizes on verifying complete device functionality, including parameter values and electrical characteristics. Because of the increasing design complexity, close to 25% of all design resources at Intel are now spent on post-silicon validation [20]. Validation is usually performed in a lab environment, where standard instruments, such as oscilloscopes, signal generators and logic analyzers are used. The standard equipment is also referred to as *bench* equipment, and the standard equipment based validation and testing approaches are also referred to as bench solutions. *Characterization* is more concentrating on verifying that the device can work under all settings and can accommodate process variations allowed in manufacturing. Characterization can be done either in the lab or on Automatic Test Equipment (ATE). *Production* testing determines the pass/fail of each device in a

mass production environment. Throughput is paramount in production testing because it directly affects the device cost. ATE is widely used in production because of its high throughput.

Among all the HSSI parameters that we need to qualify, BER and Jitter are critical specifications. *BER* is the bit error probability of the system, which shows how well the system works. *Jitter* is the deviation of a signal from its ideal timing. It usually is expressed relative to the clock signal, where such deviations can cause bits to be incorrectly latched. In data communications, we usually talk about bit errors caused by jitter. Jitter specifications are normally defined at  $10^{-12}$  BER or lower. It is very challenging and costly to qualify the timing specification mainly for three reasons:

- (1) ATE has been widely used in production testing because of its high throughput. However, the increasing demand for more bandwidth is continuously pushing the data communication rate higher, at a pace faster than the test equipment evolves; systematic HSSI testing solutions on ATE for data rates above 6 Gbps are not commercially mature yet [8].
- (2) Cost goals set by the marketplace demand competitive test solutions – testing needs to be done as fast as possible using as inexpensive equipment as possible; it is infeasible to use traditional lab instruments in a production environment because it takes hours or even days to qualify the jitter and BER performance.
- (3) Validating the jitter performance across PVT corners is becoming necessary with the continuing scale of the process technology, but the validation is very time-consuming; shortening the validation time (including debugging when necessary) would directly reduce the time-to-market, which provides great competitive advantages in gaining profit and market share.

Motivated by the great economic significance in qualifying HSSIs, this research concentrates on developing HSSI test and characterization methodologies to address the above challenges. We aim to qualify HSSIs accurately and cost-effectively, yet overcoming ATE limitations.

### 1.1.1 HSSI Technology Trends

With the evolution of information technology during the past few decades, commodities such as cell phones and computers have become commonplace. They have made it a reality for people all over the world to share information or communicate directly in one way or another. This evolution has caused a drastic increase in the amount of information generated and the number of end users that need to access the information. As a platform to communicate information, Internet has become the main driver for technology innovation and bandwidth growth. The key to meeting the increasing demand for bandwidth is the HSSI.

Figure 1-1 illustrates the structure of an Ethernet-based communication infrastructure. In this network, HSSIs are widely adopted into backplane applications, short and long-haul communications, mass storage access networking, and computer peripherals. The bandwidth requirement of the HSSIs depends on the proximity to the end-user and the location in the network. Different serial communication protocols have arisen to address different applications, such as Ethernet, XAUI, GPON and SATA.

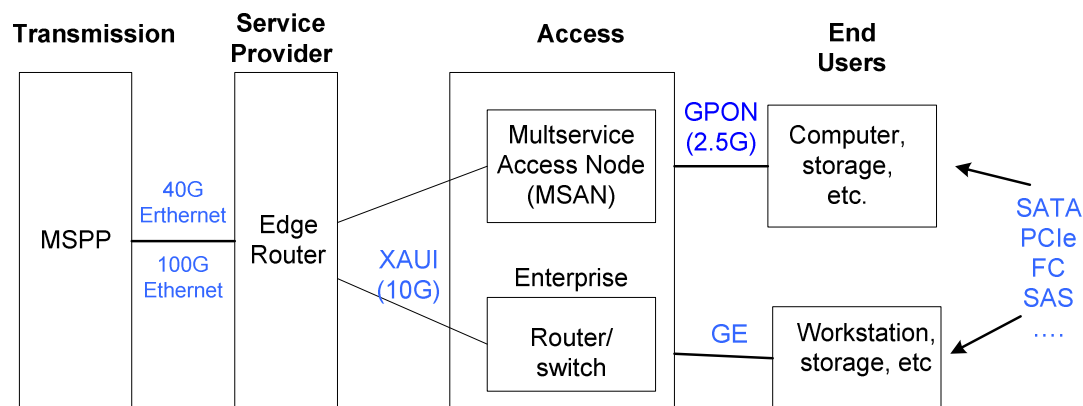


**Figure 1-1:** HSSIs in communication infrastructure

The HSSI protocols are continuously evolving to higher speeds to meet the demand for higher bandwidth. One example is the Serial ATA (SATA): when the SATA 1.0 Working

Group was formed in February 2000 to design SATA for desktops, the target speed was only 1.5Gps; in 2004 it evolved to 3Gps and now SATA 3.0 provides 6Gbps data rate [22]. Another example is the Ethernet: 10Gbps Ethernet (10GbE) was first published by IEEE in 2002 [9]. Currently it is the fastest matured standard, but IEEE is already in development of 40GbE and 100GbE.

The increasing bandwidth requirements are driving silicon vendors to provide HSSIs with higher speeds. In 2002, the highest data rate in Altera Field Programmable Gate Arrays (FPGAs) was only 1.25 Gbps per channel, available in its Mercury devices [10]; now in Altera Stratix IV GT FPGAs, the rate has increased to 11.3 Gbps per channel, with up to 48 transceivers each device [11]. Another major FPGA provider, Xilinx, provides up to thirty-six 11.2 Gbps transceivers in its Virtex-6 and Spartan-6 FPGAs, capable of supporting 40G/100G applications [12].

The increase in data rate and integration in FPGAs is just a snapshot of the trend in the whole semiconductor industry. Moore's law is still driving the industry to double the number of transistors in an integrated device every two years, making it possible to integrate more functions and provide higher performance. The aggressive scaling in deep submicron technologies has enabled the System-on-Chip (SoC) integration of a microcontroller/DSP, ADC/DAC, memory blocks, power management, PLL and external interfaces. Many Giga-Hertz serial interfaces are built in SoC type devices with CMOS process. The data rate of the interfaces also scales accordingly. Besides the FPGA providers, some other semiconductor companies have developed HSSIs with data rates up to 10Gbps per channel, and with up to 100 channels per device [13], [14]. It has been a trend to put more and faster HSSIs in a single device to meet the increasing bandwidth demand.

When we keep pushing the speed envelope and increase the integration, many signal integrity related issues arise, such as timing jitter, noise and frequency loss. A few key technologies have been developed recently to address the issues [15]. Pre-emphasis and equalization techniques are used to compensate frequency-related losses, especially those

related to Printed Circuit Board (PCB) design due to the skin effect and dielectric loss [16]. Pre-emphasis is used in the transmitter to boost the high-frequency components of a data signal before it is launched to the transmission medium. Equalization in the receiver acts as a high-pass filter to the data signal when it enters the receiver and re-shapes the signal in order to interpret the received signal correctly.

With the integration increase, there is a trend to implement multiple data rates in a single HSSI to accommodate multiple protocols. This requires the HSSI capable of providing multiple rate clock signals. The Phase Locked Loop (PLL) is widely used for clock generation, where a Voltage-Controlled Oscillator (VCO) is a key component. There are two types of oscillators: Ring Oscillator (RO) and LC tank oscillator (LC tank). RO has the advantages of small chip area and wide tunable frequency range, but LC tanks provide lower noise and better jitter performance [17], [18]. Multiple data rates can be implemented by changing divider ratios inside the PLL or by providing additional VCOs. In Altera Stratix IV GT FPGAs, the RO can support data rates from 600Mbps to 10.3 Gbps; two LC tanks are also implemented in this device, one with 4.9~6.375 Gbps optimized for PCIe/CEI-6 compliance and the other with 9.9~11.3 Gbps optimized for XLAUI/CAUI/CEI-11G compliance [19].

A side effect of implementing multiple data rates is that the jitter performance of the HSSI can vary across its data range. If the same PLL is used at two speeds, such as 6Gbps and 8.5Gbps, one speed can be susceptible to higher jitter because the two speeds are derived from the same VCO that can only be optimized at one speed. If different PLLs are used to support different data rates, the performance at one data rate does not correlate to another data rate. In either case, good performance at a higher data rate does not guarantee better margin at lower data rates because PLL characteristics may be different.

### **1.1.2 Qualification Challenges**

With the increasing data rate and higher degree of integration, the staggering complexity makes it challenging to design fault-free devices. Post-silicon qualifications are critical in

guaranteeing the design quality and the device quality. It is challenging and expensive to qualify the HSSI devices, especially the jitter performance – transmitter jitter and receiver jitter tolerance. Numerous HSSI standards define jitter performance at the  $10^{-12}$  BER level, which requires running at least  $10^{13}$  bits. This requirement fundamentally limits the test speed: for instance, at 3Gbps data rate, it takes around one hour to run so many bits. With some emerging applications demanding  $10^{-14}$  BER, direct measurements are even further from being practical.

In addition, many settings in the HSSI may affect its jitter performance. A few examples include the boost control settings in the equalizer, the bandwidth setting in the PLL and the driver strength settings in the transmitter. These settings are quite common in today's HSSIs. Choosing the optimal setting for the whole HSSI from hundreds or even thousands of available settings is challenging. It requires a tremendous amount of resources in validation and test in order to guarantee the device quality.

Because of the long test time, traditionally the jitter performance of multi-gigabit HSSI devices is only evaluated on bench in limited combinations of PVT. Besides the long test time, another reason that jitter is not qualified in production is the limited availability of ATE instruments, especially for very high-speed applications. For example, to evaluate 8.5GHz FC devices, we prefer the signal generator for the receiver and the digitizer for the transmitter with a bandwidth much higher than 8.5G (such as 15GHz), but they are not commercially mature yet on ATE [8]. Furthermore, there are currently no systematic ATE solutions that can perform complete HSSI testing accurately and cost-efficiently. Most companies only do loopback tests in production to check the functionality. Some HSSI parameters, such as transmitter jitter and receiver jitter tolerance, are assumed to be guaranteed by design.

Unfortunately, the “Guaranteed by Design” quality paradigm is no longer valid while we keep advancing the semiconductor technology and increasing the data rate, which results in tightening the jitter specifications. The devices can increasingly fail just because they do not comply with the specifications. According to the data by Collett International, the

timing, mixed-signal interfaces, clocking and crosstalk are among the prime failure reasons, each contributing 18% or more to the failure of the first silicon. HSSIs personify all such issues, and are hence critical to achieving the overall system quality. It therefore is becoming imperative to develop systematic HSSI compliance testing solutions on ATE to distinguish bad devices from good ones in production. This is the only way to ensure the device quality and to eliminate or reduce customer returns.

Besides the production testing, ATE is also becoming more and more popular in characterization and validation due to its high throughput. A thorough validation and characterization of a design requires performing measurements on different process materials at different temperature and voltage combinations. All these combinations may lead to measure the same parameter more than 100 times on one device in order to get its characteristics under different conditions. The traditional bench validation approach can no longer meet the requirement of measuring a large amount of parameters in a short time. ATE-based characterization and validation solutions have to be employed to meet the requirement. Our aim is to develop systematic HSSI testing solutions on ATE that can measure the HSSI standard parameters and design specifications for validation and characterization purposes. To achieve the best test economy, we use a simplified test flow in production to qualify key parameters only.

### **1.1.3 ATE Perspectives**

In general, ATE can provide high throughput and has been widely used in production test. It is also more and more widely use for validation and characterization to shorten the time-to-market. To validate, characterize and test HSSIs on ATE, there are several considerations that need to be addressed.

The first concern is the test cost. In early days, HSSI devices were designed as high-performance and high-margin devices. With the introduction of the low cost CMOS processes, most of the Gigahertz HSSIs are now built in high-volume and low-priced SoCs. The large scale integration makes it challenging to design a high performance HSSI



block in a very noisy SoC environment. It is more challenging to provide competitive production test solution because of the test time budget. For an average high-volume SoC, the normal acceptable test time ranges from a few seconds to ten seconds. The HSSI testing is tied with the testing of all other analog and digital blocks in the SoC. As one of many blocks in an SoC, it is expected that the HSSI block testing can be done within 1~2 seconds. For transmitter jitter testing and the receiver jitter tolerance testing, the test time budget is usually limited to a few tens or hundreds milliseconds because there are hundreds of other parameters to test. Test cost control is one of the biggest challenges in a mass-production environment. It is urgent to develop jitter testing techniques that can meet the cost requirement.

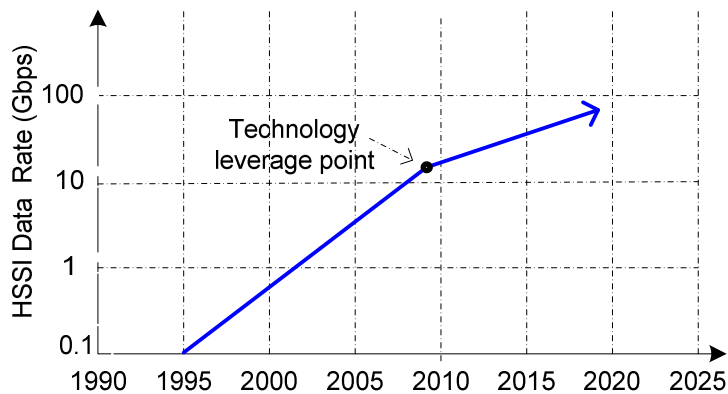


**Figure 1-2:** High speed serial interface technology trend

The second concern is the availability of high-speed instruments on ATE. The increasing bandwidth demand has been pushing the HSSI data rate higher and higher. Figure 1-2 illustrates the historic technology points and future trends [8]. During the past ten years, the data rate has increased from around 1Gbps to the 10 Gbps range. The HSSI I/O frequency is growing faster than the packaging and test fixture technology. Because of the physical limits due to the packaging and test socket, the data rate may slow down somewhat beyond 13 Gbps, shown as the technology leverage point in Figure 1-2 [8]. During the past few years, the ATE industry has made significant progress in providing HSSI test solutions. Several ATE suppliers have provided production pin-card solutions up to 6Gbps. For higher speed, such as 8.5Gbps and 10Gbps applications, systematic

ATE production solutions with jitter testing are not commercially mature yet. Normally only loopback testing is implemented in production to provide limited coverage. It is therefore imperative to address the ATE limitations in order to provide systematic production test solutions for applications above 6Gbps. Another ATE limitation is in multi-lane HSSI testing; most ATE platforms do not have enough high-speed instruments to accommodate the testing of multi-lane HSSI devices.

The third challenge is jitter decomposition and jitter injection. Many HSSI standards specify the jitter specifications in term of Deterministic Jitter (DJ) and Random Jitter (RJ). The traditional concept of histogram based peak-to-peak jitter has been replaced by the concept of Total Jitter (TJ), which is related to a certain BER level. Jitter test solutions need to be capable of decomposing TJ to DJ and RJ. In addition, uncorrelated jitter detection is also needed because it can fail the device in real applications but some jitter measurement techniques cannot detect it. To conduct a jitter tolerance test for the receiver, we need to have instruments that can deliberately inject controllable amounts of jitter. Depending on applications, we may need to inject PJ, RJ or DJ. Integrated ATE instruments that can inject all these kinds of jitter do not exist currently. It is expected that these issues can be addressed in the test community.

## **1.2 Contributions**

The thesis addresses the urgent need in the semiconductor industry for cost efficient solutions to qualify HSSI jitter and BER performance [1]. We develop accelerated jitter testing solutions based on existing ATE instrument. We also develop novel low cost, non-ATE solutions that overcome the ATE instrument limitation. The contributions include:

- 1) Develop a jitter tolerance extrapolation algorithm that can accelerate jitter tolerance testing by >1000 times [2]. Based on the algorithm, the thesis proposes a solution for jitter tolerance production testing and a solution for characterization. Using existing ATE instruments, the production testing only takes a few tens milliseconds and the characterization only takes around 1 second, the fastest

solution to the best of our knowledge. Direct measurements down to  $10^{-12}$  BER in 3Gpbs applications demonstrate the excellent extrapolation accuracy: the discrepancy between the measured results and extrapolation results is within 2 ps [3].

- 2) Present solutions for transmitter jitter testing using the time domain, frequency domain and hybrid approaches based on existing ATE instruments [4]. We manage to achieve sub-picosecond RJ measurement accuracy: the discrepancy between the ATE and bench measurement results is within 0.5ps and the run-to-run variation on ATE is also within 0.5ps. The DJ discrepancy is only a few picoseconds. The transmitter jitter testing along with other transmitter testing can be done in less than 100 milliseconds while existing solutions usually take a few seconds. In addition, our innovative hybrid approach eliminates some limitations posed by the time domain and the frequency domain approaches, making test results more reliable.
- 3) Propose low cost HSSI testing solutions without the need for high-speed ATE instruments: a) Develop a novel jitter injection technique using the state-of-the-art phase delay lines that can handle data rates up to 12.5Gpbs [5]. b) Investigate the applications of high-speed relays and propose a versatile loopback-based jitter compliance testing solution [5]. c) Modify the FPGA-based BER Tester (BERT) proposed in the M. Eng thesis titled “A Versatile FPGA-based High Speed Bit Error Rate Testing Scheme” to fit into the HSSI bit error detection [5].
- 4) Besides exploring the jitter impact to BER, the thesis also addresses the amplitude noise impact on BER. We further investigate the digital Gaussian noise generation and BER testing scheme proposed in my M. Eng thesis by further exploring the superiority of our approach, adding more accuracy evaluation approaches, improving the BER vs. SNR testing results and reviewing the most recent Gaussian noise generation techniques [6].

## 1.3 Overview of the Thesis

In the remainder of the thesis, Chapter 2 presents the background of the research. We first discuss the HSSI technologies and the BER mechanism. BER is a measure of the HSSI overall performance. We then introduce how the timing jitter and the amplitude noise can affect the BER performance.

In Capture 3, the details of an ATE-based receiver testing solution are presented. We use a high-speed Arbitrary Waveform Generator (AWG) to generate test signals with controllable amounts of injected jitter. Based on the calibrated test signals and the test setup, we develop a jitter tolerance extrapolation algorithm. This algorithm enables us to accelerate the jitter tolerance characterization and production testing by more than 1000 times. Experimental results demonstrate the excellent accuracy of the approach.

In Chapter 4, we present the details of an ATE-based transmitter testing solution. A high bandwidth digitizer is used to capture the transmitter output. We will introduce how the test settings are developed for data acquisition and how the jitter components are extracted. The proposed solution can complete the transmitter testing and characterization in 100 milliseconds, and the test accuracy reaches sub-picosecond.

Capture 5 discusses the HSSI testing techniques that do not rely on high-speed ATE instruments. We propose a phase-delay line based jitter injection scheme. Based on the novel scheme, an external loopback testing solution is developed to reduce the test cost and also overcome some ATE limitations. By putting the ATE-based approach and the loopback approach together using high-speed relays, we propose a more versatile scheme for HSSI validation, debugging, characterization and production testing. In this chapter, we also further address the BER testing under noise and further investigate the Gaussian noise generation techniques.

Conclusions and future investigation directions are provided in Chapter 6.

---

# Chapter 2 - Background

---

## 2.1. High-Speed Serial Communication

The high-speed serial communication interface has been widely used in modern communication to deliver fast and robust data transmission. It delivers data at rates from a few Gigabits per seconds to more than 10 Gbps. Typically, single-ended I/O standards, such as in PCI and VME, are noise limited and load limited to about 200 Mbps. They reach noise limitations at frequencies of about 250 MHz due to the signal integrity deterioration. Differential I/O standards break the frequency barrier of single-ended I/O standards with common mode rejection. They allow data transmission at higher speed, though the clock skew issue arises for differential I/O standards when the frequency approaches 1 Gbps.

The technology that enables multiple Gbps high-speed serial communication is Clock Data Recovery (CDR). Removing clock skew concerns by encoding the clock into every data stream, CDR circuitry provides a mechanism for the clock to track the data. Hence, it eliminates frequency barriers faced by clock synchronous systems. Figure 2-1 shows the CDR mechanism: a transmitter embedding the clock in the data stream and a receiver recovering the clock from the data.

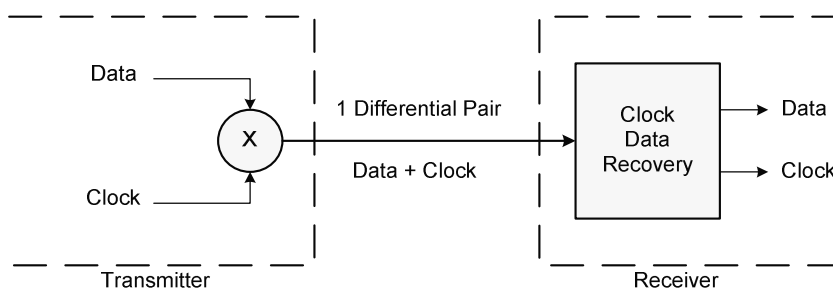


**Figure 2-1:** CDR transmission mechanism

The CDR circuitry is the key structure of an HSSI. At present, the HSSI, which employs the CDR technology and differential signaling, can support applications with data rates above 10 Gbps. The roadmaps of many companies point to higher data rates on each pair of wires. In addition, a wider pipe or datapath can be built by gluing multiple transceivers. Figure 2-2 shows such an example, where 64 bits of data at 250 MHz are transmitted through 8 transceivers. Each transceiver works at 2.5Gbps (8B10 encode/decode is used to guarantee data transitions for clock recovery). The aggregated data rate is 16 Gbps.

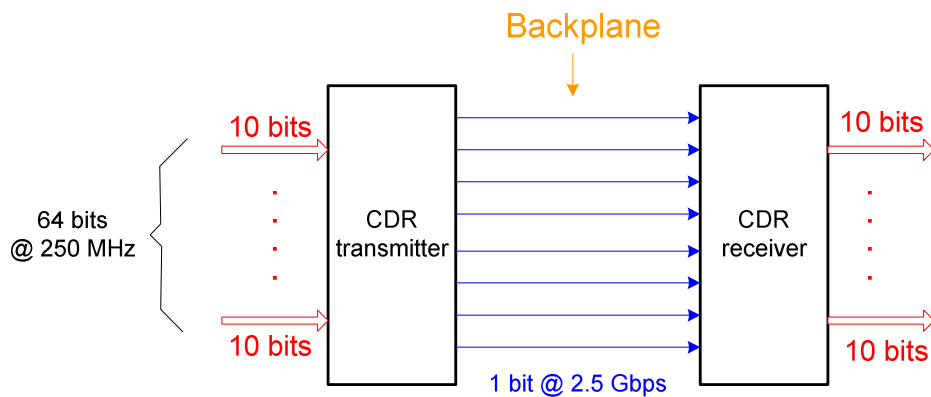


**Figure 2-2:** Applications of multiple HSSIs

Besides the high-speed capability, the serial communication also simplifies routing. In parallel communication, data are usually transmitted one bit at a time down one wire. In multi-gigabit HSSIs, differential I/Os are used and two wires are needed for each connection, but the wires are still much reduced from the parallel approach. Furthermore, in serial communication, the clock signal is embedded in the data and no clock skew exists. All these factors greatly simplify the routing of serial communication. Routing for parallel communication is always challenging. For example, in an 8-bit parallel communication system, 8 wires or 16 wires (differential IOs) are needed for data signals and another one or two wires are needed for the clock signal. Routing 9 or 18 wires across a board and keeping them all synchronized are very difficult and costly, especially for long distance connections. Because much less wires are used in a serial communication system compared to a traditional parallel one, it is possible to put more circuitry on one

die or in one package. Serial communication greatly relieves the package pin count “bottleneck” problem for SoCs.

Finally, a significant advantage of serial communication is the lower energy consumption. Low energy consumption is mainly achieved by using low voltage differential signaling technologies, such as LVDS. The LVDS technology uses a constant-current line driver rather than a voltage-mode driver, so the supply current remains constant as the operating frequency increases, whereas the supply current for CMOS technology increases as the frequency increases. As shown in Figure 2-3, the constant current is typically 3.5 mA [21]. The current passes to a resistor of about 100 Ohms (matched to the cable impedance) at the receiver end, generating a signal with amplitude around 350mV. The low power consumption of serial communication interfaces eliminates the need for either heat sinks or special packaging. Hence, serial communication reduces the system cost.

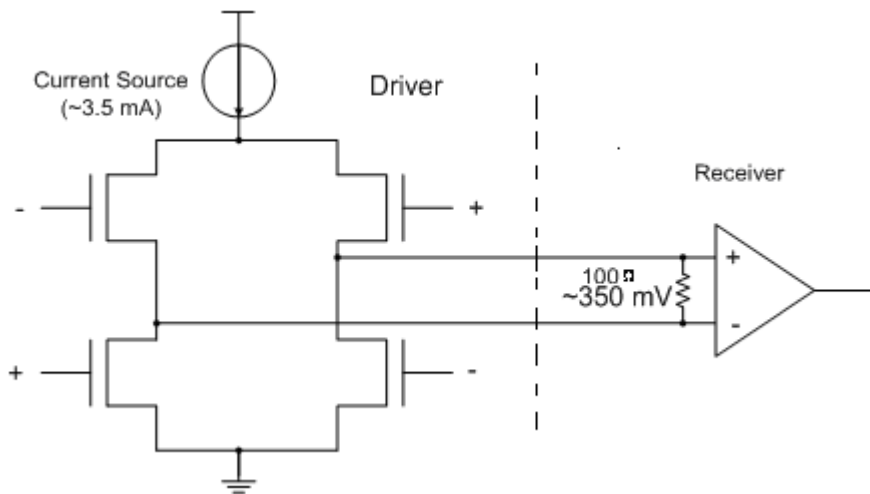


**Figure 2-3:** Current-mode LVDS driver

Due to these advantages, multi-gigabit HSSIs are more and more widely used in high speed communications between devices, boards and systems. To address different applications, several HSSI standards have been developed, such as SATA [22], Fiber Channel (FC) [23] and 10 Gigabit Attachment Unit Interface (XAUI) [24]. Each standard specifies the detailed requirements of its functionalities and signal/device parameters, such as the data rate, amplitude level, slew rate and jitter. As an example, Table 2-1 lists

the physical layer general specifications for SATA. Each device or system designed for the standard has to comply with these specifications.

**Table 2-1:** SATA Physical Layer General Specifications [22]

Parameter	Units	Limit	Gen1	Gen2	Gen3
Channel Speed	Gbps	Nom	1.5	3.0	6.0
FER, Frame Error Rate		Max	8.2e-8 at 95% confidence level	8.2e-8 at 95% confidence level	8.2e-8 at 95% confidence level
$T_{UI}$ , Unit Interval	ps	Min	666.4333	333.2167	166.6083
		Nom	666.6667	333.3333	166.6667
		Max	670.2333	335.1167	167.5583
$F_{tol}$ , Tx freq. accuracy	ppm	Min	-350	-350	-350
		Max	350	350	350

SATA is one of the most popular HSSI standards. It is the primary storage interconnect for PCs to connect the host system to peripherals, such as hard drives, solid state drives, optical drives and removable magnetic media devices [25]. SATA is an evolutionary replacement for the Parallel ATA interface. It can drastically increase the communication bandwidth and reduce the design cost compared to Parallel-ATA. Even compared to other HSSI standards used in storage systems, SATA costs significantly less than SCSI or FC hard drivers. SATA market share has increased tremendously during the past few years: from 43% in 2006 to 97.7% in 2008 in the mobile PC market, and from 58.1% in 2006 to 99% in 2008 in the desktop PC market [26]. More than 1.1 billion SATA hard drivers have been shipped from 2001 to 2008 [27]. Therefore, it is especially beneficial in developing cost-efficient test methodologies for SATA. The experiments in this thesis concentrate on SATA devices, but the methodologies are applicable to other HSSI standards.



### 2.1.1 HSSI Structure

An HSSI consists of two parts: a transmitter (Tx) and a receiver (Rx), connected by transmission medium, such as cables or PCB traces. Figure 2-4 shows the block diagram of an HSSI. The transmitter and the receiver can function independently for half-duplex operation. They can also be combined for full-duplex operation.

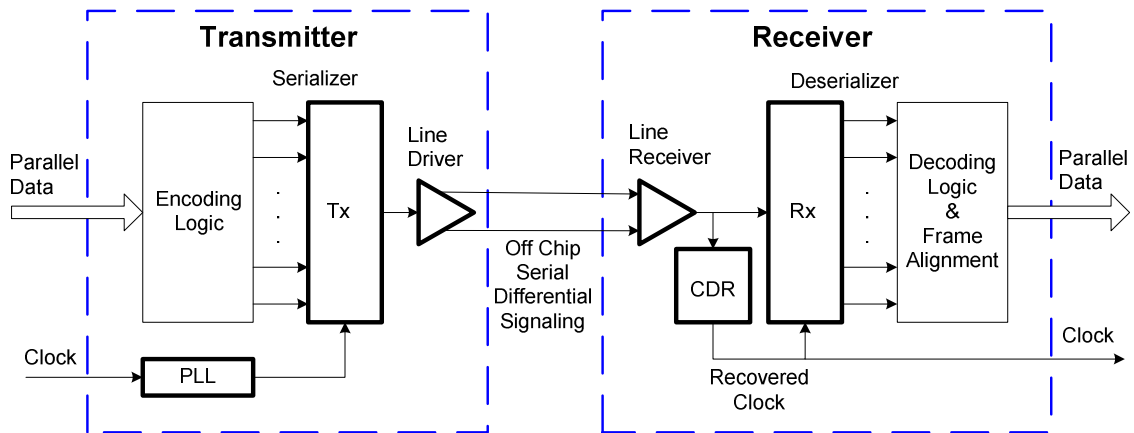


**Figure 2-4:** Block diagram of an HSSI

The transmitter takes parallel data and converts it into a serial format. The PLL in the transmitter generates an internal high-speed clock for the serializer to time the serial data. The differential line driver drives the serialized data into the transmission media. The receiver accepts the high speed serial data from the transmitter. The CDR in the receiver recovers a clock from the received serial data, and re-times the data using the recovered clock. Then the deserializer restores the re-timed serial data to the parallel format.

In the above transmission mechanism, the clock is embedded in the data signal, so only one differential data signal needs to be transmitted. The clock is recovered by the CDR in the receiver side. The CDR circuit extracts the clock information by monitoring the edge transitions of the received data. To ensure that the CDR circuit can function correctly, special encoding logic is needed in the transmitter to make sure that the transmitted data has enough transitions all the time. One solution to guarantee the transitions is to encode

the original parallel data using an 8B10B encoder. An 8B10B encoder converts 8-bit words into 10-bit words, so it can always make sure there are bit transitions, regardless of what pattern is transmitted. For example, in the 8B10B encoding scheme, there are four different symbols for the zero character; all the four symbols have transitions, but get interpreted as zero. In the receiver, the frame alignment block recognizes the word boundary and correctly restores the transmitted parallel sequences. Then the 8B10B decoding logic converts the 10-bit format to the original 8-bit format. The converted sequences are presented on the output ports of the receiver.

In the HSSI structure shown in Figure 2-4, the *Encoding Logic* block and *Decoding logic & Frame Alignment* block can be built with digital circuits; all other blocks can only be built with analog circuits. For HSSIs embedded in FPGAs, the analog blocks are usually hard cores; users can instantiate them and set some parameters, such as PLL frequencies and differential signaling formats. For the digital blocks, the users have the option to use Intellectual Property (IP) cores or develop their own designs. We will demonstrate how these blocks can be instantiated or built in Chapter 5.1.3.

In any communication system, including an HSSI system, we need physical medium to transmit the signal from the transmitter to the receiver. The medium may be PCB traces, cables, or optical fiber in serial communication. One essential feature of the communication medium is that the transmitted signal is corrupted by a variety of possible mechanisms, such as medium loss and additive thermal noise.

### **2.1.2 CDR Characteristics**

As shown in Figure 2-4, the CDR circuitry in the receiver recovers a clock from the received serial data, and then re-times the data using the recovered clock. CDR is the most critical block of the receiver. Figure 2-5 shows a more detailed block diagram of the CDR. The Edge Detector generates all the data edge transitions (both low to high and high to low transitions). Therefore, the output of the edge detector has the frequency component of the data rate. The edge detector output is then fed into a PLL to recover a

clock that is locked to the input serial data rate. The serial data are then re-timed by the recovered clock.

The CDR characteristics are mainly determined by the PLL inside the CDR. The structure of a linear PLL is included in Figure 2-5. The input signal to the PLL comes from the Edge Detector. The Phase Frequency Detector (PFD) compares the frequency and phase difference between the edge detector output and the recovered clock signal, and produces narrow pulses with widths proportional to the phase error. The narrow pulses are sent to the Loop Filter (LF) to generate a voltage, and the voltage adjusts the frequency and phase of the VCO output. The narrow pulses are sent to the Loop Filter (LF) to generate a voltage, and the voltage adjusts the frequency and phase of the VCO output.

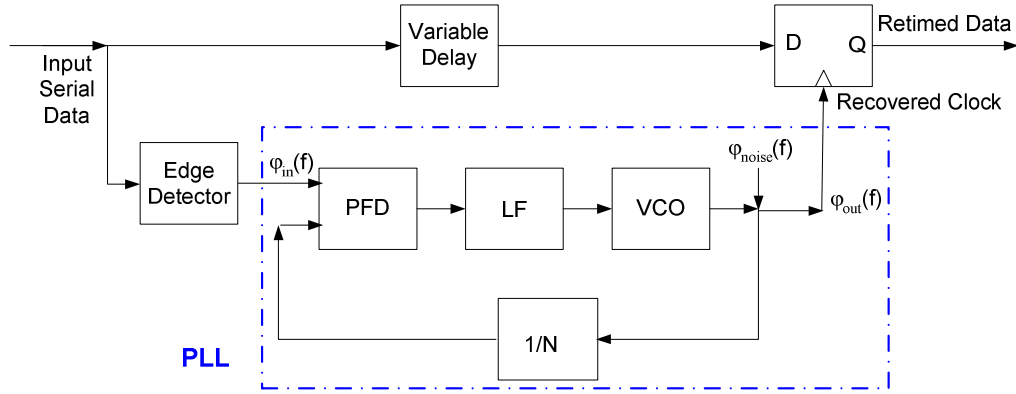


**Figure 2-5:** Block diagram of the CDR with a typical linear PLL

To illustrate the characteristics of the PLL, we use  $\phi_{in}(f)$  to denote the PLL input phase of the signal and  $\phi_{out}(f)$  to denote the PLL output phase in Figure 2-5. In the PLL model,  $\phi_{noise}(f)$  represents the random VCO phase noise, such as the thermal noise and the simultaneous switching noise [68]. Figure 2-6 shows the frequency behavior of the PLL [69]. The function  $\phi_{out}(f)/\phi_{in}(f)$  is the input jitter transfer function, showing a low-pass characteristic. Therefore, the PLL tracks the jitter in the input signal with jitter frequencies below the PLL bandwidth  $f_{PLL}$  (in band jitter). The function  $\phi_{out}(f)/\phi_{noise}(f)$  is the VCO jitter transfer function, showing a high-pass characteristic. The PLL will pass through the spectral content of the phase noise that is above the PLL bandwidth (out of band jitter).

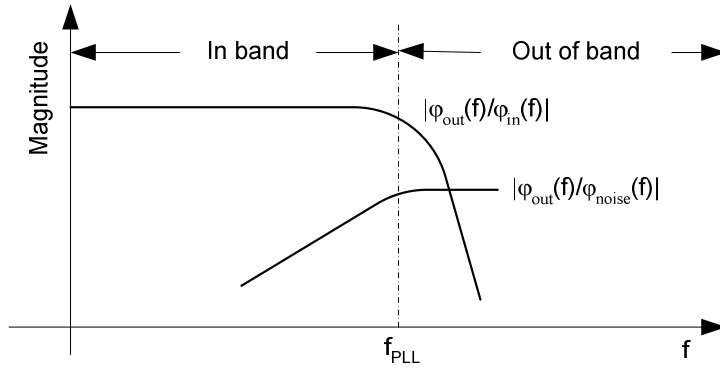


**Figure 2-6:** Phase transfer characteristics of the PLL

From the application point of view, the jitter that the receiver sees is relative to its recovered clock. Therefore, the output jitter is the timing difference between the recovered clock and the data. Because the PLL has a low pass transfer function, the jitter seen by the receiver will have a high-pass transfer characteristic as shown in Figure 2-7. A “golden” PLL for Fiber Channel has a low-pass loop filter with a -3dB frequency at  $F_d/1666$  [70], where  $F_d$  is the data rate. The jitter transfer function implies that a receiver can tolerate more low frequency jitter than high frequency jitter. The jitter tolerance function is the mirror function of the jitter transfer function [71]. Therefore, transmitter jitter and receiver jitter tolerance specifications are defined by jitter frequency bands.

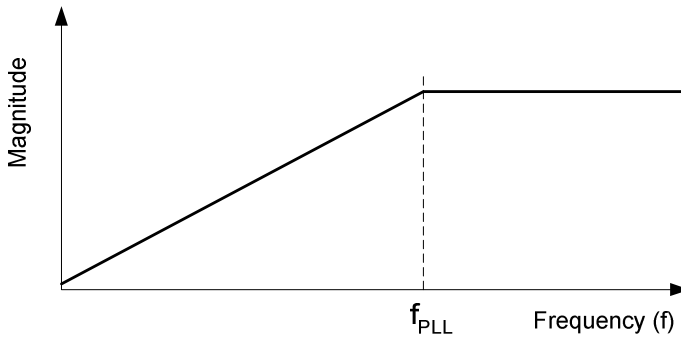


**Figure 2-7:** Jitter transfer function of the receiver

The above discussion concentrates on the linear PLL. In Recent years, the Bang-bang Phase Detector (BBPD) PLL is gaining popularity in HSSI designs. The BBPD PLL samples the incoming data with both the rising edge and falling edge of the VCO clock.

Based on three consecutive samples, the phase detector can determine whether the VCO runs faster or slower. Figure 2-8 illustrates the sampling mechanism: after the PLL is locked, the rising edge of the VCO samples the centre of the data bit and produces a retimed data bit (A), and the next VCO rising edge produces a retimed data bit (B). The VCO falling edge between the two rising edges samples the transition (T) between the data bits A and B. Table 2-2 shows the early/late/hold judgments from the three consecutive samples [73]. The VCO frequency is adjusted according to the early/late judgment.

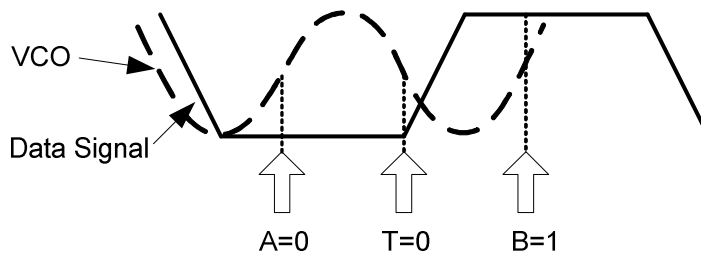


**Figure 2-8:** BBPD PLL sampling

**Table 2-2:** VCO Judgments in BBPD PLL

State	A	T	B	Judgment
0	0	0	0	Hold
1	0	0	1	Early
2	0	1	0	Hold
3	0	1	1	Late
4	1	0	0	Late
5	1	0	1	Hold
6	1	1	0	Early
7	1	1	1	Hold

Compared to the linear PLL, the BBPD PLL has a few unique advantages. First, it does not need to generate narrow pulses and hence can operate at the highest speed at which a process can make a working flip-flop [73]. In addition, the VCO is undisturbed in the absence of data transitions; therefore it suppresses pattern dependent jitter. However, the

nonlinear nature of BBPDs makes the analysis and design of a BBPD PLL difficult. Figure 2-9 shows the first order model of a BBPD PLL presented in [73].

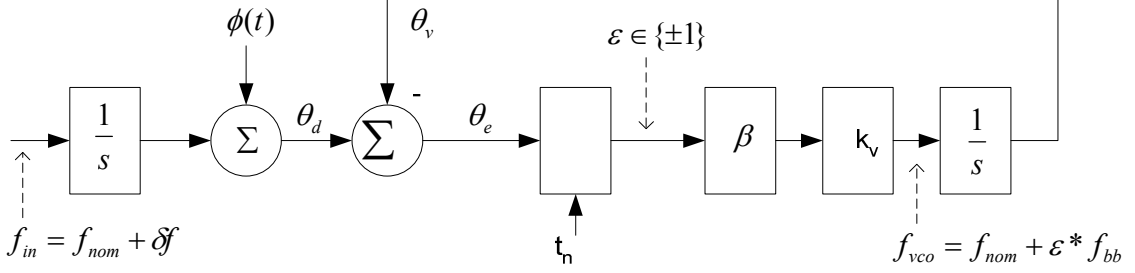


**Figure 2-9:** First order model of a BBPD PLL

In this model,  $\theta_e(t_n)$  is defined as the difference between the data phase  $\theta_d(t_n)$  and the VCO phase  $\theta_v(t_n)$  at the  $n$ th sampling time  $t_n$ . The data phase  $\theta_d(t_n)$  can be represented by

$$\theta_d(t_n) = \theta_d(0) + 2\pi\delta f t_n + \phi(t_n)$$

where  $\delta f$  is the frequency difference between the incoming data signal and the VCO centre frequency, and  $\Phi(t)$  is the phase jitter with a zero mean.

The phase detector quantizes the loop phase error to a ternary value at each sampling time. The error can be denoted by

$$\varepsilon_n = \text{sign}[\theta_e(t_n)]$$

The error signal  $\varepsilon_n$  is -1 when the phase is early, 1 when the phase is late or 0 when it is not possible to determine the phase error due to no data transitions. The error signal drives the VCO to produce a change in the frequency of

$$f_{bb} = \beta * k_v$$

where  $\beta$  is an attenuator.

Therefore, from time  $t_n$  to  $t_{n+1}$ , the VCO runs at one of the two frequencies determined by  $f_{nom} + \varepsilon_n f_{bb}$  ("hold state discussed later), where  $f_{nom}$  is the ideal clock frequency. In a typical CDR,  $f_{bb}$  is on the order of 0.1% of  $f_{nom}$ . The VCO frequency changes in each cycle. We can approximate the update period by

$$t_{update} = 1 / f_{nom}$$

and the up-or-down phase change (also called bang-bang phase step) by

$$\theta_{bb} = 2\pi(f_{bb} / f_{nom})$$

The loop will remain phase locked as long as the input data signal frequency is in the range of VCO frequency. Assuming the phase jitter  $\Phi(t)$  is small, the input signal frequency error  $\delta f$  needs to be smaller than the  $f_{bb}$  frequency, which gives the lock range:

$$-f_{bb} < \delta f < f_{bb}$$

Based on the  $f_{bb}$  frequency, we can also calculate the maximum allowed phase jitter. For phase jitter  $\phi(t) = A \sin(2\pi f_{mod} t)$ , where  $f_{mod}$  is the phase modulation frequency, the instant jitter-induced frequency error is the derivative of the data phase derivation:

$$f_{jitter} = \frac{d[\phi(t)]}{dt} = 2\pi f_{mod} A \cos(2\pi f_{mod} t)$$

Assuming  $\delta f = 0$ , in order to keep the loop locked, the phase modulation amplitude  $A$  at frequency  $f_{mod}$  should satisfy

$$A < \frac{|f_{bb}|}{2\pi f_{mod}}$$

Otherwise, the loop goes into a jitter-induced slew rate limiting. Even though the average input frequency is in the loop lock range, the added jitter causes the instantaneous input frequency deviation to exceed  $\pm f_{bb}$ , resulting in a transient phase error.

For the first order bang-bang loop, all parameters, such as jitter generation, lock range and jitter tolerance, are controlled by one parameter,  $f_{bb}$ , which gives us little design freedom. This limitation can be solved by adding another loop to dynamically adjust the VCO center frequency  $f_{nom}$  to be equal to the incoming data rate. The second loop can be implemented by an integrator.

We can consider the PLL being composed of two non-interacting branches – an integral branch and a bang-bang branch (or proportional branch). To keep the quality of the first order loop, it is needed to keep the phase change due to the proportional branch

dominating over the phase change from the integral branch. The stability factor  $\xi$  of the PLL is defined as the ratio of two phase changes [73]:

$$\xi = \frac{\Delta\theta_{proportional}}{\Delta\theta_{integral}} = \frac{2\beta\tau}{t_{update}}$$

The dual branch BBPD structure provides two degrees of freedom: the loop frequency step  $f_{bb}$  and the stability factor  $\xi$ . In this way, it is possible to make the lock range independent of jitter tolerance and jitter generation. However, more loops also make the PLL design more complicated. There are many factors to consider when implementing a CDR and sometimes we have to make tradeoffs [74]. There is a great pressure to characterize and test well the CDR whether it is implemented with a linear PLL or a BBPD PLL.

### 2.1.3 BER Mechanisms

In the serial communication system, the transmitter, the receiver or the transmission media can introduce distortion or cause bit errors. The correctness and performance of communication interfaces depend on many design choices, such as the CDR mechanism, the PLL bandwidth, the method of encoding/decoding and the transmitter power. As a measure of how well the overall communication system performs, BER is the probability of a bit error at the output of the receiver, compared to the input of the transmitter [28].

By definition, BER is derived by calculating the ratio of the number of erroneous bits to the number of transmitted bits. The concept is very simple, but there are a few issues we need to consider when performing the BER measurement, such as how many bits need to be transmitted and how many bit errors need to be captured in order to get a reliable BER test result. If we transmit  $10^{12}$  bits and get one erroneous bit, can we claim that the BER performance of the system is  $10^{-12}$ ? If we transmit another  $10^{12}$  bits, will we also get one and just one erroneous bit? I would say most likely no. The BER confidence level is used to solve these problems and define how reliable the test result is.



For a given digital communication system or component, there usually is a minimum specification for the BER -  $p(e)$ . In practice,  $p(e)$  is often estimated by calculating the ratio of detected bit errors ( $l$ ) to total bits transmitted ( $n$ ) in a fixed length test sequence. If we denote the ratio by  $p'(e)$ ,  $p'(e)$  is only an estimation of  $p(e)$ . The estimation accuracy improves with the increase of the number of transmitted bits. As shown in the following equation,  $p'(e)$  only equals to  $p(e)$  if an infinite number of bits are transmitted.

$$p'(e) = \frac{l}{n} \xrightarrow{n \rightarrow \infty} p(e)$$

However, it is impossible to transmit an infinite number of bits to get  $p(e)$  in real BER testing because the test time would be infinite. The actual number of transmitted bits depends on the desired BER confidence level. The BER confidence level is defined as the probability that the actual  $p(e)$  is better than a specified BER level  $\gamma$  (such as  $10^{-12}$ ). The Confidence Level ( $CL$ ) is mathematically expressed as

$$CL = p[p(e) < \gamma | l, n]$$

where  $p[]$  indicates probability,  $\gamma$  is a specified BER level, and  $|l, n$  denotes a system where  $n$  bits are transmitted and  $l$  bits of errors are detected.

The confidence level is based on a set of BER measurements. One interpretation of the confidence level is that, if the BER test is repeated many times and the value  $p'(e) = l/n$  is recomputed each time, we expect  $p'(e)$  to be better than the BER level  $\gamma$  for  $CL$  (in percent) of the measurements. To measure BER with a constant confidence level, we need to use a variable-length test sequence [29], [30]. The BER confidence level can be calculated based on the binomial distribution function [31], [32]. The binomial distribution function models events that have only two possible outcomes and is generally written as

$$p_n(k) = \binom{n}{k} p^k q^{n-k}, \text{ where } \binom{n}{k} = \frac{n!}{k!(n-k)!}$$

where  $p_n(k)$  is the probability that  $k$  events (i.e., bit errors) occurs in  $n$  trials (i.e., bits transmitted),  $p$  represents the probability that an event occurs in a single trial (i.e. a bit

error), and  $q$  represents the probability that the event does not occur in a single trial (i.e., no bit error). According to these denotations, we have  $p + q = 1$ .

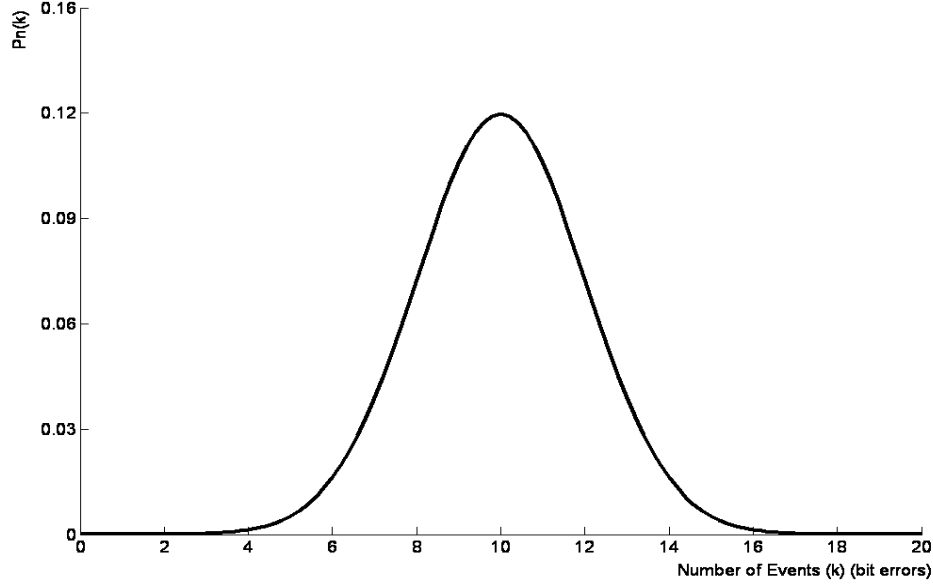


**Figure 2-10:** Graph of the binomial distribution ( $n = 10^8$ ,  $p = 10^{-7}$ )

Figure 2-10 plots the graph of the binomial distribution with  $n = 10^8$  and  $p = 10^{-7}$ . If we treat the  $n$  as the total number of bits transmitted,  $p$  as the BER, and  $p_n(k)$  as the probability that  $k$  bit errors will occur, we can use the distribution to calculate the BER confidence level. We are interested in the probability that  $N$  or fewer bit errors occur in  $n$  transmitted bits. The probability is the Cumulative Distribution Function (CDF) of the binomial distribution and is expressed as

$$p(e \leq N) = \sum_{k=0}^N p_n(k) = \sum_{k=0}^N \frac{n!}{k!(n-k)!} p^k q^{n-k}$$

Then the confidence level can be written as:

$$CL = 1 - \sum_{k=0}^N \left[ \frac{n!}{k!(n-k)!} \right] p^k (1-p)^{n-k}$$

To qualify a BER  $p$ , we need to determine how many bits  $n$  must be transmitted with  $N$  or few errors. We can first choose a hypothetical value of  $p$  and a desired  $CL$ , then solve the above  $CL$  equation to determine  $n$  and  $N$  to prove the hypothesis. It is difficult to directly

solve  $n$  and  $N$ . One solution is to use Poisson theorem [31] to simplify solving  $n$  and  $N$ . Poisson theorem provides a conservative estimate of the binomial distribution function and is written as

$$p_n(k) = \left( \frac{n!}{k!(n-k)!} \right) p^k q^{n-k} \xrightarrow{n \rightarrow \infty} \frac{(np)^k}{k!} e^{-np}$$

An example of the solutions for  $N$  and  $n$  is listed in Table 2-3 [33]. In this system,  $p$  is specified to  $10^{-10}$  and the confidence level  $CL$  is set to 99%. For various bit errors of  $N$ , the corresponding required transmitted bits of  $n$  are solved. According to the table, we have a 99% confidence level to claim  $p(e) < 10^{-10}$  in a 2.5Gbps system if no erroneous bit is detected in 18.5s of testing, one erroneous bit occurs in 26.7s, or two erroneous bits occur in 33.7s.

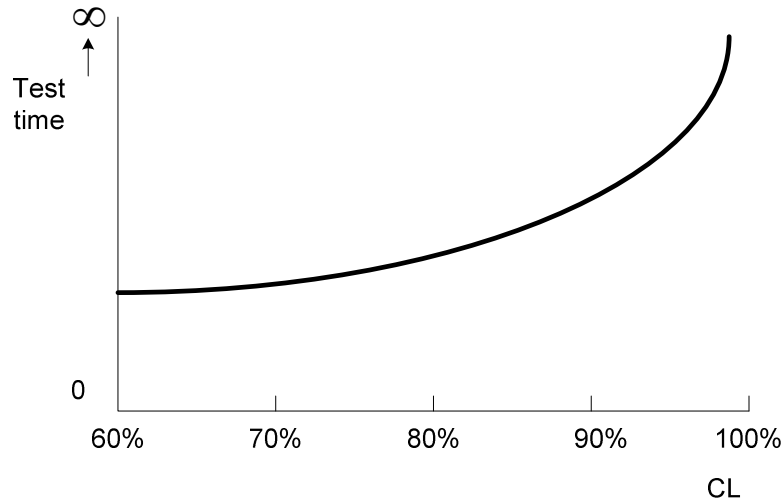
**Table 2-3:** An Example of BER Estimation ( $CL=99\%$  and  $p=10^{-10}$ )

Bit Errors $N$	0	1	2	3	4
Required bits $n$	$4.61 \times 10^{10}$	$6.64 \times 10^{10}$	$8.40 \times 10^{10}$	$1.00 \times 10^{11}$	$1.16 \times 10^{11}$
Test time @ 2.5Gbps (s)	18.5	26.7	33.7	40.2	46.6

The test time  $t$  can be calculated using Gaussian error distribution:

$$t = \frac{\ln(1 - CL)}{p * r}$$

where  $CL$  is degree of confidence level,  $p$  is the upper bound of BER and  $r$  is the data rate. Figure 2-11 shows the relationship between the test time and the confidence level. If we want to achieve higher confidence level, the test time must increase. We can not achieve 100% confidence level in BER testing because it requires infinite test time. The BER measured by BERT equipment is only an estimate of the true BER. In practice, we are hence forced to make tradeoffs between the confidence level and the test time.



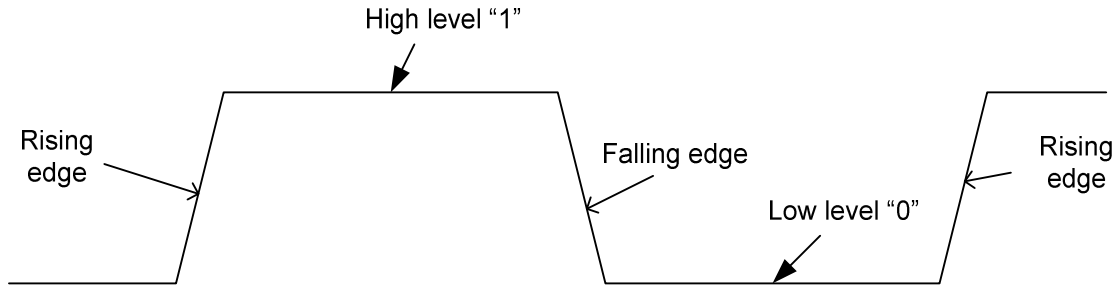
**Figure 2-11:** Test time vs. BER confidence level

Table 2-3 also shows that we need to give some margin for a measured BER if we use only a few bit errors to qualify BER performance. For example, if we measure 3 bit errors out of  $10^{11}$  transmitted bits, we should not think that the BER performance is  $3.33 \times 10^{-11}$ . It is only reasonable to say that we have 99% confidence level that the BER performance is better than  $10^{-10}$ . We normally need at least  $10 \times (1/p)$  transmitted bits in order to qualify  $p$  BER performance. As shown in Table 2-3, to qualify  $10^{-10}$  BER performance, we can tolerate up to 3 bit errors if we transmit  $10^{11}$  bits. This provides us guidelines on how to efficiently and confidently test the BER for jitter tolerance qualifications discussed in Chapter 3.

### 2.1.4 Jitter and Noise Impacts to BER

In serial communication systems, there are various signal formats in time domain. The most commonly used format is Non Return Zero (NRZ). Non Return Zero Inverted (NRZI) and Return Zero (RZ) are also used in some systems. In NRZ format, the binary information digit 1 is encoded as a high signal represented by “1”, and the binary information digit 0 is encoded as a low signal represented by “0”. The ideal NRZ signal can be represented by a trapezoidal waveform as shown in Figure 2-12. The waveform

consists of four components: high level “1”, low level “0”, rising edge (0 to 1 transition) and falling edge (1 to 0 transition).



**Figure 2-12:** Ideal digital signal

When the ideal signal is transmitted, it gets contaminated by a physical process called noise. The deviation of a noise-contaminated signal from its ideal position can be viewed from two aspects: time-deviation (jitter) and amplitude-deviation (amplitude noise). Figure 2-13 illustrates the two deviations:  $\Delta t$  and  $\Delta v$ .

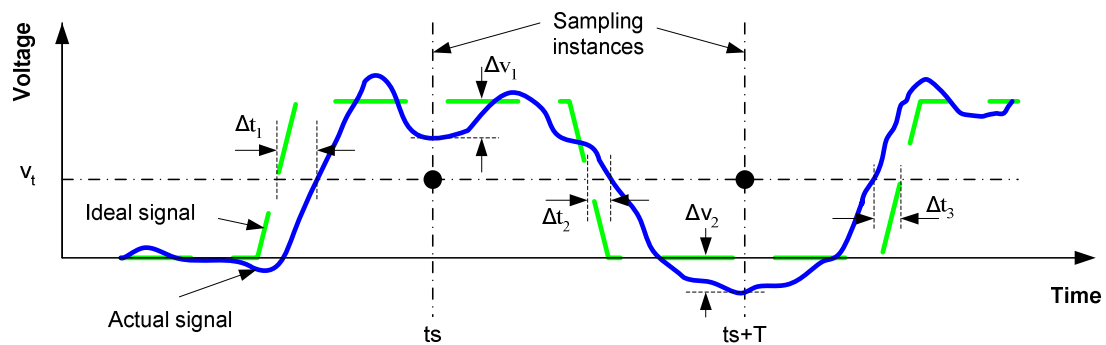


**Figure 2-13:** Timing and amplitude deviations in an actual data signal.

At the receiver side, the CDR samples the actual data signal at sampling instance  $t_s$  and compares the sampled value with a threshold voltage  $V_t$ . If the value is bigger than  $V_t$ , logic “1” is received; otherwise, logic “0” is received. An ideal receiver samples data in the middle of each data bit. Without amplitude noise, the receiver can always correctly recover the transmitted bit. Under the presence of jitter and noise, the transition edge of the signal can fluctuate horizontally across the sampling point (along the time axis), and

the signal voltage can fluctuate vertically across the sampling point (along the voltage axis). Both the time deviation and amplitude deviation can cause a bit error – bit “0” is received as bit “1” or bit “1” is received as bit “0”.

If we ignore the setup time and hold time requirements [109], timing jitter can cause bit errors in the following two conditions:

- For logic “1”, the rising edge lags behind the sampling instance or the falling edge is ahead of the sampling instance
- For logic “0”, the falling edge lags behind the sampling instance or the rising edge is ahead of the sampling instance

Amplitude noise causes bit errors in the following two situations:

- For logic “1”, the voltage level at the sampling instance is smaller than the threshold voltage
- For logic “0”, the voltage level at the sampling instance is bigger than the threshold voltage

The timing and amplitude noise impacts on BER can be characterized by two parameters – Jitter and Signal-to-Noise Ratio (SNR). SNR quantitates the amplitude noise while jitter represents the timing deviation.

## **2.2 Timing Jitter**

### **2.2.1 Jitter Overview**

Jitter is the deviation of a signal from its ideal timing. There are different types of jitter. TJ is composed of RJ and DJ [34], [35], [36]. RJ is caused by random events and is usually characterized statistically by a Gaussian distribution, which can be quantified by a mean and a standard deviation. Because a Gaussian distribution is unbounded (its peak-to-peak value approaching infinity), the peak-to-peak value is sample size dependent.

Therefore, the peak-to-peak value of RJ is related to the BER and TJ is defined at a certain BER level.

DJ is caused by deterministic events and has a bounded peak-to-peak value. DJ can be decomposed into Periodic Jitter (PJ), Bounded Uncorrelated Jitter (BUJ) and Data Dependent Jitter (DDJ) [37]. PJ is caused by repetitive noise sources, such as clock signals and oscillators. BUJ is usually caused by coupling, such as from adjacent signal paths and on-chip logic switching. DDJ depends on the bit pattern in the signal under test and can be further classified into Duty Cycle Distortion (DCD) and Inter-Symbol Interference (ISI). DCD is caused by an imbalance in the drive circuit, which generates a signal having unequal pulse widths for high and low logic values. ISI is caused by frequency related losses in the signal path, such as those caused by the bandwidth limitation. Figure 2-14 shows the relationship of all the jitter components.

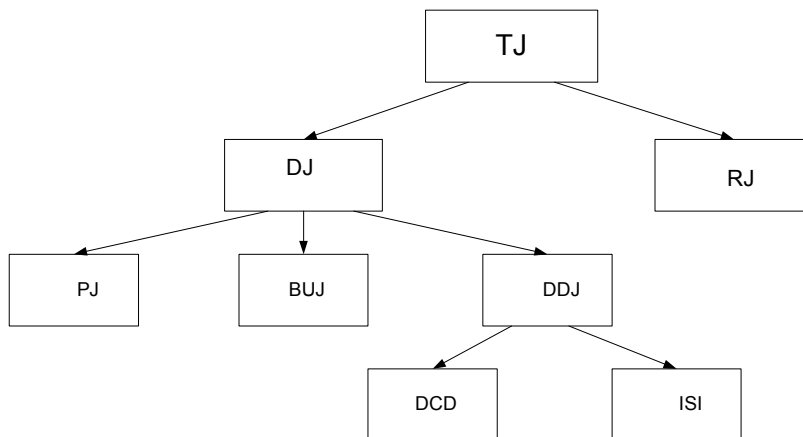


**Figure 2-14:** Jitter components

Most communication standards, such as SATA, Fiber Channel and XAUI, specify jitter in terms of DJ and TJ as separate specifications [22], [23], [24]. Table 2-4 summarizes the HSSI transmitter jitter specifications for the SATA [22] at  $10^{-12}$  BER. The normal data rate is 1.5Gbps for Gen1, 3.0Gbps for Gen2 and 6.0Gbps for Gen3. Table 2-5 summarizes the SATA specifications of the lab-sourced signals for HSSI receiver jitter tolerance testing. As we can see, the maximum jitter the receiver should tolerate is higher than the maximum jitter allowed from the transmitter output. For example, the receiver TJ

tolerance specification for Gen2 is 0.60UI while the transmitter jitter specification is 0.37UI. This is understandable because the transmission medium between the transmitter and the receiver may introduce extra jitter.

**Table 2-4:** Transmitter Jitter Specifications for SATA

Parameters	Units	Limit	Gen1	Gen2	Gen3
TJ, $f_{\text{BAUD}}/500$	UI	Max	0.37	0.37	--
DJ, $f_{\text{BAUD}}/500$	UI	Max	0.19	0.19	--
TJ*	UI	Max	--	--	RJp-p + 0.34
RJ*	UI	Max	--	--	0.18p-p

\* More detailed test conditions are defined in [22]

**Table 2-5:** Receiver Jitter Tolerance Specifications for SATA

Parameters	Units	Limit	Gen1	Gen2	Gen3
TJ, $f_{\text{BAUD}}/500$	UI	Max	0.60	0.60	--
DJ, $f_{\text{BAUD}}/500$	UI	Max	0.42	0.42	--
TJ after CIC, JTF defined	UI	Max	--	--	0.60
RJ before CIC, MFTP JTF defined	UI	Max	--	--	0.18p-p (2.14ps, 1 sigma)

## 2.2.2 Jitter and BER

Jitter can cause bit errors in serial communication when the recovered clock re-times the serial data signal. Figure 2-15 illustrates the relationship between jitter and BER. Ideally, the data are always sampled in the mid-bit (sampling instance  $t_s = \text{UI}/2$  in Figure 2-15(a)). This is usually true if the jitter frequency is within the bandwidth of the CDR because the sampling clock is recovered from the data signal and the clock can track the in-band jitter. However, for out-of-band jitter, the sampling clock cannot track the data any more and the jitter can cause bit errors.



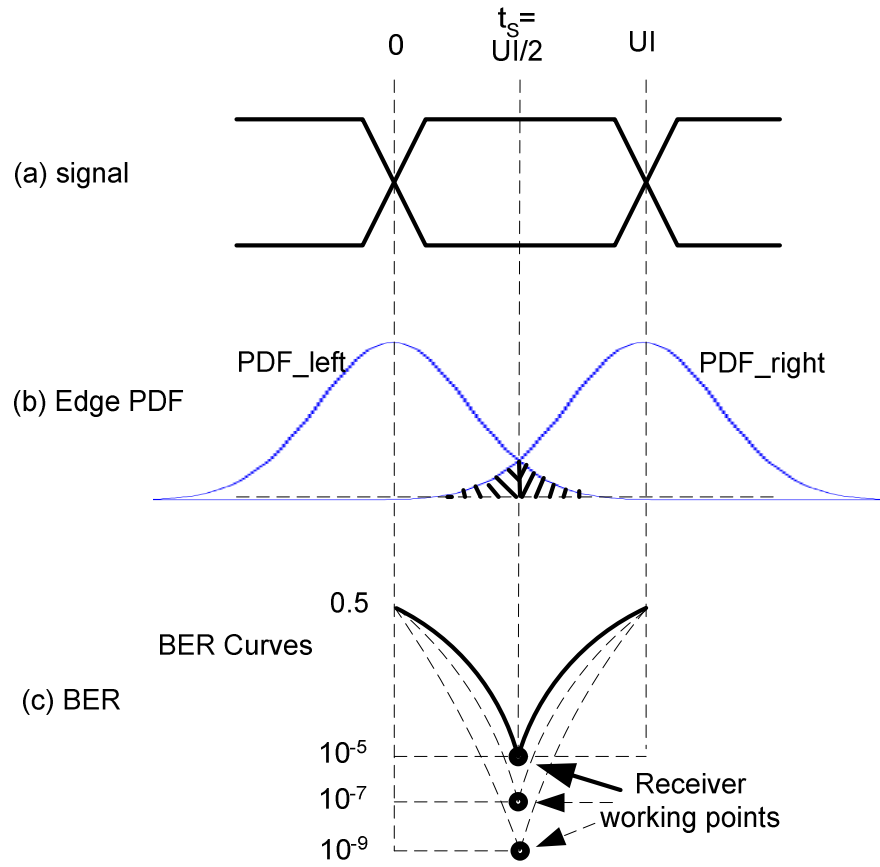


**Figure 2-15:** Jitter and BER in the receiver

Figure 2-15(b) shows an example of the jitter profile. The signal edge transition is disturbed by RJ. The RJ is assumed to be Gaussian. The Probability Density Function (PDF) of a zero-mean Gaussian variable is

$$p(x) = \frac{1}{\delta\sqrt{2\pi}} e^{-x^2/2\delta^2}$$

where  $\delta$  is the standard deviation.

One important function used to characterize the Gaussian distribution is the Q factor, which represents the area under the tail of the Gaussian PDF. The Q factor is widely used for computing the error probability in communication systems [38]. Normalized to zero mean and unit variance,  $Q(x)$  is defined as

$$\begin{aligned}
Q(x) &= \frac{1}{\sqrt{2\pi}} \int_x^{\infty} e^{-t^2/2} dt, \quad x \geq 0 \\
&= \frac{1}{2} \operatorname{erfc}\left(\frac{x}{\sqrt{2}}\right)
\end{aligned} \tag{2-1}$$

where  $\operatorname{erfc}(x)$  denotes the complementary error function, defined as

$$\operatorname{erfc}(x) = \frac{2}{\sqrt{\pi}} \int_x^{\infty} e^{-t^2} dt \tag{2-2}$$

As shown in Figure 2-15(b), the PDF of the left and right edge transitions of the data bit can be expressed by

$$\begin{aligned}
p_{\_left}(x) &= \frac{1}{\delta\sqrt{2\pi}} e^{-x^2/2\delta^2} \\
p_{\_right}(x) &= \frac{1}{\delta\sqrt{2\pi}} e^{-(x-UI)^2/2\delta^2}
\end{aligned}$$

Bit errors may occur when the left edge occurs after the  $t_s$  (illustrated by back slash) or the right edge occurs before the  $t_s$  (illustrated by forward slash). Assuming uniform bit distribution, i.e., a 50% chance of errors in these two cases, the BER can be expressed by

$$\begin{aligned}
BER(t_s) &= 0.5 * \left( \int_{t_s}^{\infty} p_{\_left}(t) dt + \int_{-\infty}^{t_s} p_{\_right}(t) dt \right) \\
&= 0.5 * \left( \int_{t_s}^{\infty} \frac{1}{\delta\sqrt{2\pi}} e^{-\frac{t^2}{2\delta^2}} dt + \int_{-\infty}^{t_s} \frac{1}{\delta\sqrt{2\pi}} e^{-\frac{(t-UI)^2}{2\delta^2}} dt \right) \\
&= \int_{t_s}^{\infty} \frac{1}{\delta\sqrt{2\pi}} e^{-\frac{t^2}{2\delta^2}} dt
\end{aligned} \tag{2-3}$$

According to Equation (2-2), Equation (2-3) can be rewritten as

$$BER(ts) = 0.5 * \operatorname{erfc}\left(\frac{t_s}{\delta\sqrt{2}}\right) \tag{2-4}$$

By substituting  $\delta$  with the Root-Mean-Square (RMS) value of the RJ,  $RJ_{RMS}$ , Equation (2-4) becomes

$$BER(ts) = 0.5 * erfc(\frac{t_s}{RJ_{RMS}\sqrt{2}}) \quad (2-5)$$

Equation (2-5) directly links the jitter to BER. The BER and jitter relationship can further be transferred to BER and Q factor. As shown in Figure 2-15(c), the receiver works at the crossing points of the bathtub curves. Therefore, we have

$$t_s = UI / 2 \quad (2-6)$$

$$UI = DJ + 2Q * RJ_{RMS} \quad (2-7)$$

where Q is  $Q(x)$  defined in Equation (2-1) with  $x = BER$  [34].

By substituting  $t_s$  and  $RJ_{RMS}$  in Equation (2-5) according to s (2-6) and (2-7), we have

$$BER = 0.5 * erfc(\frac{Q}{\sqrt{2}}) \quad (2-8)$$

or

$$Q = \sqrt{2} * erfc^{-1}(2 * BER) \quad (2-9)$$

Equations (2-8) and (2-9) directly link BER and Q factor. If we know one parameter, the other can be calculated accordingly. We would need these two equations for our jitter tolerance extrapolation.

In the above analysis, we ignore the DJ effect. This is reasonable since the bit errors are caused by RJ at low BER regions. Because the DJ is bounded, it only adds offsets to a bathtub curve; it does not change the shape of the lower part of the bathtub curve [34].

### 2.2.3 Jitter Testing and Jitter Injection

As we can see, jitter can cause bit errors. From the receiver point of view, there are two possible factors that can cause excessive bit errors. One is that there is excessive jitter in the received signal, which means the transmitter generates too much jitter (assuming no issues with the transmission media). Another factor is that the minimum jitter that the receiver can tolerate at a certain BER level is lower than what is expected. To quantify the two factors, the transmitter jitter specification defines the maximum jitter the

transmitter is allowed to generate, and the receiver jitter tolerance defines the minimum jitter the receiver should tolerate to achieve a certain BER level. Therefore, in HSSI jitter compliance testing, we qualify the transmitter jitter and the receiver jitter tolerance performance.

Because the jitter is usually defined at  $10^{-12}$  BER or lower, direct measurements are too time consuming to conduct in most cases. Considering the BER performance of an HSSI is related to jitter according to Equation (2-5) or related to Q factor according to Equation (2-8), Q factor can be used to accelerate the BER and jitter measurement. One important assumption for the Q factor approach is that RJ is Gaussian. A Gaussian distribution is theoretically unbounded and can be characterized by its standard deviation. For example, a Gaussian distribution on average will exceed a span of 14 times its standard deviation one time for every  $10^{12}$  samples, which can be interpreted as Q factor is 7 ( $14/2=7$ ) at  $10^{-12}$  BER. If we know the DJ and the RJ, we can estimate the transmitter TJ as follows:

$$TJ = DJ + 2Q * RJ$$

where the Q factor is 7 at  $10^{-12}$  BER.

The above Q factor based transmitter TJ estimation is much faster than direct measurements at lower BERs. We can also use the Q factor to accelerate the receiver jitter tolerance testing that is discussed in Chapter 3. Even though the Q factor is widely used in the industry [34], [140], the measurement accuracy may be affected if the RJ distribution deviates from the true Gaussian distribution [141]. For non-Gaussian distributions, we can not use the Equation (2-3) to calculate the BER as shown in the overlap area in Figure 2-15(b). However, the Q factor based approaches in this thesis are still valid because RJ is primarily due to the thermal noise in electrical components, which has a white power spectrum density and whose PDF is Gaussian. Even though there are some non-Gaussian RJ sources, such as 1/f noise and shot noise [7], our eye mask testing approach discussed in Chapter 4.3.5 provides a mechanism to detect it.

To accelerate the HSSI receiver jitter tolerance qualification, we also need to stress the receiver with controllable amounts of injected jitter. By varying the injected jitter in the

input signal, we can make the receiver work at different higher BER levels, which are much less time-consuming to test. The jitter tolerance performance at low BER levels can then be extrapolated according to the measured jitter vs. BER relationship at high BER levels.

Jitter is traditionally injected using a few instruments in lab. In [34], a FM source is used to inject PJ; a random noise generator is used to inject RJ; a long cable or a long backplane PCB trace is used to inject DDJ. These kinds of setup can be used to inject large amounts of jitter to test receiver jitter tolerance. However, besides the complexity, it is difficult to mix the different jitter components together and characterize the test signals accurately.

Laquai and Cai propose a jitter tolerance test methodology in [40] based on a DDJ injection filter. This approach uses a passive filter that is carefully tweaked to condition the data eye seen by the receiver. This filter can add jitter to stress the receiver. A big advantage of the jitter injection filter is that it only takes a small space on a loadboard and the cost is very low. However, this methodology does not offer the flexibility of varying the amount of injected jitter. In addition, the amount of the injected jitter is very sensitive to the data rate. For example, for the same filter and the same transceiver, the injected jitter changes from 0.25UI at 2.125Gbps to 0.42UI at 2.67Gbps [40]. This limits the applications of the approach because it has become quite common for current HSSIs to accommodate multiple protocols and hence requires the test equipment to have the ability to generate controllable amount of jitter.

Hafed *et al.* propose a high density HSSI tester that can significantly reduce the HSSI validation time by relying on parallelism and efficient measurement techniques [41]. In this tester, the jitter is injected by modulating the PLL input signal of the transmit port module [139]. The advantage of this approach is that the high-speed signal path is completely untouched. Hence the approach would not produce unwanted jitter in the high-speed signal path when the injected jitter is programmed to zero. However, the injected jitter frequency is limited to the tracking bandwidth of the PLL. Chapter 6.2.1

will demonstrate that any jitter with frequencies above the PLL bandwidth will be drastically attenuated.

Keezer *et al.* present another modular approach in [42] for testing multiple Gbps HSSIs. The approach eliminates the PLL bandwidth limitation by modulating the high-speed clock (PLL output signal) that has the same rate as the Gigabit serial data signal. The jitter is injected to the clock signal through dynamically shifting its phase by ATE. Advantest also developed a jitter injection module that can mix any modulated signal as a jitter signal with a carrier signal [43].

Sunter *et al.* propose an alternative approach in [44] for the jitter tolerance testing. Instead of injecting jitter to the test signal, the approach uses on-chip undersampling to measure parameters that affect the jitter tolerance, such as high-frequency jitter in the received signal and the recovered clock. This approach requires that the CDR be selected to lock either to the received serial data or to an offset reference clock, and that the parallel data ports be fully accessible. A module called UnLimited Time Resolution Analysis is used to extract all the measurements. The module can be placed either on the loadboard or on-chip. However, adding an extra module onto a loadboard or a device requires extra space and cost. It also complicates the design and test program development.

There are several other jitter injection schemes, such as these presented by Yamaguchi *et al.* in [81], by Tabatabaei *et al.* in [134] and by Ishida *et al.* in [136]. In this thesis, we present two jitter injection techniques. One is based on an AWG on ATE, which does not need any extra module or add-on circuits. This approach can qualify the jitter tolerance of HSSIs with data rates up to 3Gbps. Another jitter injection technique is based on the state-of-the-art phase delay product, which can be used to test HSSIs with data rates up to 12.5Gbps. The details of each technique will be presented in Chapter 3.2 and Chapter 5.2 respectively.

## 2.3 Amplitude Noise

### 2.3.1 BER and SNR

As discussed in section 2.1.4, amplitude noise can cause bit errors when the noise exceeds a certain level. The BER characterizes the probability of bit errors and the SNR defines the ratio of the signal amplitude over the noise amplitude. The relationship between BER and SNR can be derived from the Additive White Gaussian Noise (AWGN) communication model [38]. The basic components of a communication system include a transmitter, a receiver and a communication channel. One problem associated with the channel is that it corrupts the transmitted signal in a random manner. The AWGN model is predominantly used to analyze this problem. Its mathematical model is shown in Figure 2-16 [38]. In the AWGN model, the transmitted signal  $s(t)$  is corrupted by noise  $n(t)$ . The model can be expressed by

$$r(t) = s(t) + n(t).$$

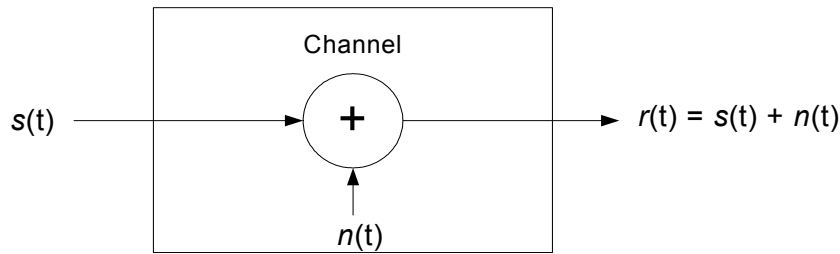


**Figure 2-16:** AWGN channel model

The noise is introduced by the channel, as well as by electronic components, including amplifiers at the receiver. This type of noise is most often characterized as thermal noise, or statistically as Gaussian noise. Its PDF is expressed by

$$p(x) = \frac{1}{\sigma\sqrt{2\pi}} e^{-(x-m_x)^2/2\sigma^2}$$

where  $m_x$  is the mean and  $\sigma^2$  is the variance of the Gaussian random variable.

In general, BER is a function of the characteristics of the channel (i.e., amount of noise), the type of waveforms used to transmit information over the channel, the transmitter power, the timing jitter, and the method of demodulation and decoding. In baseband

transmission, the data and clock are combined on the transmitter side and transmitted as digital waveforms. One commonly used baseband scheme is NRZ CDR encoding, which has been discussed in Chapter 2.1. The receiver in the system samples the received bit stream at an appropriate time point and decides whether the sampled value represents a binary one or zero. Careful timing extraction leads to a reduction in the number of transmission errors. A matched filter is a linear system that significantly alters the shape of both the signal and the noise in a way that increases the SNR. Figure 2-17 shows the structure of a binary matched filter receiver [38], [45]. The following introduces the “one or zero” decision principle and evaluates the BER performance of the binary matched filter receiver.

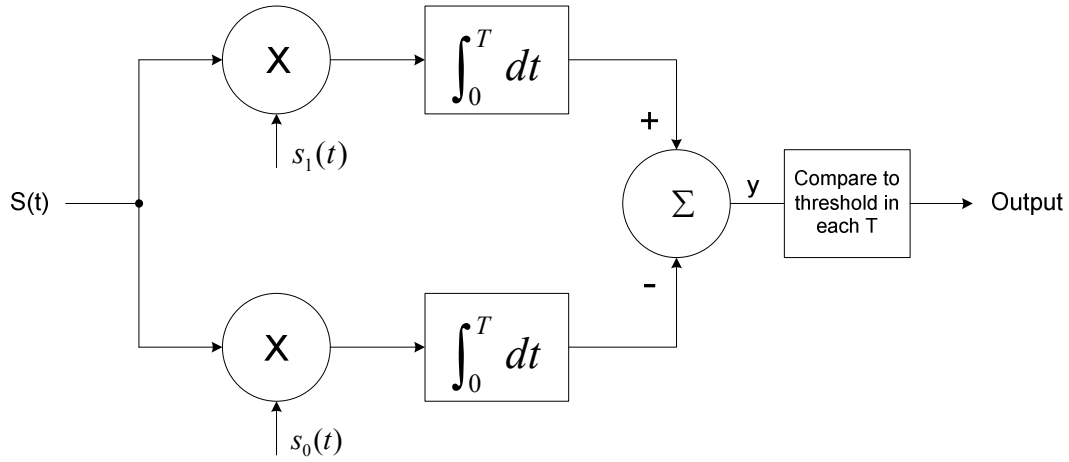


**Figure 2-17:** Binary matched filter receiver

The receiver consists of two filters, one matching to  $s_0(t)$  and the other matching to  $s_1(t)$ . Each filter consists of a multiplier and an integrator. The receiver compares the output of the two filters. The output of each integrator is a number composed of a deterministic part (due to the signal) and a random part (due to the additive noise). The additive noise is assumed to be zero-mean Gaussian and its frequency spectrum is flat. Suppose the input signal to the receiver is  $s_i(t) + n(t)$ , where  $i$  is either zero (binary 0 is transmitted) or unity (binary 1 is transmitted). The comparator input is

$$y = \int_0^{T_s} s_i(t)[s_1(t) - s_0(t)]dt + \int_0^{T_s} n(t)[s_1(t) - s_0(t)]dt$$



The value of  $y$  consists of two integrals. The average of the second integral is zero since the noise is zero mean. Therefore, the mean value of  $y$  is given by

$$m_y = \int_0^{T_b} s_i(t)[s_1(t) - s_0(t)]dt$$

and the variance of  $y$  is given by

$$\begin{aligned}\sigma_y^2 &= E\{[y - m_y]^2\} \\ &= E\left\{\left[\int_0^{T_b} n(t)[s_1(t) - s_0(t)]dt\right]^2\right\} \\ &= E\left\{\int_0^{T_b} \int_0^{T_b} n(t)n(v)[s_1(t) - s_0(t)][s_1(v) - s_0(v)]dtdv\right\}\end{aligned}$$

Because the noise is assumed to be white with power spectral density  $G_n(f) = N_o/2$ , the autocorrelation of the noise is the inverse Fourier transform of the power spectrum, or  $R_n(t) = N_o \delta(t)/2$ . According to this and  $E\{n(t)n(v)\} = R_n(t - v)$ , we have

$$\begin{aligned}\sigma_y^2 &= \left\{\int_0^{T_b} \int_0^{T_b} \frac{N_o}{2} \delta(t - v)[s_1(t) - s_0(t)][s_1(v) - s_0(v)]dtdv\right\} \\ &= \frac{N_o}{2} \int_0^{T_b} [s_1(t) - s_0(t)]^2 dt\end{aligned}$$

According to the mean and variance of  $y$ , we can get the probability density of  $y$ . As shown in Figure 2-18, the probability density fits into one of the two PDFs labeled with  $p_0(y)$  -- 0 being transmitted, and  $p_1(y)$  -- 1 being transmitted. The two functions have the same variances but different mean values,  $m_0$  and  $m_1$  respectively.

The comparator threshold is chosen as the two-PDF cross point labeled as  $y_0$ . If  $y$  is greater than  $y_0$ , we assume that  $s_1(t)$  is being sent; otherwise,  $s_0(t)$  is being sent. Because of the symmetry, the threshold  $y_0$  is the midpoint between the mean values of the two PDFs:

$$y_0 = \frac{m_1 + m_0}{2}$$

$$\begin{aligned}
&= \frac{1}{2} \int_0^{T_b} [s_1(t) + s_0(t)][s_1(t) - s_0(t)] dt \\
&= \frac{1}{2} \int_0^{T_b} [s_1^2(t) - s_0^2(t)] dt
\end{aligned}$$

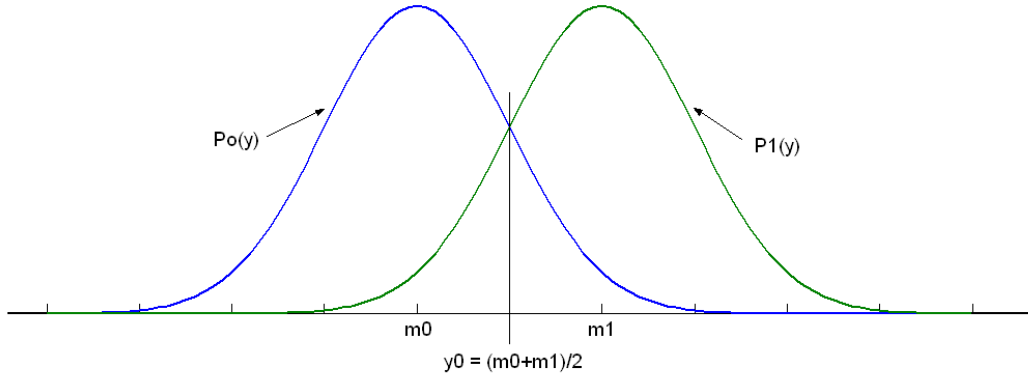


**Figure 2-18:** Probability densities of  $y$

Because the integral of the square of the signal is the signal energy over the bit period, the threshold becomes

$$y_0 = \frac{E_1 - E_0}{2}$$

where  $E_1$  and  $E_0$  are denoted as the energy for the two signals  $s_1(t)$  and  $s_0(t)$ , respectively.

According to the two PDFs shown in Figure 2-18, we can calculate the error probability of the receiver. The probability of mistaking a transmitted 1 for a 0 is the integral of  $p_1(y)$  between  $[-\infty, y_0]$ , and the probability of mistaking a transmitted 0 for a 1 is the integral of  $p_0(y)$  between  $[y_0, \infty]$ . Hence, the error probability is given by the areas under the tails of the PDFs. Assuming that the two signals,  $s_0(t)$  and  $s_1(t)$ , have equal energy, the probability of an error is

$$\begin{aligned}
P_e &= \frac{1}{\sqrt{2\pi}\sigma} \int_0^{\infty} \exp\left[-\frac{(y-m_0)^2}{2\sigma^2}\right] dy \\
&= Q\left(\sqrt{\frac{E(1-\rho)}{N_o}}\right)
\end{aligned} \tag{2-10}$$

where  $Q(\cdot)$  is the Q factor (discussed in Chapter 2.2.2),  $E$  is the average energy of the two signals,  $\rho$  is the correlation coefficient of the two signals, and  $N_0$  is the noise power per Hz.  $E$ ,  $N_0$  and  $\rho$  are defined as

$$E = \frac{E_0 + E_1}{2}$$

$$N_0 = \frac{\sigma^2}{f_m} \quad (f_m \text{ is the bandwidth})$$

$$\rho = \frac{\int_0^{T_b} s_0(t)s_1(t)dt}{E}$$

As can be seen from Equation (2-10), the BER is determined by three factors: the average energy per bit  $E$ , the correlation of the two signals  $\rho$ , and the noise power per Hertz  $N_0$ . To understand the relationship between BER and  $E/N_0$ , we consider three cases where the correlation coefficient  $\rho$  is different.

The first case assumes that  $s_0(t) = s_1(t)$ . Then the correlation coefficient  $\rho$  equals to 1. According to Equation (2-10), the BER is

$$P_e = Q(0) = \frac{1}{2}$$

This result can be easily explained. Since the same signal is used to transmit both 0 and 1, there is actually no information provided and the receiver can only randomly guess the received information.

The second case assumes that  $s_0(t) = -s_1(t)$ . In this case, the correlation coefficient  $\rho$  equals to -1, and the BER is

$$P_e = Q\left(\sqrt{\frac{2E}{N_0}}\right)$$

The third case assumes that  $s_0(t) = 0$  and  $s_1(t) = 1$ . Because only a single power supply is needed, most digital communication systems, including HSSIs, use this format. In this case, the correlation is  $\rho = 0$ , and the BER becomes

$$P_e = Q\left(\sqrt{\frac{E}{N_o}}\right)$$

or

$$BER = Q(\sqrt{SNR}) \quad (2-11)$$

Figure 2-19 plots the relationship between the BER and the SNR for the above three values of correlation: -1, 0 and 1.

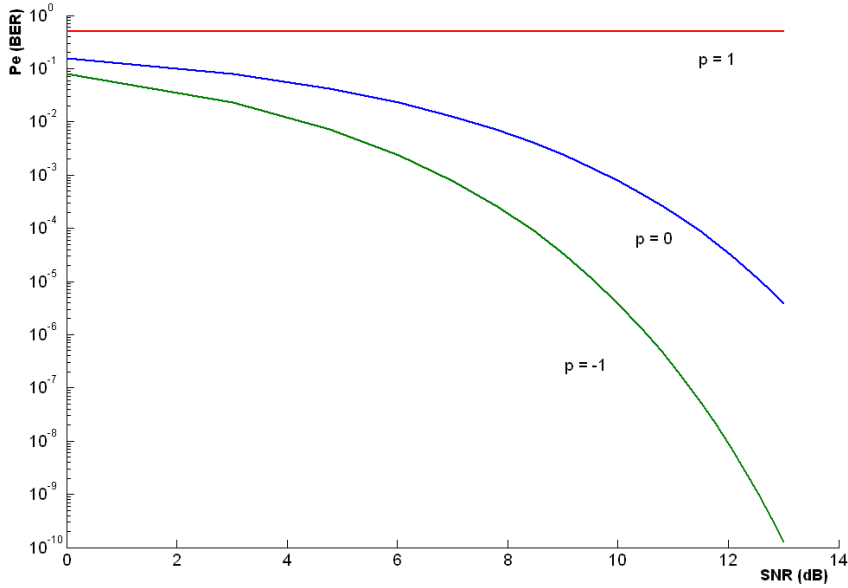


**Figure 2-19:** BER vs. SNR for baseband transmission

If Gaussian noise at the input of the receiver is the dominant cause of bit errors, according to Equation (2-11) we can get higher BER by reducing the SNR. In simulation or real testing, the SNR can be reduced to a known quantity by adding a controllable amount of noise to the test signal. Therefore, we need a high-quality noise generator in order to control the SNR.

### 2.3.2 Simulation and Emulation

Usually, the BER performance of a communication system is first evaluated by software simulation in the early development stage. Simulation tools such as MATLAB and Simulink [46] are therefore used for pre-silicon evaluation. In software simulations, each

component of a communication system, including the communication channel, is represented by a software model that exhibits the characteristics of the represented component. In software-based BER testing scheme, a communication channel is built using a software channel model. The BER performance of the communication system can be easily evaluated by running the simulations under different conditions of SNR.

Although software simulations are easy to set up, they are very time consuming for BER evaluation. The execution is typically done using workstation CPU processors or using acceleration methods. The execution speed depends on the level of abstraction of the simulation models. Due to the vast amounts of data and run-time overhead, simulations generally are only suitable for the evaluation of a system with low BER performance (such as  $\text{BER} > 10^{-6}$ ). For example,  $10^9$  calculation iterations are needed to get an accurate ( $\pm 3.3\%$ ) estimation of a BER around  $10^{-6}$  [47]; a simulation of  $\text{BER}=10^{-8}$  with 10 errors takes days on a personal computer equipped with a 1 GHz Pentium 4 processor. In contrast, acceptable BERs in commercial communication systems (e.g. data transmission) go below 10 errors out of  $10^9$  transmitted bits in many cases. Moreover, many design variables, such as sampling frequency, digital format, etc., have to be optimized while satisfying the best trade-off between performances and complexity, which would further lengthen the simulation process.

In order to speed up the BER evaluation process, performing direct hardware simulation - emulation is proposed. As an alternative to simulation, emulation utilizes FPGAs to re-target all or part of a design. Many software tools and dedicated hardware [48], [49] have been developed with the aim of automating this re-targeting process. In emulation, performance evaluation takes place in hardware, rather than in the virtual environment of a simulator. A hardware-based solution is commonly 100,000 to 1 million times faster than the best simulation software at the same abstraction level [50].

Emulation also makes it possible to run a design at a real time system. This feature is especially important for applications such as the video/audio, where the final output needs to be observed in real time due to the subjective nature of the receiver (the human

eye/ear). If such systems run in real time, the performance of the system can be evaluated on the fly. Otherwise, large test vectors need to be captured and replay mechanisms have to be created, which is much more time-consuming and the evaluation result is less reliable.

Overall, emulation can greatly reduce the evaluation time. Additionally, its real time test capacity can cover a much larger set of test conditions than simulation and hence emulation can enhance the evaluation quality. For these reasons, emulation has been widely used for performance evaluation [51], [52], [53], [54].

### 2.3.3 AWGN Emulation

As discussed in Chapter 2.3.1, the BER performance of a communication system is closely related to the SNR. There exist instruments for BER testing [55], [56], but few integrate an AWGN emulator. Therefore, such testers are difficult to set up for BER testing under the presence of noise. An AWGN generator is needed in order to perform BER performance evaluation under noise conditions.

AWGN generation usually utilizes a variety of statistical techniques. The implementations of AWGN generators are almost always based on transformations or operations performed on uniform random variables [57], [58], [59]. There are a few publications on generating AWGN in digital hardware. The most relevant publications in this area are [47], [60], [61], [62] and [63], which implement AWGN generators in FPGAs.

**CTL Method:** the CLT method exploits the Central Limit Theorem (CLT). According to CLT, if  $X$  is a random variable of mean  $m_x$  and Standard Deviation (SD)  $\delta_x$ , the random variable  $X_N$  defined as

$$X_N = \frac{1}{\delta_x \sqrt{N}} \sum_{i=0}^{N-1} (x_i - m_x)$$

tends toward the Gaussian distribution of zero mean and the unity SD when  $N$  tends toward infinity, where  $x_i$  is  $N$  independent instances of  $X$ .

The CLT method usually employs an accumulator, which greatly slows down the output rate. In addition, implementing a high accuracy AWGN generator using this method needs a large number of random variables. Hence, it is not suitable for high-speed and high accuracy applications. The AWGN generator in [64] uses this method. It produces one output every 12 clock cycles by adding 48 random numbers. Its output rate is 1 MHz.

**Box-Muller Method:** the Box-Muller method [65], shown in Algorithm 1, is the most widely known method for AWGN generation.

1. Generate two independent random values  $x_1$  and  $x_2$ , uniformly distributed over  $[0,1]$ .
2. Obtain:
$$f(x_1) = \sqrt{-\ln(x_1)},$$

$$g(x_2) = \sqrt{2} \cos(2\pi x_2).$$
3. Generate Gaussian variable
$$n = f(x_1) g(x_2).$$

**Algorithm 1: Box-Muller Method**

An FPGA implementation of the Box-Muller method is proposed in [47], where implementing  $\ln$  and  $\cos$  functions requires careful considerations regarding the number of recursions and relative position of points, as well as the precision of implementation. The efficient implementation is therefore not straightforward.

Another disadvantage of the Box-Muller method is that it is not suitable for generating high maximum output values. As indicated in Algorithm 1, the maximum output value of  $n$  is determined by  $f(x)$ , as  $g(x)$  is bounded by  $[-\sqrt{2}, +\sqrt{2}]$ . Since  $f$  approaches infinity when the value of  $x_1$  is close to zero, the maximum output value of  $n$  is determined by the smallest value of  $x_1$ . We express  $x_1$  as  $2^{-t}$ , where  $t$  is the number of bits used to represent  $x_1$  (all bits represent the fractional part). When  $t = 32$ , the maximum output value of the

generator is around 6.7; while  $t$  increases to 64, the maximum value can only increase to 9.4. Obviously, the hardware cost is high and the output speed is limited if we need to achieve good tail distribution using the Box-Muller method.

**Mixed Method:** As presented in [47], the mixed method combines the CLT method and the Box-Muller method for higher accuracy. However, the CLT method slows down the output rate by a factor of  $N$ , where  $N$  is the number of iterations; therefore, the mixed method decreases the AWGN output rate. For the generator proposed in [47], when  $N=4$ , the output rate is only 24.5 MHz, while its clock rate reaches 98 MHz.

**Analog Method:** Even though the above digital implementations of AWGN generators have been successfully realized, converting these multi-bit digital signals to analog signals is challenging – it requires a high performance digital-to-analog converter. Analog Gaussian noise generators are typically realized by low-pass filtering the output of a Linear Feedback Shift Registers (LFSR) or by amplifying the thermal noise of a resistor. These kinds of generators are usually not programmable and not accurate for low BER testing. In [66], a programmable analog Gaussian noise generator is presented. The method encodes a specified Gaussian signal in a RAM, and filters the bit stream using an analog low-pass filter. The performance of the Gaussian noise generator realized in hardware is limited by the size of the available memory that needs to be initialized. Tradeoffs have to be made between the memory size and the signal quality. Typically the generator quality can only be guaranteed within 4 $\delta$ .

**Our Method:** In [67], we present a novel digital implementation of the AWGN generator. Our method combines the Polar method shown in Algorithm 2 with a version of CLT method in a way suitable to maximize the output rate.

As an improvement to the Box-Muller method, the Polar method uses rejection techniques to eliminate the trigonometric calculations that are usually rather slow [57]. It generates two independently distributed Gaussian variables at the same time, which are additionally convenient for applications where two emulators are needed, such as



modeling I and Q channels in wireless communications. The Polar algorithm is faster than the Box-Muller algorithm because it uses fewer transcendental functions, even though it throws away on average 21% of the numbers generated in the Do loop. The proof of validity of the Polar method is elaborated in [65].

- 1. Do**
2. Generate two independent random values,  
 $U_1$  and  $U_2$ , uniformly distributed over  $[0,1]$ .
3. Set:  $V_1 = (2 * U_1) - 1$  and  $V_2 = (2 * U_2) - 1$ .
4. Set:  $S = V_1^2 + V_2^2$ .
5. If  $S \geq 1$ , go back to line 2.
- 6. Loop** until  $S < 1$ .
7. Set:  $W = \sqrt{-2 \ln(s) / s}$ .
8. Generate two Gaussian variables  
 $X_1 = V_1 * W$ ,  
 $X_2 = V_2 * W$ .

**Algorithm 2. Polar Method**

This thesis further investigates the AWGN generation techniques and explores the advantages of our method in BER testing. More details are presented in Chapter 5-4.

---

# Chapter 3 – Accelerating Receiver Jitter Tolerance Testing on ATE

---

Jitter tolerance testing for HSSIs calls for validating BER down to the  $10^{-12}$  or lower. This requirement makes this test extremely time-consuming. It normally takes tens of minutes to a few hours at multiple Gbps data rates. While in the ATE world every test is measured in milliseconds, it is obviously impractical to adopt this test directly. In this chapter, we demonstrate a new technique to perform the jitter tolerance test >1000 times faster. The technique involves extrapolation from the higher BER region down to the  $10^{-12}$  BER level for the compliance test. The thesis proposes a new model suitable to reason about this extrapolation process. Based on the algorithm, we present methodologies to accelerate jitter tolerance characterization and production test.

## 3.1 Introduction

### 3.1.1 Jitter Tolerance Testing

As discussed in Chapter 2.1.2, the CDR is the key differentiator for a serial interface. The overall performance of an HSSI depends on many design choices of the CDR. We have to perform very thorough characterization testing. This includes analysis across PVT corners. The traditional jitter tolerance test has always been very challenging. There are mainly two outstanding issues: the long test time, and the complexity to generate a controlled amount of jitter with the proper mix of different types of jitter [34].

The jitter tolerance test is notorious for its long test time. Since most standards for serial links define jitter tolerance performance down to  $10^{-12}$  BER, we need to run  $10^{13}$  bits to check the BER level. Even at 1.5Gbps data rate, it takes 111 minutes (~2 hours) for the device to run so many bits. That is the fundamental limit for running this test fast. With some applications on the trend demanding  $10^{-14}$  BER, direct measurement is even not practical.

The test time issue becomes much worse when we take into considerations that many design parameters and device settings in the CDR can affect the jitter tolerance performance. One example is the PLL bandwidth. When the jitter frequency in the input data signal is below the PLL bandwidth, the recovered clock can track the input jitter [69] [75]. On the other hand, when the input jitter frequency is above the PLL bandwidth, the jitter gets attenuated more than the lower frequency jitter in the recovered clock. As a result, the jitter tolerance performance is better at lower frequency than that at higher frequency. Jitter tolerance specifications are defined accordingly and Figure 3-1 shows an example the jitter tolerance dependence on the jitter frequency. For SAS,  $f_1$  is 120KHz,  $f_2$  is 1800KHz,  $A_1$  is 0.1UI and  $A_2$  is 1.5UI [76]. Therefore, the jitter tolerance performance needs to be characterized at multiple frequencies, which makes the jitter tolerance testing extremely time-consuming.

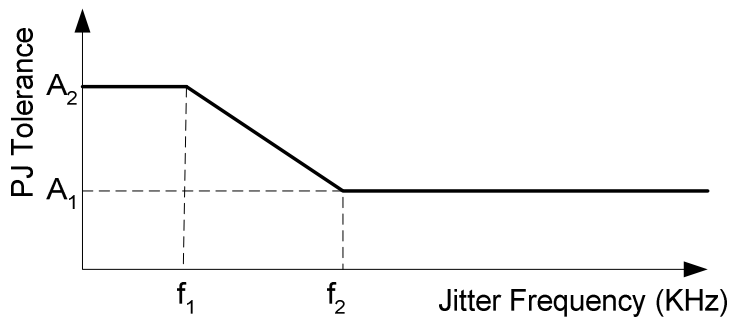


**Figure 3-1:** Jitter tolerance specifications

The second challenge for jitter tolerance test is to generate different kinds of jitter and mix them together. For SATA applications, the jitter tolerance test requires a proper amount of deterministic jitter, random jitter and periodical jitter. This is becoming a norm for most of the point-to-point serial links using backplanes or cables [23], [24], [77], [78].

In SATA, SAS and XAUI applications, there is not much concern about jitter transfer, but a very elaborate jitter tolerance test is required with ISI, DCD and PJ. The reason is that the given transmission media generates these specific jitter types.

Chapter 2.2.3 provides a survey of jitter injection techniques. For laboratory use, we need several instruments to produce the different types of jitter and combine the results [34] [136]. On ATE, supplying the proper mix and amount of jitter is always more challenging. Even though there are existing jitter injection techniques that are targeting on testing HSSIs [41], [42], [44], they usually need extra add-on modules on the testing loadboard or inside the device as a Design-for-Test (DFT) feature. To actually implement them in an ATE environment needs a lot of considerations, such as the loadboard design complexity and the design cycle time increase.

### 3.1.2 Proposed New Method

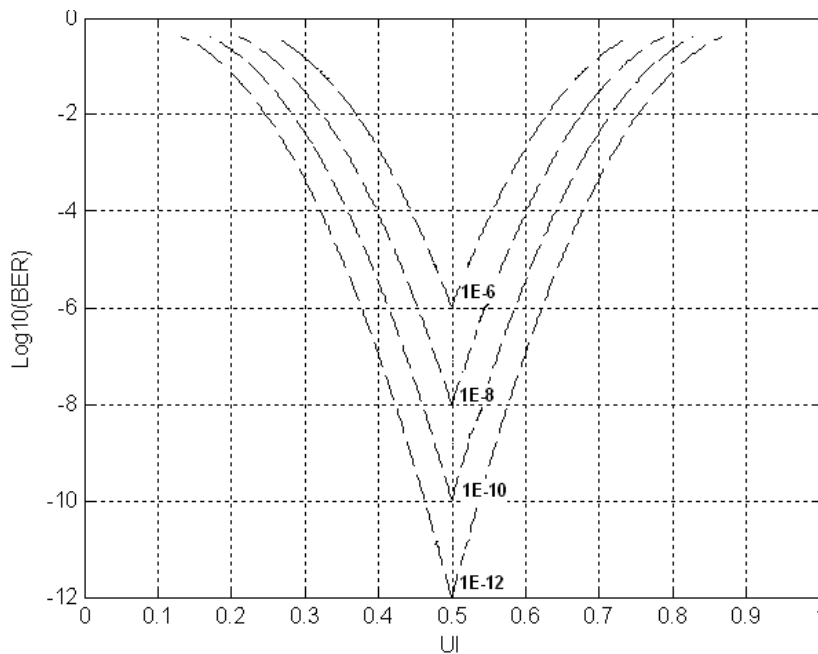


**Figure 3-2:** Conceptual illustration of the jitter tolerance extrapolation

To address the two outstanding issues in jitter tolerance testing, we aim to develop schemes to test jitter tolerance on ATE in a much faster manner. ATE is well known for

its high throughput in production. ATE-based solutions are also more widely being used in validation and characterization, especially for performance analysis across PVT corners on a large sample size. In this chapter, we propose a new approach that can perform the jitter tolerance test >1000 times faster. The approach is straightforward: varying the amount of input jitter to get the receiver into several higher BER levels, and then extrapolating down to the  $10^{-12}$  BER specification for jitter tolerance qualification. The conceptual illustration is shown in Figure 3-2. We will present the concept, assumptions, extrapolation models and experimental data in this chapter.

Jitter tolerance extrapolation is a relatively new subject. We start from borrowing ideas from transmitter jitter measurements. The histogram tail-fitting, real-time sampling and Time Interval Analysis (TIA) approaches require the knowledge of the actual probability density function of the jitter. For the receiver CDR, it is not as accessible as the transmitter. Therefore we can not use them for receiver testing. Only the BER scan (also known as bathtub curve) uses a model based on certain assumptions, which we may use for receiver jitter tolerance testing.

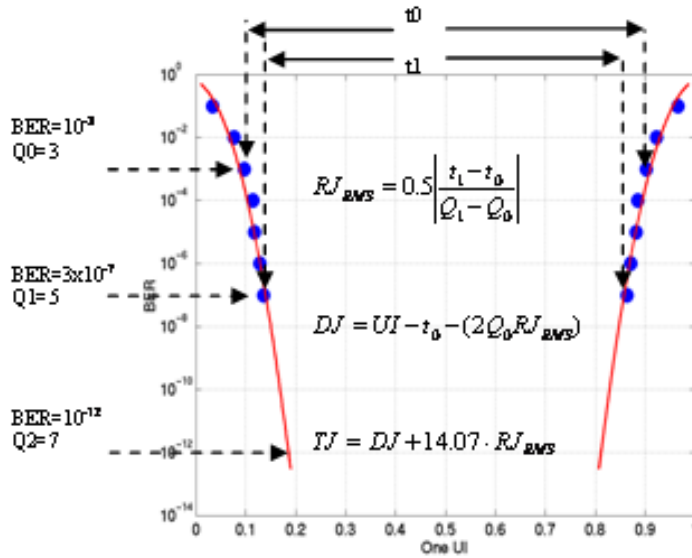


**Figure 3-3:** Transmitter BER scan

In the BER-scan based transmitter jitter measurement approach, a bathtub curve is usually used. The bathtub curve is generated through sweeping the sampling position on the

timing axis and then recording BER at each sampling position. Figure 3-3 shows an example of the bathtub curve. It is actually a plot of data eye openings at various BER thresholds. The finite slope of the bathtub curve is caused by RJ. Obviously, at a lower BER, the eye opening becomes narrower. Figure 3-3 also shows a simplified formula to calculate DJ, RJ and TJ with only two data points recommended by the XAUI standard [34].

In the bathtub based transmitter jitter measurement, all we can see is the combined TJ profile, which is a convolution of the DJ and RJ. We need to work backwards to derive its DJ and RJ components. It is nearly impossible if we do not make some assumptions and use a simple model. The most popular model used is the so called dual Dirac model – assuming that the only DJ is DCD, whose PDF is only comprised of a pair of delta functions [80]. In this case, the complicated convolution is reduced to a standard complementary error function. The dual Dirac assumption serves as the model for modern bathtub curve fitting.

Theoretically the dual Dirac model is not the most flexible one for arbitrary jitter profiles. There are studies on the effect of the DJ profile when deviating from the dual Dirac assumption [80]. However, this seemingly limited model works reasonably well when used appropriately (i.e. proper selection of the curve fitting range). The model is favored by many people because it directly links the jitter to the system level BER performance. The eye openings at lower BER levels can be extrapolated from the openings at high BER levels. The extrapolation results can be verified by performing direct measurements at the lower BER levels. Therefore we borrow ideas from the transmitter BER scan for our jitter tolerance extrapolation.

Similar to the transmitter BER scan, we perform a receiver BER scan. We collect data points at higher BER levels, which takes much less time to do. Then we extrapolate performance to the lower BER range. The extrapolation accuracy can be easily verified by performing the test at the lower BER range, and comparing it to the extrapolation result. If the error is small, then the new method is self validated.

However, there are two significant differences between the receiver BER scan and the transmitter BER scan. Firstly, the receiver BER scan is no longer going to be a bathtub curve fit. We usually can not control the data sampling position in a receiver because the CDR circuitry is designed to sample the data in the mid of each bit. Therefore, the receiver always works at the crossing point of the bathtub curve. The BER of a receiver is associated with the jitter in its input signal. As shown in Figure 3-4, with the increase of the jitter in the input signal, the bathtub curve moves up, indicating a higher BER. What we get is a series of crossed curves, as shown in Figure 3-2. Therefore, a new extrapolation algorithm needs to be developed for the jitter tolerance test.

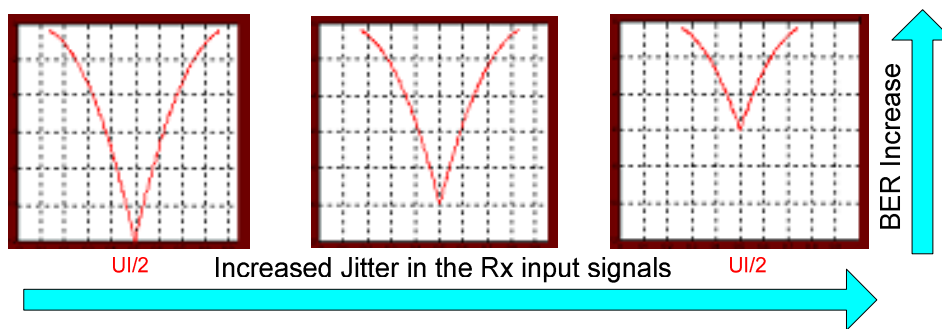


**Figure 3-4:** Receiver BER scan

Another significant difference is that in the receiver BER scan we have control over the jitter PDF of the test signal while we do not have control over the jitter PDF in the transmitter. Normally the HSSI standards define separate DJ, PJ and RJ specifications, but do not define the shape of the jitter probability distribution. In the jitter tolerance test we have some flexibility to shape the jitter PDF. This is an important property because the types of jitter profile can affect the curve-fit accuracy when we use the complementary error function to model the curve [80].

Considering that in the transmitter BER scan, a dual Dirac jitter PDF gives a better curve fit, we choose to inject single tone sine wave jitter to the receiver test signal, which would generate a jitter profile similar to a dual Dirac distribution. As shown in Figure 3-5, there is also a strong tendency to favor the two edges in the sine wave PDF curve. Therefore, it

would be a closer fit to the complementary error function. Another reason to inject the sine wave jitter is that only sinusoidal jitter can provide the worst case jitter to HSSI devices [81]. Sinusoidal jitter is commonly used to perform jitter tolerance testing [82], [83]. Even though in the receiver input signal there are other DJ components (e.g. ISI) that may change the jitter profile a bit, we are not concerned about them. In the transmitter jitter bathtub curve fitting, we can still achieve good accuracy with many kinds of jitter distribution.

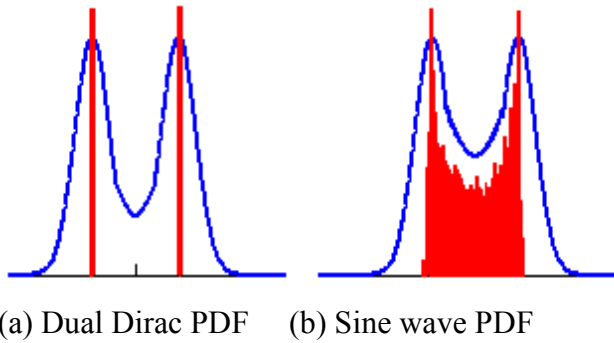


**Figure 3-5:** Jitter PDFs for curve fitting

In this Chapter, we propose to inject the sinusoidal PJ using an AWG available on ATE. We can generate controllable amounts of PJ with only one piece of equipment – AWG. In the receiver BER scan for jitter tolerance testing, the AWG output is directly connected to the input of the receiver as shown in Figure 3-6. By varying the amount of injected PJ, we can get different BER data points.

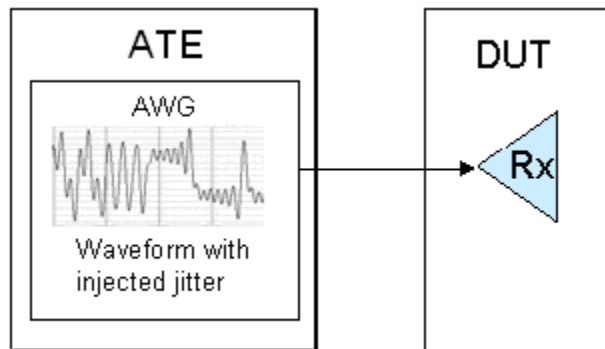


**Figure 3-6:** Test setup for jitter tolerance testing



The test setup of the proposed solution is very simple. There is no intermediate add-on circuit, which means that we do not have to switch off any circuit for the functional test and the input sensitivity test where clean signals (no jitter is injected) are used. The AWG approach can also produce high frequency PJ, like the more modern Voltage-Controlled Delay Line (VCDL) modulators. The high frequency PJ is needed for testing CDR out-of-band jitter tolerance where the CDR can no longer track the input PJ.

In the remaining of the chapter, we will present the details how the test signal is generated, how the bit errors are detected, how we develop an algorithm for jitter tolerance extrapolation and how we use the algorithm to accelerate jitter tolerance qualifications.

## **3.2 Jitter Test Signal Generation**

On ATE, there are mainly two types of instruments that can do GHz receiver testing: AWGs and binary digital pattern generators. Generally, binary digital pattern generators such as Teradyne SPQ [84] and Agilent/Verigy NP3G [85], can provide higher analog port count, suitable for multiple serial interface testing. However, an AWG-based approach provides us more controllability to the signal it generates, including jitter injection and multiple-level amplitude manipulation. In addition, AWG-based solutions exhibit more capabilities in testing other analog blocks: the same instrument can be used to provide test signals for other blocks, such as amplifier and ADC. This is especially attractive for SoCs, which have a very limited number of HSSIs (typically 1 or 2), but have many other analog blocks. AWG-based approaches can provide better overall cost efficiency in this application. This chapter concentrates on the AWG-based approach. Testing solutions for multiple-port applications, such as in networking and switching devices are discussed in Chapter 5.2.

To perform a jitter tolerance test, we need source signals with controllable jitter. In our implementation, the source signals are generated by modulating ideal AWG binary signals with a user defined jitter profile. Generally speaking, we can source any

waveform with spectral content limited to the Nyquist band. The jitter injection does not require additional instruments as in some other setups [78], [86], [87].

With the state of the art AWG on ATE – 6G samples/s and 2.0GHz analog bandwidth, we have 2 samples per bit for 3 Gbps data. By manipulating the sample timing and amplitude, we can inject controllable amount of jitter to the test signals. Using the AWG6000, we can do receiver jitter tolerance testing for data up to 3Gbps and receiver function testing for data up to 6Gbps. The main point of our jitter injection mechanism is to modulate jitter-free data edges using a jitter signal. Oversampling, FFT and downsampling techniques are used to achieve quality test signals with desired jitter resolution. The generated signals are essential to characterize the jitter tolerance performance along with other receiver parameters. The following section describes the details of the jitter injection scheme.

### **3.2.1 Choosing Test Signal Parameters**

In our implementation, AWG6000 is used and its sample rate is set to 6GHz. Each data bit has two samples for 3Gbps signals and four samples for 1.5Gbps signals. The AWG6000 can also be used to generate test signals with non-integer samples per bit, such as for the 5.5Gbps application discussed in Chapter 3.2.3. The following jitter injection discussion is based on 1.5Gbps SATA applications; the principle is the same for 3Gbps or other applications, but minor changes are needed based on the specific requirement.

To generate test signals with controllable amount of jitter for jitter tolerance testing, we need to properly choose or set the following parameters:

- Test pattern
- Length of the test signal
- Jitter signal
- Jitter injection resolution

As for the test pattern, it should be able to represent the patterns in real applications. Pseudo Random Bit Sequence (PRBS) patterns have been widely accepted to test different communication interfaces because they have different run lengths and hence provide very good test coverage for possible data combinations. For SATA applications, the maximum run-length is 7. Therefore, we choose the standard 128-PRBS pattern, which has a maximum run-length of 7. Figure 3-7 shows the 128-PRBS sequence. The 128-PRBS covers all run-lengths from 1 to 7. There are totally 63 transition edges in the test pattern. We inject jitter to the PRBS signal through modulating these transition edges. The injected jitter can have any arbitrary profile. In this section, we demonstrate how different amounts of sinusoidal jitter are injected to the data signal.

**Figure 3-7: The 128-PRBS sequence**

Because the length of an AWG sequence is finite, the test signal (including data and jitter) is generated by running the AWG pattern continuously. The injected jitter signal needs to be coherent with the data pattern stored in the AWG. In [2], we modulate one cycle of the

128-bit PRBS data pattern using a sinusoidal signal. The generated test signal exhibits the exact amount of PJ as we expected according to the calibration result from standalone lab equipment. However, with the test signal, ATE reports better jitter tolerance performance than that observed on bench equipment when we characterize some special devices using the same 128-bit PRBS pattern. Further experiments demonstrate that the difference is caused by different jitter injection mechanisms between the bench and the ATE. On bench, the PJ signal and the un-modulated data signal are asynchronous -- each edge of the data signal can be modulated up to 100% of the injected PJ peak value. On ATE, the jitter and the un-modulated data signal are always synchronous: the jitter at each of the 63 edges of the 128-bit PRBS pattern is a constant. Therefore, not every edge has a chance to be modulated with the peak value of the injected PJ signal -- some edges even do not move.

We overcome the issue by increasing the length of the ATE test pattern. If the movement of each edge of the test signal can reach or nearly reach the PJ peak value, the bench test signal is emulated. For this reason, along with the ATE memory source availability and FFT requirements, we increase the length of the test pattern by repeating the 128-bit PRBS pattern  $2^n$  times, where  $n$  is an integer. We then modulate the long test pattern using a sinusoid jitter signal with an odd number of cycles. This can greatly increase the randomness of the edge movement for each edge of 128-bit PRBS pattern.

Our calculation shows that a good choice is to use a 1024-bit test pattern (constructed by repeating the 128-bit PRBS pattern eight times) and then to modulate the test pattern using a sinusoid PJ signal with 39 cycles. In the generated test signal, each edge of the 128-bit PRBS can reach at least 92% of the injected PJ peak value, which is very close to the bench test signal. Even though further increasing the length of the test pattern can slightly further increase the randomness of the edge modulation, choosing 1024 bits is a good tradeoff between the randomness and the AWG memory usage (we need to store multiple test signals in the AWG for jitter tolerance characterization and other testing).

When 1024-bit test signals are used in 3Gbps applications, the FFT frequency resolution is given by

$$f_{avg\_FFT\_res} = \frac{3000MHz}{1024} = 2.9296875MHz$$

We can inject any sinusoidal jitter signal that is a multiple of  $f_{avg\_FFT\_res}$ . Lower frequency jitter can be injected by increasing the length of the test pattern. In our experiments, we investigate the jitter tolerance characteristics at different frequencies while concentrating on the jitter frequency of 114.2578125MHz (= 39 x 2.9296875MHz) for most of our work. At this frequency, the generated test signal exhibits very good randomness of edge modulation. This frequency is also a good representative of the out-of-band frequency in SATA, whose range is from 6MHz to 300MHz [22].

### 3.2.2 Periodic Jitter Injection

We inject jitter to the jitter-free data signal by modulating the ideal data edges -- moving them forward when the jitter is positive or backwards when the jitter is negative. The process of jitter injection consists of the following five steps:

#### 3.2.2.1 Creating Jitter-Free Data Signal

The jitter resolution of the modulated data signal is directly determined by the time resolution of the data edges. For instruments such as AWG6000, the maximum sampling rate is 6G samples/s. Each data bit can have two samples for 3Gbps signals and four samples for 1.5Gbps signals. If we directly manipulate the edge transitions, the jitter resolution is only 0.25UI even with the 1.5Gbps signals because each AWG sample represents 0.25UI. We cannot use this approach to perform jitter tolerance testing because pico-second jitter resolution is required.

One solution is to oversample the jitter-free data signal to pico-second resolution. Considering the requirement of FFT that we will perform later, we need to choose the oversampling rate to be a power of 2. For the 1.5Gbps signal, one UI is 667ps. We can

choose an oversampling rate of 512 samples per bit, which translates into a jitter resolution of 1.3ps. Figure 3-8 shows one cycle waveform of the 128-bit PRBS jitter free data signal *oversampled\_data* oversampled with 512 samples per bit.

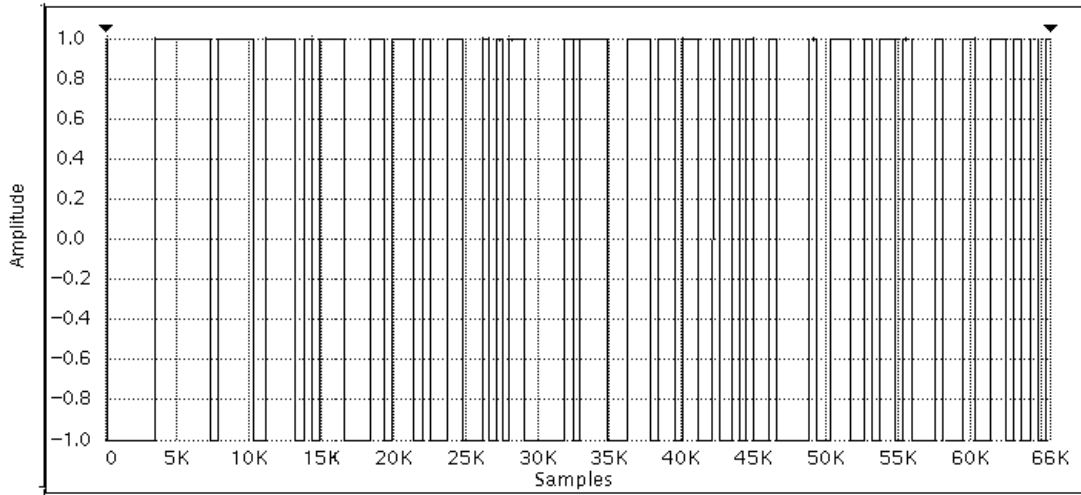


**Figure 3-8:** Oversampled jitter-free data signal

### 3.2.2.2 Creating a Digitized Jitter Signal

Now we have created the jitter-free data signal. Next, we need to modulate the data edges in order to convert jitter amplitude information to timing information. This is done by moving the edge of the data signal based on the jitter amplitude information. Therefore, we need to create a digitized PJ signal to modulate the ideal data edges.

A sinusoidal jitter signal can be characterized by two parameters: the frequency and the amplitude. The frequency can be represented by  $pj\_bin * f_{avg\_FFT\_res}$ , where  $pj\_bin$  is the PJ frequency bin. The amplitude is the PJ peak value  $amp\_UI$ , which is the maximum edge displacement in the modulated data signal. Based on the jitter parameters, the digitized jitter signal  $jitter[i]$  can be represented by

$$jitter[i] = amp\_UI * \sin(2 * M\_PI * i * pj\_bin / 1024 + M\_PI / 2)$$

where  $i$  is the sample index and  $i \in [0, 1023]$ ,  $amp\_UI$  is the jitter amplitude measured in UI,  $pj\_bin$  is the jitter frequency bin and  $M\_PI$  is the constant 3.14159....

The jitter amplitude is measured in UI. Therefore the value of  $jitter[i]$  represents the data edge displacement in UI at data bit  $i$ . As the data signal is oversampled with 512 samples per bit, the data edge timing resolution is UI/512. To convert the jitter into data edge time displacement, we need to oversample the  $jitter[i]$  with a resolution of UI/512, which gives

$$oversampled\_jitter[i] = 512 * jitter[i]$$

where  $oversampled\_jitter[i]$  represents the number of samples that the data edge needs to be pushed back or forwards.

For the 1.5Gbps signal, one UI is 667ps and each data bit is oversampled by 512. If we set the jitter peak-to-peak value to 400ps, the jitter amplitude  $amp\_UI$  is 0.3UI,  $jitter[i]$  is between 0.3 and -0.3, and  $oversampled\_jitter[i]$  is between 153 and -153.

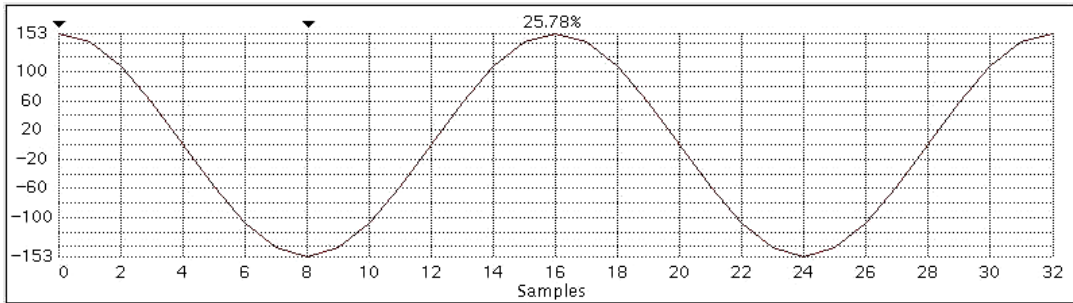
### 3.2.2.3 Modulating the Data Signal

Each bit of the oversampled data is then modulated by the oversampled jitter signal. The following demonstrates how the modulation is done:

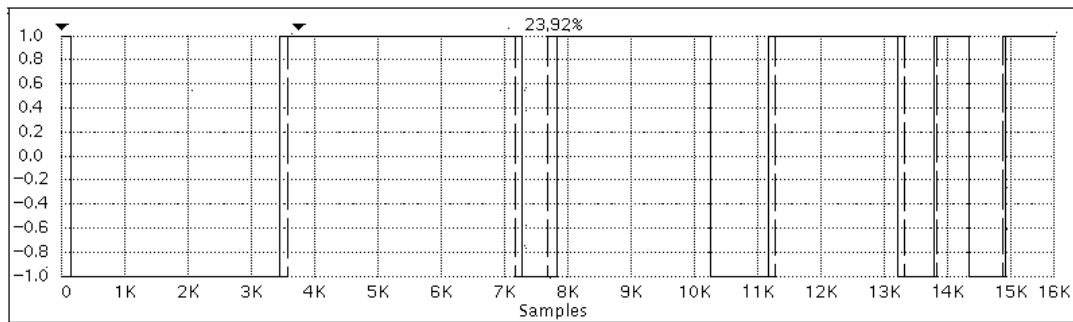
```
for (i=0; i<=1024; i++)
{
    if oversampled_jitter[i] > 0
    { oversampled_data[i*512] ~ oversampled_data[i*512+oversampled_jitter[i]]
      is replaced by oversampled_data[(i-1)*512]           //push the edge later
    }
    else
    { oversampled_data[i*512-oversampled_jitter[i]] ~ oversampled_data[i*512]
      is replace by oversampled_data[i*512]                 //pull the edge earlier
    }
}
```

Figure 3-9 illustrates the first 32 bits of the data signal and the jitter signal. The amplitude of the jitter signal is scaled by the oversampling rate 512, and the amplitude of the data signal is normalized to 1.0. The data signal has been oversampled by 512 and modulated

by the jitter signal. At the first transition edge (bit 7), the jitter is negative, so we pull the transition edge earlier; at the second edge, the jitter is positive, so we push the transition edge later; for the fourth edge, the jitter is 0, so the transition edge does not change.



(a). Jitter signal *oversampled\_jitter*:  $V_{pp} = 0.6 \text{ UI}$ , resolution =  $\text{UI}/512$



(b). Data signal: jitter-free data (broken line) and jittered-data (solid line)

**Figure 3-9:** Jitter signal and modulated data signal

### 3.2.2.4 Generating Bandwidth Limited Signals

The above oversampled jittered data signal is an ideal signal that has zero transition time: it contains infinite spectrum and does not suffer from any bandwidth limitation. However, the actual AWG we use only has a bandwidth around 2G, and its maximum sampling rate is 6G samples per second. In order to retain the jitter and maximize the signal to noise ratio, we use two techniques: one is to smoothen the transition edges and another to bandwidth-limit the signal.

To smoothen the transition edges, we add a transition time. In this example, we set the transition time from rail to rail to be  $0.8\text{UI}$  (410 samples). At this step, the transition is



linear. Band-limited filtering in the following step will generate the signal with “real” transitions. Figure 3-10 shows the data signal with linear transitions.

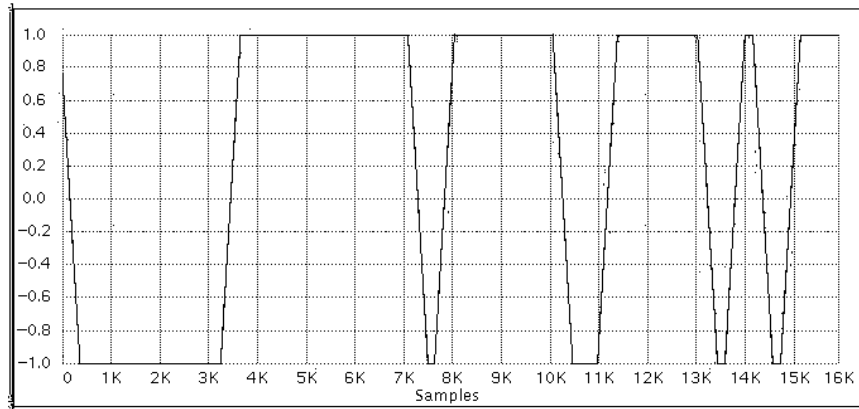


**Figure 3-10:** Adding edge transition time

To bandwidth-limit the modulated signal, we need first to get the magnitude frequency response and phase response of the data signal. This can be achieved by performing FFT on the modulated oversampled data samples. Figure 3-11 shows frequency spectrum of the modulated data signal, where only the first 160 bins of the total of 262144 bins are displayed.

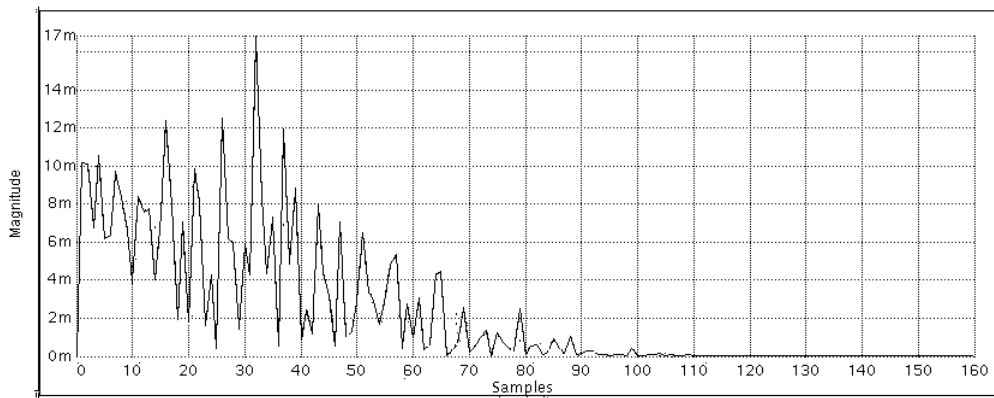


**Figure 3-11:** Frequency spectrum of the oversampled data signal

We limit the bandwidth of the generated signal to 3GHz because the AWG sampling rate is 6GHz. Therefore we filter out all frequency components above the Nyquist frequency by setting all the frequency bins above 1024 to 0. By performing an inverse FFT

operation, we can get the time domain data. Figure 3-12 shows the waveform of one cycle of the 128-prbs pattern after the inverse FFT operation.

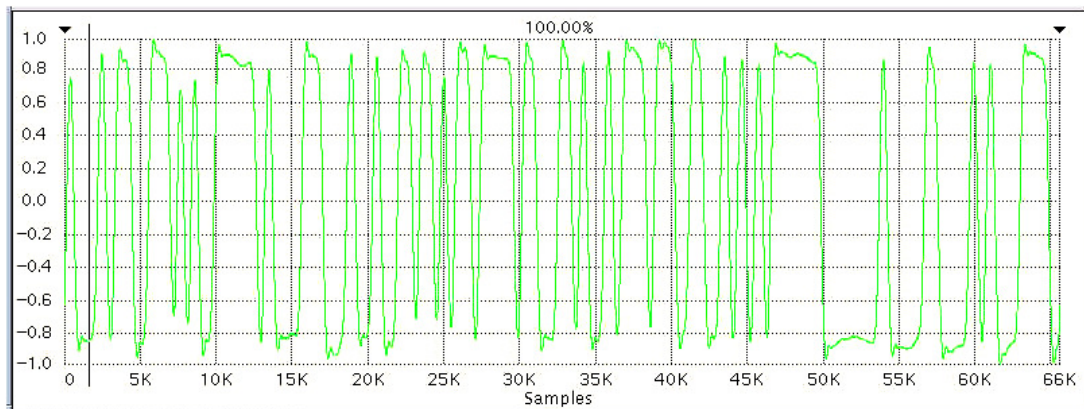


**Figure 3-12:** Time domain data after the inverse FFT

### 3.2.2.5 Downsampling to Get AWG Samples

The data after the above manipulation is still oversampled with 512 samples per bit. If we directly store the oversampled data in the AWG for 1.5Gbps application, the AWG sampling rate needs to be as high as 768GHz. Because the AWG sampling rate is limited to 6GHz, we need to decimate the waveform to get the desired AWG samples. For 1.5Gbps applications, we need to keep 4 samples out of 512 samples (one data bit), which translates into a downsampling rate of 128. Figure 3-13 shows the waveform of 128 bits of the final data signal we generate, where each bit has 4 samples. This data can be directly stored in the AWG memory.

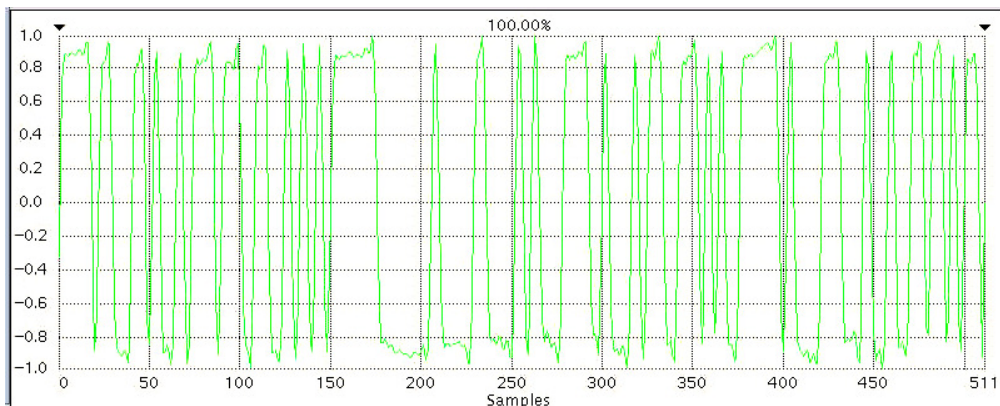


**Figure 3-13:** AWG waveform – data after under-sampling

With 4 samples per bit, the 1024-bit test signal takes 4k AWG sample source memory. Because the AWG6000 has 32M sample source memory, we can use one AWG to store multiple jittered test signals, which are needed when we sweep the test signals to characterize the jitter tolerance performance. The same AWG can still be used to store other waveforms to test other blocks in an SoC. In addition, we can test multiple HSSIs in parallel if we have multiple AWGs.

### 3.2.3 Fractional Sampling

The test signal generation scheme discussed previously is based on integer sampling – each data bit has an integer number of samples in the AWG6000, such as 2 samples per bit for 3Gbps signals and 4 samples per bit for 1.5Gbps signals when the sampling rate is set at 6G samples per second. Normally there is only a limited range of sampling frequencies that we can set for the AWG in order to optimize the AWG performance. For example, for the AWG6000 we used, the sampling frequency can only be set to between 5.8G~6.2G or below 5G. If the sampling rate cannot be set to a multiple of the data rate we need to investigate, fractional sampling has to be used - each data bit has a non-integer number of samples. For example, if we need to investigate a 2.75Gbps application, we need to use fractional sampling because the AWG sampling rate cannot be set to 5.5G. This section presents a method to generate test signals with fractional sampling. The following demonstrates how the test signals for the 2.75Gbps application are generated using the 6G sampling rate.

When the AWG sampling rate  $f_{avg}$  is set to 6G and the input data rate  $f_{in}$  is 2.75Gbps, each data bit needs to be sampled by

$$\frac{f_{AWG}}{f_{in}} = \frac{6.0}{2.75} = \frac{24}{11} \quad (3-10)$$

which shows that every 11 data bits need 24 AWG samples. Therefore, the length of the data pattern needs to be a multiple of 11. For example, if we want to use a 160-bit test

pattern, we need to repeat the 160-bit pattern 11 times, which means we need to increase the test pattern to 1760 bits and the number of AWG samples should be 3840 according to

$$\frac{f_{AWG}}{f_{in}} = \frac{24}{11} = \frac{24 * 160}{11 * 160} = \frac{3840}{1760}$$

To convert 1760 bits of data into 3840 AWG samples, we propose the following procedure:

- 1) Oversampling the data by a multiple of 24 (derived from Equation (3-10)). We can choose an oversampling rate of 240. This oversampling translates into a resolution around 1.5ps for the 2.75Gbps data signal
- 2) Performing an FFT on the 1760 bits data oversampled by 240 (the total number of samples is 422400) to convert the time-domain data into frequency domain data
- 3) Modulating the data edge using a jitter signal if needed using the procedure discussed in Chapter 3.2.2
- 4) Filtering out all the frequency components above 3GHz by setting these frequency bins to zero
- 5) Performing an inverse FFT to convert the band-limited frequency domain data into time-domain data
- 6) Downsampling the time-domain data by 110 to get the 3840 AWG samples

If we run the AWG with the generated AWG samples continuously and set the sampling frequency to 6G, the AWG would generate a 2.75Gbps data signal as we need. It is equivalent to that each data bit has 2 and  $\frac{2}{11}$  AWG samples. For other data rate applications, we only need to adjust the oversampling and downsampling ratio based on  $f_{AWG}$  and  $f_{in}$  when applying the above procedure.

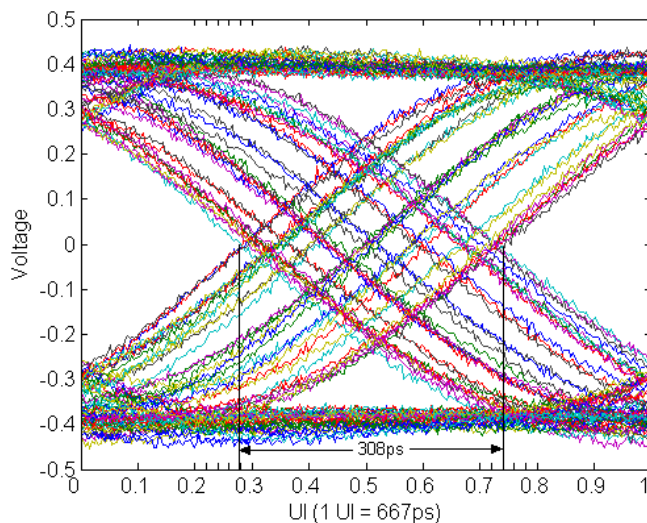
### 3.2.4 Jitter Calibration

We thoroughly calibrate the generated test signals for two reasons. The first one is to verify our jitter injection technique. Secondly, we use the calibration results to link the

injected PJ to DJ and TJ because most HSSI standards define DJ and TJ tolerance specifications separately and we control the DJ and TJ through the injected PJ.

The jitter injection technique is verified by extracting the actual jitter in the generated signal and then comparing it with the injected value. There are three approaches we can use for the verification. The quickest approach is to plot the eye diagram according to the test signal data stored in the AWG. Another approach is to use a digitizer on the ATE to capture the AWG output signal and then extract the jitter information. The jitter in the generated test signal can further be calibrated using bench equipment.

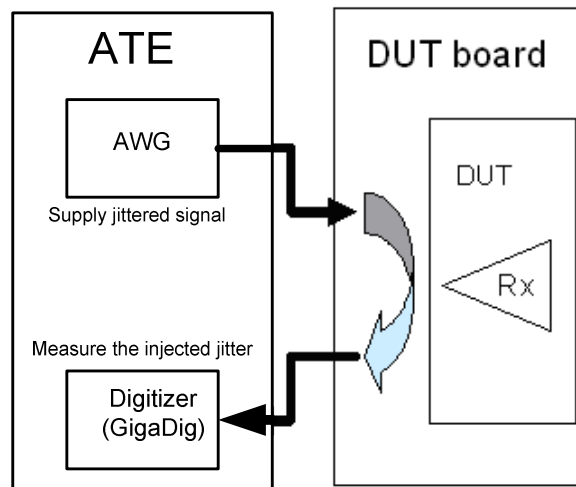
We first verify our jitter injection technique using eye diagrams. Figure 3-14 captures the eye diagram of a 1.5Gbps test signal with 300ps PJ injected. The diagram is generated by overlaying the data samples stored in the AWG in one UI interval, and the figure is plotted in MATLAB. As we can see, the eye closure is very close to the amount of PJ we injected. Without the need for any instrument, the eye-diagram can be generated and used to verify the concept of our jitter injection technique.



**Figure 3-14:** The eye diagram of the AWG samples with 300ps PJ injected

We can calibrate the amount of injected jitter on ATE by connecting the AWG output to the input of a high bandwidth digitizer, such as the GigaDig available on Teradyne

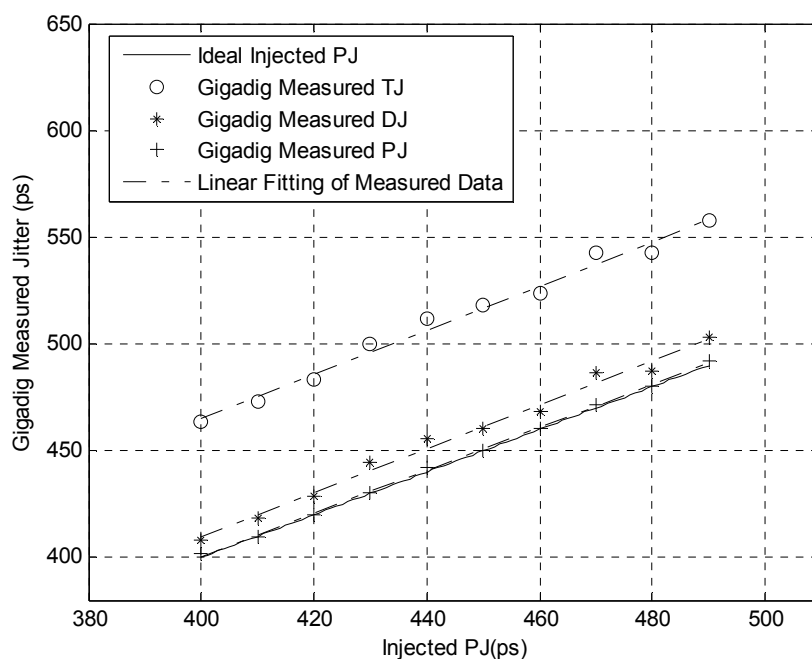
Catalyst/Tiger ATE. Figure 3-15 shows the connection used to calibrate the injected jitter on ATE. We use the digitizer to capture the AWG output and we then extract the jitter components from the captured waveform [4]. The details on how the jitter components are extracted are discussed in Chapter 4.



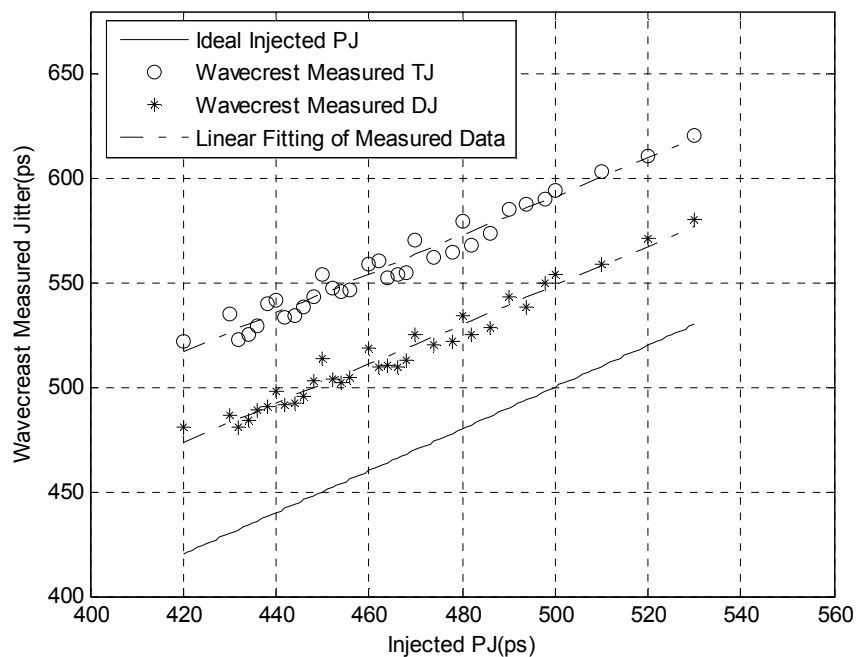
**Figure 3-15:** Test setup for jitter calibration on ATE

Figure 3-16 plots the jitter calibration result using the ATE. The horizontal axis is the injected PJ and the vertical axis is the measured jitter. As we can see, the measured PJ correlates well with the ideal injected PJ. We have a good linear control on the injected jitter. DJ and TJ are also recorded. There is a small offset between the injected PJ and the measured DJ, which is contributed by other DJ components. The offset between the measured DJ and the measured TJ is caused by intrinsic RJ of the AWG.

To further confidently report the jitter numbers, we used a Wavecrest SIA-3000 to calibrate the TJ, RJ and DJ numbers in the generated test signals. Figure 3-17 plots the measurement results. Similar to the ATE jitter measurement results shown in Figure 3-16, the Wavecrest measured DJ and TJ are tracking the injected PJ. The constant vertical offset between the measured TJ and the injected PJ is caused by the intrinsic RJ, DCD and ISI from the AWG and the connection cables. In this example, the offset between the PJ and TJ is around 92 ps.



**Figure 3-16:** Jitter injection calibration curves with the digitizer



**Figure 3-17:** Jitter injection calibration curves with Wavecrest SIA-3000

Figure 3-17 demonstrates that in our test signals PJ and TJ are related by a constant offset. Therefore, we can translate the TJ tolerance testing into PJ tolerance testing once we know the offset. This is important because on ATE we can only accurately generate controllable amount of PJ due to the AWG memory limitation. The final jitter tolerance number we report will be derived from the calibration curve shown in Figure 3-17.

### 3.2.5 Random Jitter Control

Even though we cannot deliberately inject controllable amount of RJ to the AWG signal due to the size limitation of the AWG memory, we propose an approach to control the RJ in the test signals. The approach utilizes the characteristics of the AWG driver. In Figure 3-17, the offset between the measured DJ and TJ is caused by the intrinsic RJ of the AWG. Because the AWG output signal has a constant rise/fall time, the intrinsic RJ would vary at different output amplitude levels: RJ increases when the signal amplitude decreases and decreases when the signal amplitude increases. Figure 3-18 shows the captured RJ RMS values at amplitude levels from 230~780mV using the Wavecrest SIA-3000. Therefore, we can control the RJ of our test signals by controlling the amplitude of the AWG output signal, which is programmable on the ATE.

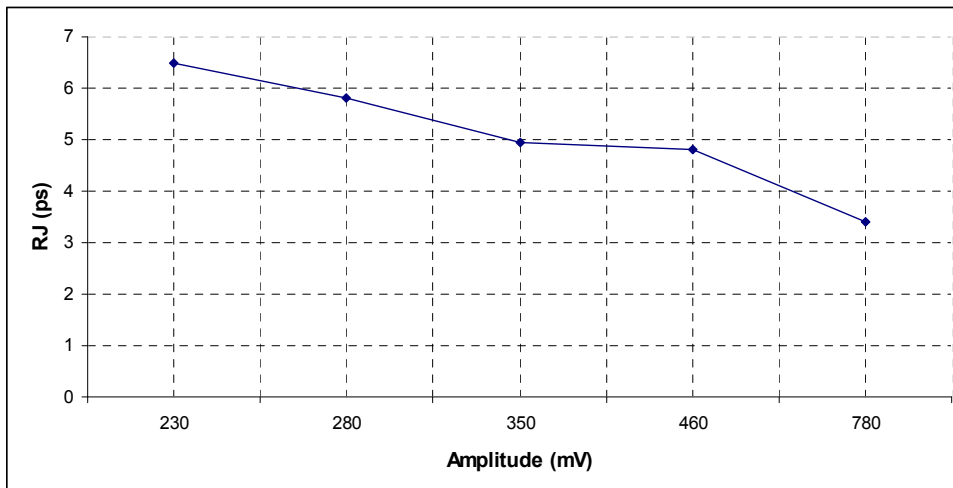


**Figure 3-18:** RJ vs. AWG output amplitude



According to the SATA jitter tolerance specification shown in Table 2-5, the difference between the out-of-band DJ and TJ for Gen1 SATA is 0.25UI. The difference suggests that a test signal with a 0.25UI RJ peak-to-peak value is the best candidate to perform both DJ and TJ compliance tests at the same time. This RJ peak-to-peak value translates into a 5.92ps RMS value. According to Figure 3-18, setting the amplitude to around 280mv is the most reasonable setting for the jitter tolerance compliance testing using the generated test signals. This amplitude is also very reasonable as it covers the lower end of the SATA receiver amplitude range, which is from 250mv to 700mv. The low end amplitude is more stringent as it is less immune to noise.

### **3.3 Receiver Bit Error Monitoring**

When the jittered test signals are applied to the receiver, bit errors may occur in the recovered data. Jitter tolerance testing is done by supplying a test signal with a certain amount of injected jitter to the receiver and then monitoring the bit errors in the recovered data to check whether the BER is below a certain level. The receiver error rate can be monitored using several methods. One approach is to loop back the received parallel data signals to the transmitter and then check the bit errors from the output of the transmitter. This approach usually needs a high speed BERT, which is not available on ATE. The under-sampler on the ATE is not a good candidate for BER measurement. In addition, the transmitter itself might introduce errors, which makes it hard to justify the jitter tolerance test results. Therefore, we need to use alternative approaches. This chapter presents two approaches based on available ATE instruments or DFT features. Chapter 5.1 introduces another approach based on FPGAs.

#### **3.3.1 ATE-based Error Detection**

The solution is to bring out the recovered parallel data signals to device pins, and then compare the outputs of these pins with expected values in a digital pattern. Figure 3-19 shows the testing configuration of this approach.

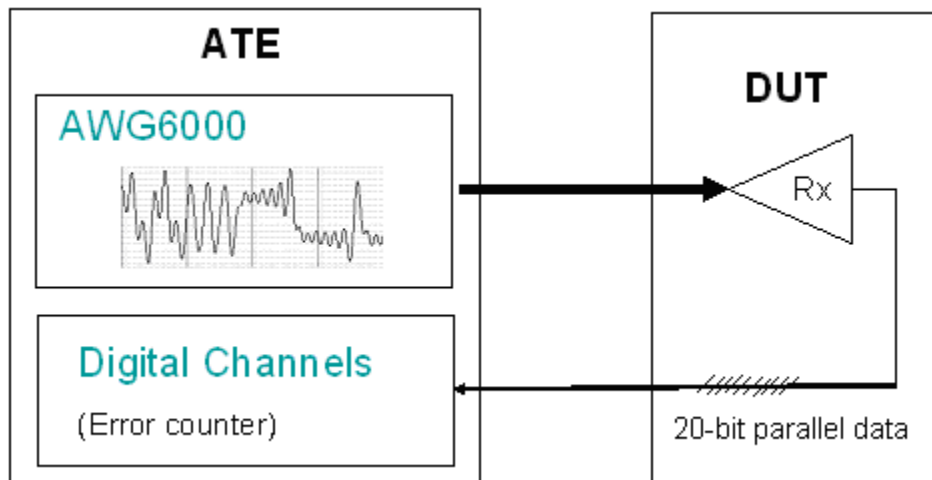


**Figure 3-19: ATE-based BERT**

The number of errors on each pin can be accessed by reading back the error counter of the High Speed Digital (HSD) channel associated to the parallel output pin. The error counter is essentially a byproduct of the failure capture memory. It keeps track of how many pattern cycles the fail flag has been asserted from the last HSD reset or counter clear to the time the counter is read. Each failure counter is 16 bits in width. In our devices, the parallel data are 20 bits in width. The maximum number of errors the ATE can track is more than 1 million, which is enough to suppress the statistical variation and allow a generous step size on incrementing the jitter injection amount. This is important because we need to obtain multiple BER points for extrapolation, but the performance (and hence the error rate) can vary from device to device at the same injected jitter level.

One challenging issue of using the parallel data bus for error counting is the synchronization. Because the AWG and digital channels on ATE are in two clock domains, clock synchronization is a priority. Considering the two domains are generated from the same clock source on ATE, clock synchronization can be achieved by properly setting the two clock dividers such that the two frequencies are coherent and the receiver can work correctly. The receiver reference clock uses the same clock signal as the digital channels on ATE. The digital channel strobe is set centered on the parallel data of the receiver output. The byte (i.e. word boundary) alignment is becoming a norm for almost all devices. The frame alignment character is detected by the receiver to ensure that the

right sequence of a word (from LSB to MSB) comes out of the parallel bus in a consistent way, from run to run, and from device to device. For pattern alignment, because the delay from the input of the receiver to the output of the receiver varies from device to device, we use a match loop to line up to the repeating PRBS pattern. As shown in Figure 3-20, the match loop skips byte-by-byte to search expected parallel data. Once an expected parallel data sequence is detected (the parallel data bus is aligned to the AWG serial output sequence), the pattern jumps out of the match loop and the HSD channels start checking errors.

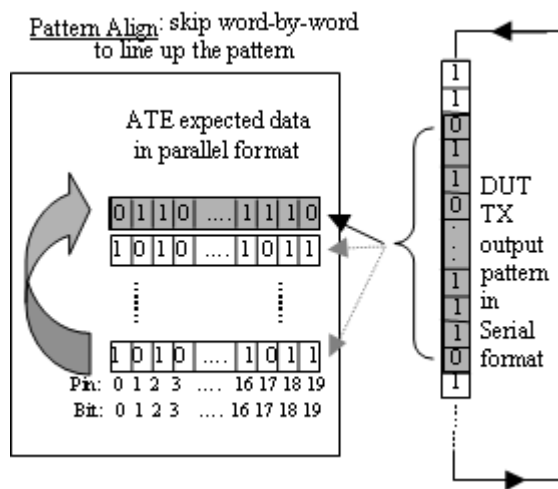


**Figure 3-20:** Pattern alignment between the serial data and the parallel data

We can vary the length of the error checking pattern to get the BER with an expected confidence level. A longer length pattern provides a higher confidence level, but takes more test time. By sourcing test signals with different amounts of injected jitter, we can get different bit error rates.

### 3.3.2 DFT-based Error Detection

The ATE-based BERT is complicated to implement because it involves external synchronization. The BER testing can be simplified by adding DFT features. DFT has been widely used in devices manufactured today in order to reduce testing cost or removing the need for expensive testers. Researchers have proposed Built-in-Self-Test

(BIST) techniques specifically tailored for testing common designs, such as bit error checkers [87], ADCs [88] and PLLs [89].

The idea of DFT-based error detection approach is to implement a BERT inside the device. The internal BERT includes a pattern generator and an error counter muxed with transmitter and receiver latches. Figure 3-21 illustrates the concept of the DFT feature [87]. The pattern generator generates test sequences, such as the 128-PRBS pattern as we used. When the test signals applied to the receiver have the same sequence as the one generated by the pattern generator, the internal checker can record the errors that have occurred after the synchronization is achieved.

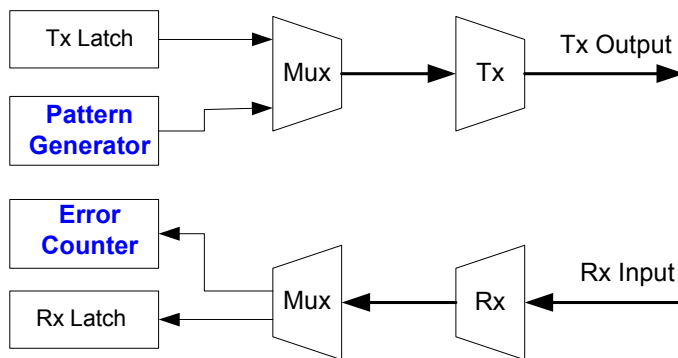


**Figure 3-21:** Conceptual illustration of the DFT-based BERT

This approach is widely used in HSSI designs because it simplifies the verification and testing process with little extra design cost. With the built-in BERT, loopback testing can easily be implemented. For receiver function verification, only a small error counter, such as a 4-bit counter, needs to be implemented in the checker. The receiver function can be verified by just checking the contents of the error counters in the checker after the synchronization is achieved: if the number of errors is zero, the receiver functions correctly; otherwise, it fails.

For BER testing, the range of the error counter needs to be big enough to avoid the error counter getting saturated quickly when the error rate is high. The jitter tolerance testing requires us to sweep the input signals with different amounts of injected jitter. The BERs

may range from  $10^{-5}$ ~ $10^{-12}$ . To accommodate such a wide BER range, the error counter needs to be bigger than  $10^7$ . Therefore, the width of the error counter should be 24 bits or more for jitter tolerance characterization. By reading back the values in all the error counter registers, we know the total number of errors. The BER is measured by calculating the ratio between the total number of errors and the total number of tested bits.

### 3.4 Jitter Tolerance Extrapolation

As discussed in Chapter 3.1.2, we can not use the transmitter bathtub curve fitting technique for receiver jitter tolerance testing. We need to develop a new algorithm for jitter tolerance extrapolation.

#### 3.4.1 Jitter Tolerance Extrapolation Algorithm

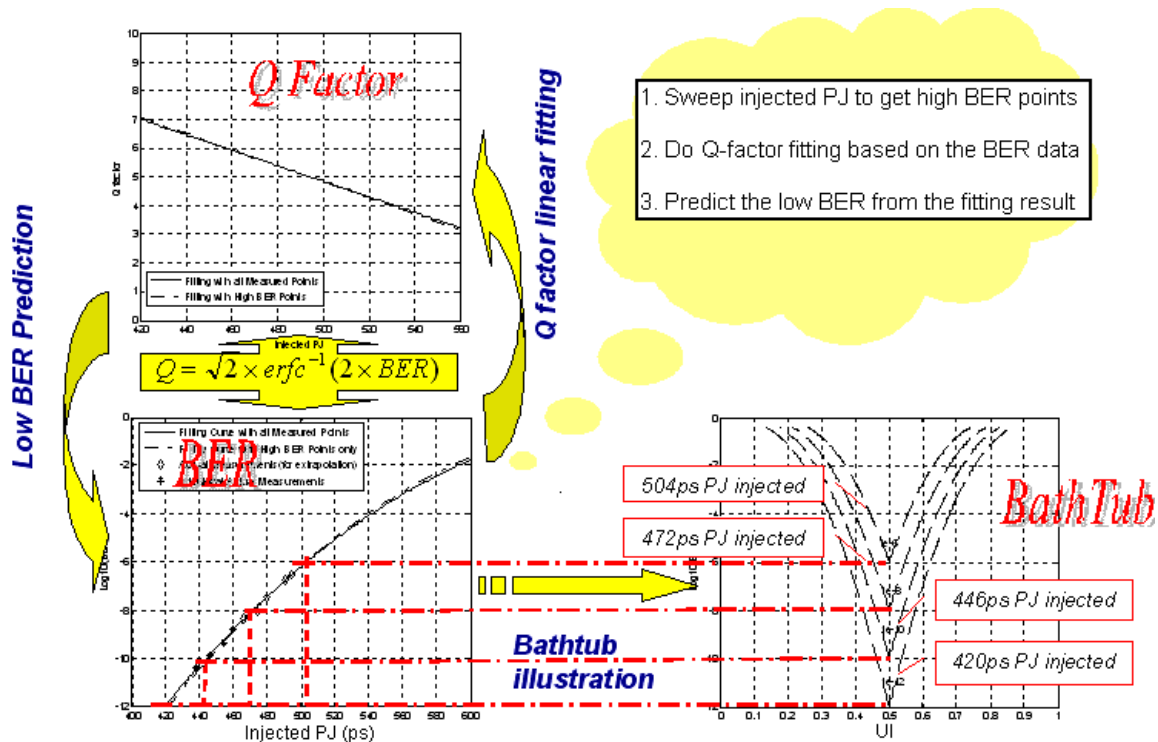


**Figure 3-22:** Overview of the jitter tolerance extrapolation

The goal of jitter tolerance extrapolation is to predict the jitter tolerance at low BER based on high BER region data. Figure 3-22 illustrates the jitter extrapolation process. We

sweep the injected PJ in small increments to get several high BER levels, which can be obtained quickly. In Figure 3-22, the right-bottom plot shows the bathtub curves of these BER levels; the left bottom plot shows the PJ vs BER curve. Because the Q factor and the BER are linked by the inverse error function according to Equation (2-9), we can transfer the measured PJ vs. BER data into PJ vs. Q factor data. According to our jitter tolerance extrapolation algorithm that the relationship between the Q factor and the PJ is linear, we can do a Q factor linear fitting based on the PJ vs. Q factor data. The plot in the top left corner is a Q factor fitting result. Based on the fitting result, we can return to predict the PJ tolerance at low BER region through the error function.

In the above jitter tolerance extrapolation process, every step is straightforward except the Q factor linear fitting. The fitting is based on the jitter tolerance extrapolation algorithm that there is a linear relationship between the Q factor and PJ. The following explains how we derive our jitter tolerance extrapolation algorithm.

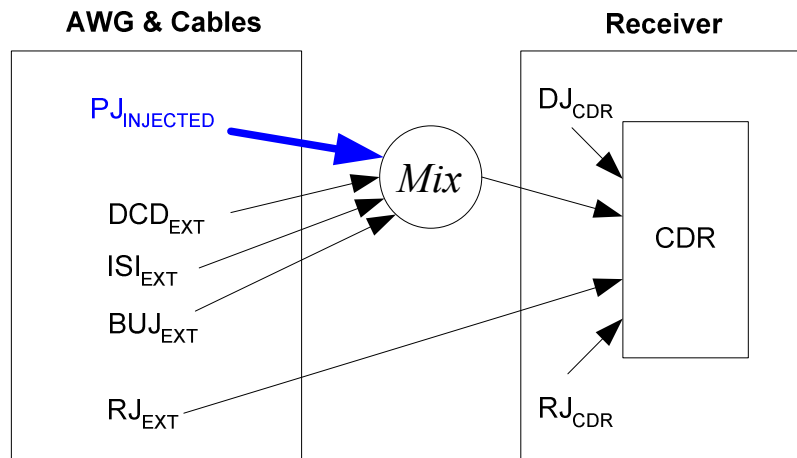


**Figure 3-23:** Jitter sources to the CDR

In our testing setup shown in Figure 3-6, we use an AWG to source the test signal and the AWG is connected to the receiver input through RF cables. The jitter sources that stress the CDR come from the AWG, connection cables and the CDR itself. Figure 3-23 illustrates these jitter sources. All the jitter components are convoluted together to affect the CDR performance. We use the following symbols to represent different jitter sources:

- $PJ_{INJECTED}$ : the PJ injected in the AWG signals
- $DCD_{EXT}$ : the DCD from the AWG and cables
- $ISI_{EXT}$ : the ISI from the AWG and cables
- $BUJ_{EXT}$ : the BUJ from the AWG and cables
- $RJ_{EXT}$ : the intrinsic RJ of the AWG
- $DJ_{CDR}$ : the intrinsic DJ of the device
- $RJ_{CDR}$ : the intrinsic RJ of the device

Under the “black box” assumption, we have no knowledge about the  $DJ_{CDR}$  and  $RJ_{CDR}$ . However, we can assume that  $DJ_{CDR}$  and  $RJ_{CDR}$  are constant for the same device with the same injected jitter frequency because they are determined by the CDR response to the jitter frequency. In [90], a method is proposed to measure the receiver internal jitter. We can also assume that the  $RJ_{EXT}$  is a constant when we sweep through different amounts of PJ at a fixed frequency. This is reasonable because the RJ in the AWG comes mostly from the sampling clock, which is constant when we change the programmed AWG data samples for PJ injection. It can also be proved by the jitter calibration result shown in Figure 3-17, where  $RJ_{EXT}$  is the constant offset between the measured DJ and the measured TJ. Considering  $RJ_{CDR}$  and  $RJ_{EXT}$  are independent, if we denote the total RJ seen by the CDR with  $RJ_{TOT}$ ,  $RJ_{TOT}$  is constant and we have:

$$RJ_{TOT} = \sqrt{RJ_{EXT} + RJ_{CDR}} \quad (3-1)$$

The  $DCD_{EXT}$ ,  $ISI_{EXT}$  and  $BUJ_{EXT}$  are assumed to be constant when the PJ is incremented. This is also a reasonable assumption, because they are mainly determined by the group delay caused by bandwidth limitation. It is also proved by the constant offset between the PJ and TJ shown in Figure 3-17. Of course, how the PJ combines with the ISI depends on the relative phase relationship, which is unknown inside the DUT. As all the DJ sources are uncorrelated, the total DJ seen by the CDR,  $DJ_{TOT}$ , can be expressed as:

$$DJ_{TOT} = (PJ_{INJECTED} + ISI_{EXT} + DCD_{EXT} + BUJ_{EXT}) + DJ_{CDR} \quad (3-2)$$

Under the Q factor model at the bathtub crossing point (filling up 1UI) discussed in Chapter 2.2.2, the RJ, DJ and UI are related by Equation (2-7):

$$UI = DJ + 2Q * RJ_{RMS}$$

where  $Q$  is  $Q(x)$  defined in Equation (2-1) with  $x = BER$  [69].

By plugging Equations (3-1) and (3-2) to Equation (2-7), we have

$$UI = PJ_{INJECTED} + DJ_{DELTA} + 2Q * RJ_{TOT} \quad (3-3)$$

where  $DJ_{DELTA}$  is a constant defined as

$$DJ_{DELTA} = ISI_{EXT} + DCD_{EXT} + BUJ_{EXT} + DJ_{CDR}$$

Rewriting Equation (3-3) to solve  $Q$  and  $PJ$ , we have

$$Q = C \times PJ_{INJECTED} + S \quad (3-4)$$

$$PJ_{INJECT} = \frac{Q - S}{C} \quad (3-5)$$

where  $C$  and  $S$  are constants defined by

$$C = -\frac{1}{2RJ_{TOT}} \quad (3-6)$$

$$S = \frac{UI - DJ_{DELTA}}{2RJ_{TOT}} \quad (3-7)$$

Equation (3-4) demonstrates that the  $Q$  factor is a linear function of the injected  $PJ$ . As discussed in Chapter 2.2.2, the  $Q$  factor and BER are related by the complementary error function and shown in Equations (2-8) and (2-9). By substituting Equation (3-4) into Equation (2-8), we have:

$$BER = 0.5 * erfc\left(\frac{C * PJ_{INJECTED} + S}{\sqrt{2}}\right) \quad (3-8)$$

Therefore, we linked BER to a single variable –  $PJ_{INJECTED}$  following the classical complementary error function –  $erfc$ . The curve fitting for this function has matured for decades when applied to transmitter bathtub curve fitting. Even though we cannot use bathtub curves to represent jitter tolerance extrapolation, the mathematics needed for conducting the jitter tolerance curve fit is still the complementary error function.



Equation (3-8) enables us to estimate BER according to the injected PJ in the test signal. We can extrapolate the PJ tolerance at low BER levels (such as  $10^{-12}$ ) once we know the two constant values  $C$  and  $S$ , which can be obtained using higher BER data (such as  $10^{-10}$  and higher).

### 3.4.2 Accelerating Jitter Tolerance Characterization

In design validation and device characterization, we need to get the TJ tolerance number at different PVT corners. The test signal calibration results shown in Chapter 3.2.3 enable us to translate the TJ tolerance testing into PJ tolerance testing. Our scheme is to perform a PJ tolerance BER scan using test signals with different levels of injected PJ. High BER data are collected in the range of  $10^{-6}$  to  $10^{-10}$ . Q factor values at different BER levels are calculated according to Equation (2-9). Theoretically, we only need two data points to get the two constant values  $C$  and  $S$  in Equation (3-4) according to

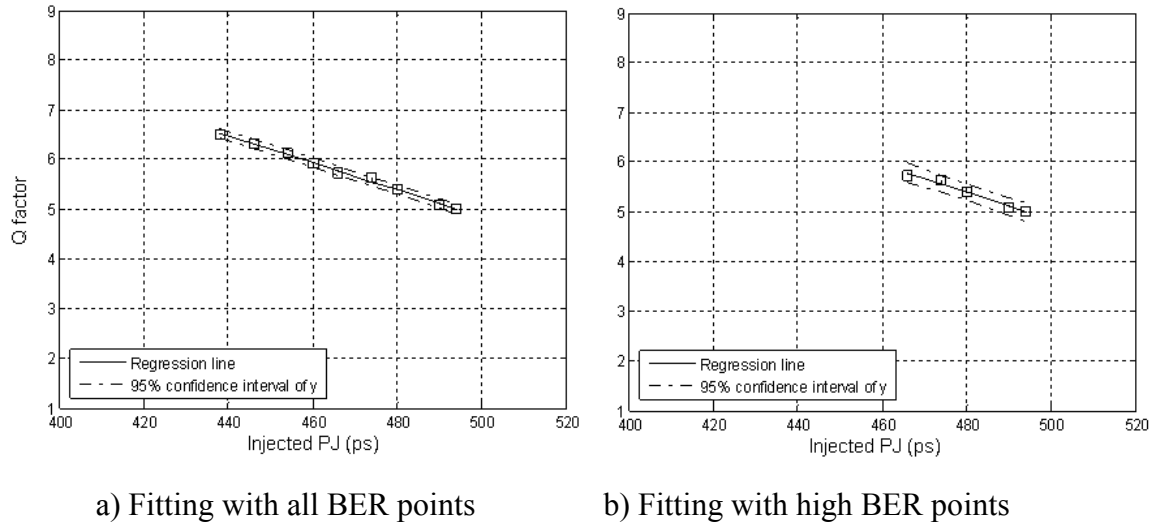
$$C = \frac{Q_1 - Q_2}{PJ_1 - PJ_2}$$

$$S = \frac{Q_2 * PJ_1 - Q_1 * PJ_2}{PJ_1 - PJ_2}$$

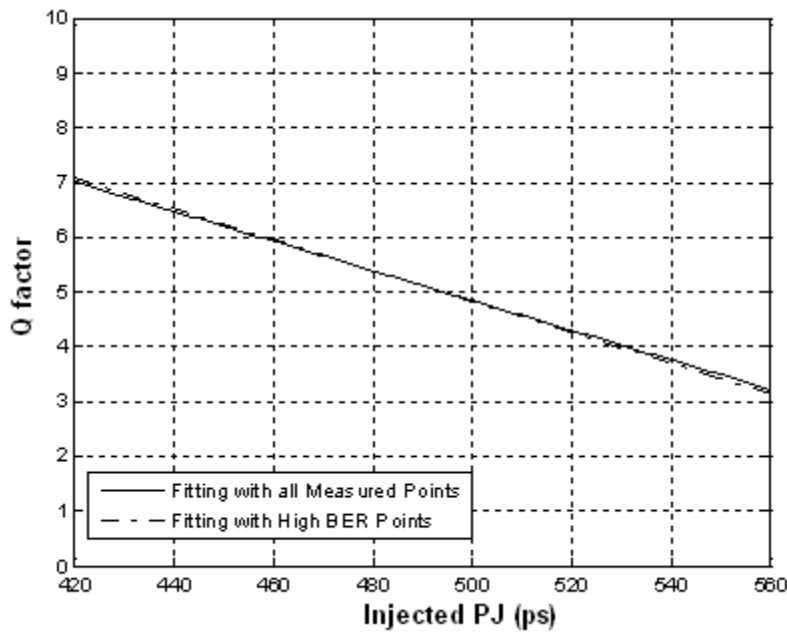
However, we need to catch a large number of errors when testing BER in order to get a high confidence result because of the randomness of the RJ. A better approach is to use more data points and perform linear regression fitting. In the example below, jitter tolerance BER scan was performed using 1.5Gbps test signals discussed in Chapter 3.2.2, and BER data was collected in the range of  $10^{-6}$  to  $10^{-11}$ . The data between  $10^{-6}$  to  $5 \times 10^{-9}$  was considered as high BER data and was used to predict the remainder of the points, which are considered as low BER points.

Figure 3-24 is a linear regression fitting of the Q factor versus injected PJ. Figure (a) is the fitting result based on all measured BER points collected between  $10^{-6}$  and  $10^{-11}$ , while Figure (b) is the fitting result based on high BER points only. The difference between the two fitting results is shown in Figure 3-25. The two fitting lines are almost

the same, which demonstrates that the prediction based on high BER points only is very accurate.



**Figure 3-24:** Linear regression of Q factor as a function of the injected PJ



**Figure 3-25:** A comparison between the two fitting results

Based on the Q factor fitting result, we can now plot the BER curve as a function of the injected PJ, and thus predict the jitter tolerance for a lower BER, e.g.  $10^{-12}$ . Figure 3-26

shows the difference between the BER curve predicted based on the high BER points and the curve fitted with all measured BER points. The discrepancy is found to be very small; from Figure 3-26, we read only 2ps difference at  $10^{-12}$  BER. In this plot, diamond points (high BER data) are used for the prediction; star points are additional real measurements at the lower BER region. The real measurements in the lower BER range (star points) are very close to the predicted curve, which indicates that our BER prediction can successfully match the measurements.

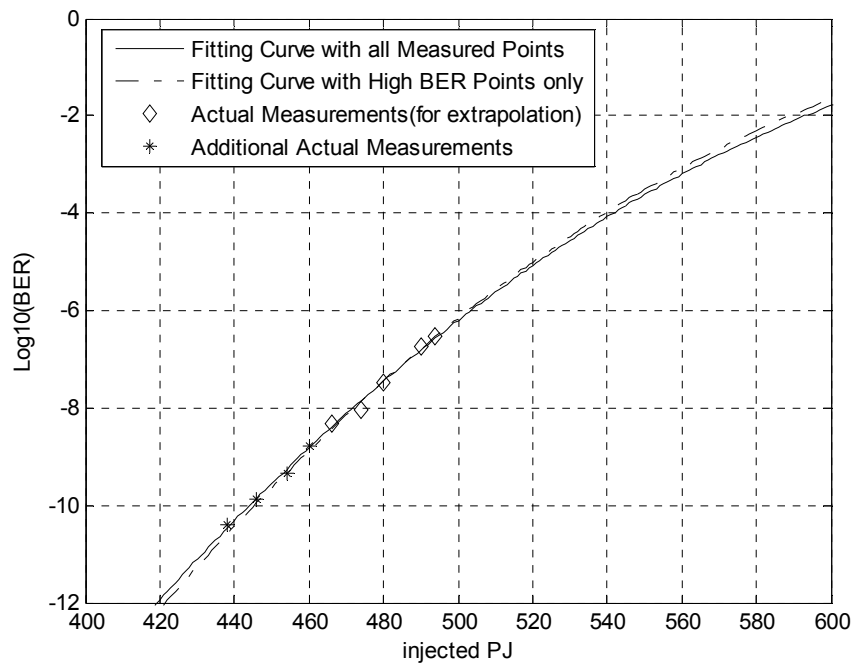
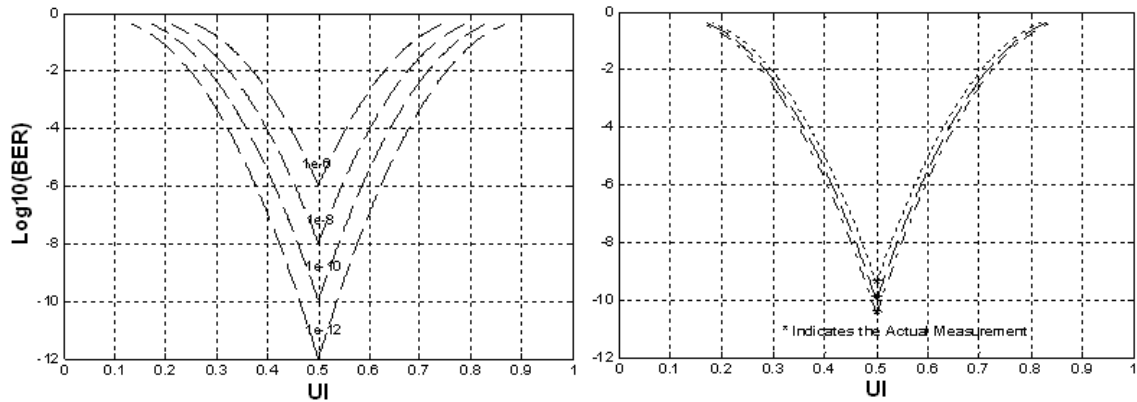


**Figure 3-26:** A comparison of BER curve fitting results

The jitter tolerance result presented in Figure 3-26 is in terms of PJ only. To include the DCD, ISI, BUJ and RJ, we need to link this diagram with jitter injection calibration curves from the Wavecrest SIA-3000. As shown in Figure 3-17, the delta between the injected PJ and the actual TJ observed by the SIA-3000 is a constant around 92ps. For this particular device under test, the jitter (TJ) tolerance at  $10^{-12}$  BER is 512ps or 0.76UI, while 420ps of PJ is injected in the test signal.

Figure 3-27 can further help understand the story from the bathtub point of view. Figure (a) conceptually shows that the depth of the bathtub curve moves with different amounts

of injected jitter; Figure (b) is a comparison of the predicted bathtub curves to real measurements. This is another way to visualize the accuracy of our model.



a) Predicted bathtub curves

b) Predicted curves vs. actual measurements

**Figure 3-27:** Bathtub curve prediction

We further verified our jitter tolerance extrapolation algorithm at 3Gbps applications and measured the BER down to  $10^{-12}$ . For 3Gbps applications, the test signals need to be re-generated and calibrated using the methods discussed in Chapter 3.2.2. Figure 3-28 shows the calibration results of the generated 3Gbps test signals using a Wavecrest SIA-3000; it plots the measured PJ and TJ values at different injected PJ levels on one tester. As can be seen, from 20ps to 200ps, the measured PJ correlates well to the injected PJ and there is a constant offset between the measured PJ and the measured TJ. In this case, the offset is around 80ps. When the injected PJ is below 20ps, the TJ does not change much due to the noise floor of the AWG. This does not impact us as we will show later that the test signals we need should have PJ values more than 100ps.

Once again, the constant offset between the injected PJ and the measured TJ is caused by the intrinsic RJ of the AWG, and DCD, ISI and BUJ from the AWG and cables. The offset enables us to relate the PJ to TJ, and we can translate the TJ compliance testing into PJ testing, where we can control the amount of PJ in the test signal.

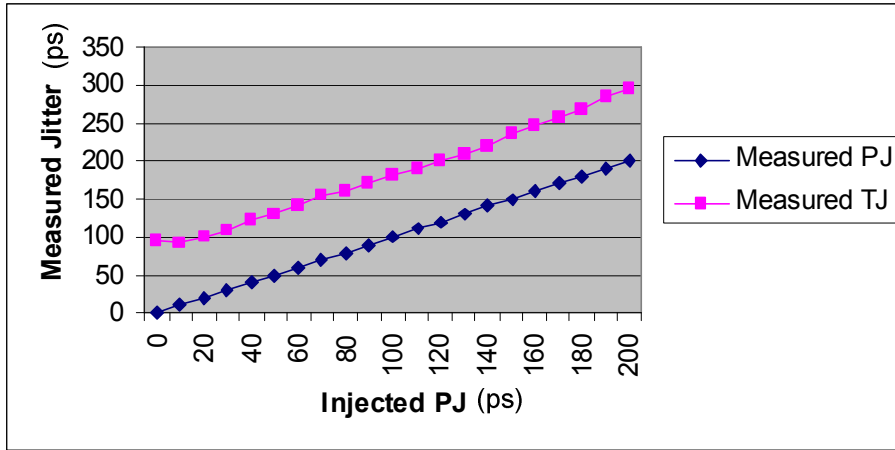


**Figure 3-28:** 3Gbps test signal calibration results

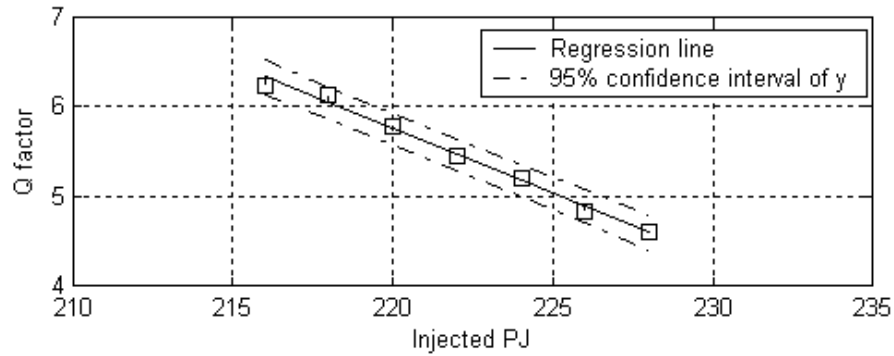
Table 3-1 lists an example of measured BER values at different PJ levels using the 3Gbps test signals; the Q factor values are calculated based on the BER value according to Equation 2-9. When we sweep the injected PJ from 228ps to 216ps, the BER levels decrease from  $10^{-6}$  to  $10^{-10}$ . In this experiment, the bit errors are obtained using the DFT-based error detection approach discussed in Chapter 3.3.2. We use these measured high BER data to extrapolate the BER performance at lower BER levels and then verify the extrapolation results by making BER measurements down to  $10^{-12}$  BER.

**Table 3-1:** High BER Data for Jitter Tolerance Extrapolation

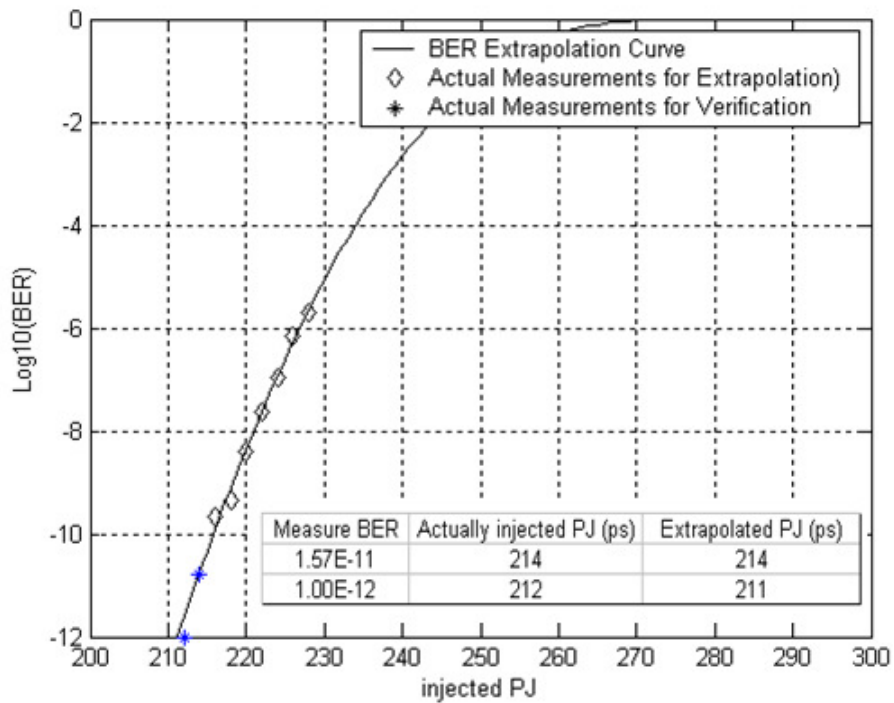
PJ(ps)	216	218	220	222	224	226	228
BER	2.13E-10	4.37E-10	3.90E-9	2.43E-8	1.05E-7	7.06E-7	2.05E-6
Q	6.24	6.13	5.77	5.46	5.19	4.82	4.60

Figure 3-29 is a linear regression fitting of the Q factor versus PJ based on the measurement results shown in Table 3-1. Based on the Q factor fitting result, we can now plot the BER curve as a function of the injected PJ according to Equation (2-8), and thus predict the jitter tolerance at low BER levels. Figure 3-30 shows the BER curve based on the fitting result from the measurements listed in Table 3-1 (diamonds). It also shows low BER measurements for extrapolation accuracy verification (star points). As we can see, at  $10^{-12}$  BER there is only 1ps discrepancy between the actually measured PJ tolerance

and the extrapolated PJ tolerance based on the BER data above  $10^{-10}$ . We tried the procedure on different devices and the discrepancy is within 2% while our solution can speed up the characterization over 1000 times.



**Figure 3-29: Q factor vs. PJ**



**Figure 3-30: BER extrapolation**

The jitter tolerance result presented in Figure 3-30 is in terms of PJ. To translate the PJ tolerance into TJ tolerance, we need to use the jitter injection calibration curves shown in

Figure 3-28, where the delta between the injected PJ and the actual TJ observed by the SIA-3000 is a constant around 80ps. For this particular device with BER data listed in Table 3-1, the TJ tolerance at  $10^{-12}$  BER is 292ps or 0.88UI while PJ is 212ps.

### 3.4.3 Accelerating Jitter Tolerance Compliance Testing

If we directly apply the jitter tolerance characterization technique in production to qualify jitter tolerance compliance, the test time overhead is still a bit high because it involves BER to Q factor translation, Q factor fitting and BER extrapolation down to  $10^{-12}$  level. It takes around one second, which is still too long for one parameter testing – on average an SoC device may have hundreds of parameters to test.

Considering the compliance testing in production is only a go/no-go judgment process, we do not need to know the exact value of the jitter tolerance for each device; we only need to know whether the jitter tolerance of a device is better than the jitter specification defined at  $10^{-12}$  BER. Instead of extrapolating the jitter tolerance down to  $10^{-12}$  BER and comparing it with the specification, we perform the jitter tolerance compliance test at a higher BER level. For example, we can do the test by qualifying  $10^{-6}$  BER performance. We apply a test signal with a certain amount of injected PJ to the device: if the measured BER of the device is better than  $10^{-6}$ , it passes; otherwise, it fails. For this approach, we need to solve two issues:

- Translating the jitter tolerance specification from  $10^{-12}$  BER level to  $10^{-6}$  BER level
- Translating the TJ specification to a PJ specification

The proposed jitter tolerance extrapolation algorithm can transfer jitter tolerance specifications at different BER levels. Because the Q factor values at  $10^{-12}$  and  $10^{-6}$  BER levels are known (7.0374 and 4.7534 respectively [38]), according to Equation (3-5), the PJ tolerance difference between  $10^{-12}$  and  $10^{-6}$  BER levels can be calculated by

$$PJ_{10^{-12}-10^{-6}} = \frac{Q(10^{-12}) - Q(10^{-6})}{C} \quad (3-9)$$

which is 25ps in the 3Gbps example in Chapter 3.4.2. According to Equation (3-1) and Equation (3-6), the difference is determined by the RJ in the test signal and the intrinsic RJ of the device that slightly varies from device to device. For each new design, we need to perform the jitter tolerance extrapolation to characterize the PJ difference distribution and use the worst case value (the minimum value) to set test limits for production.

Next, we need to translate the TJ specification into PJ specification because we can only control the amount of PJ in the test signal. The test limit we need to set in production should be based on the amount of the injected PJ. This translation is done according to the offset value between the measured TJ and the injected PJ as shown in Figure 3-17 and Figure 3-28. To do this translation for production, we need to perform the test signal calibration at all the testers because the offset may vary from tester to tester. Figure 3-31 shows the offset at some testers. For these testers, we can claim that the offset between the injected PJ and the actual TJ is at least 70ps.

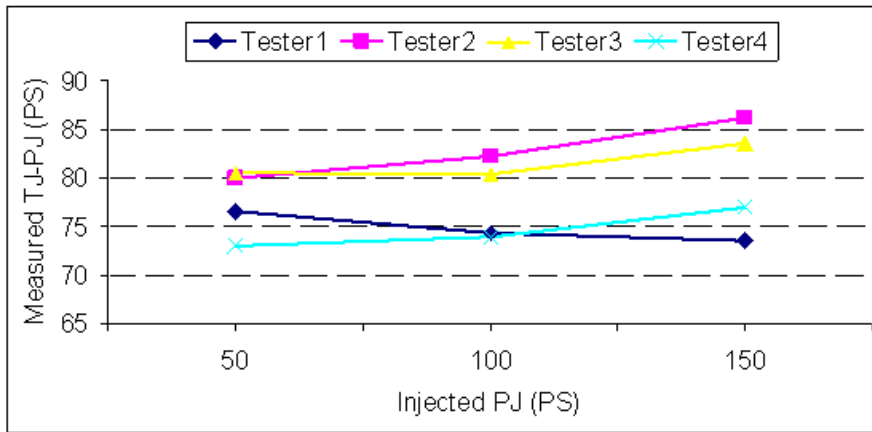


**Figure 3-31:** The offset between PJ and TJ at different testers

Based on this offset, we can translate the TJ specification into a PJ tolerance requirement. In SATA II, the out-of-band TJ tolerance specification is 200ps at  $10^{-12}$  BER level [22]. We can guarantee the TJ specification by checking the PJ tolerance at 130ps: if a device can tolerate 130ps PJ at  $10^{-12}$  BER level, we can guarantee that the device meets the SATA jitter tolerance specification. Even though this might slightly overstress devices on



some testers (such as Tester2 and Tester3), this is acceptable as long as it does not cause yield issues.

According to jitter translation Equation 3-9, the PJ difference between  $10^{-12}$  and  $10^{-6}$  BER levels is 25ps. Because the PJ tolerance requirement at  $10^{-12}$  BER level is 130ps, the PJ tolerance limit should be set to 155ps at  $10^{-6}$  BER level. We can source a test signal with 155ps injected PJ to the receiver and check  $10^7$  bits of recovered data. If no errors are detected, this device is classified as a good one; otherwise, it fails the jitter tolerance compliance test.

### **3.4.4 Discussions**

In the proposed acceleration scheme for jitter tolerance qualification, the injected jitter calibration and the jitter tolerance extrapolation are the two key techniques we employ. When applying the scheme to production testing, we need to especially pay attention to them.

We need to calibrate the test signals on all testers to ensure that the difference between the injected PJ and the measured TJ is bigger than the offset we used to derive the test limit, which is 70ps in the 3Gbps example. If the offset is below this, we need to tighten our test limit accordingly. In the same time, we also need to keep an eye on the possible yield loss because we overstress devices on some testers, such as on Tester2 in Figure 3-31 where we overstress the device by around 10ps. This should not cause issues because the design margin normally is big enough to accommodate it. Another source that provides extra margin for the test is that we classify devices with errors between 1 and 10 out of  $10^7$  bits as bad devices. Actually, they can be classified as good ones as they meet  $10^{-6}$  BER performance, but with limited confidence. Because of the extra margin, we have a high confidence level that the good devices meet the jitter tolerance requirement.

In addition, we need to do the jitter specification translation (from  $10^{-12}$  to  $10^{-6}$  BER levels) based on devices that can cover the product to be tested, such as devices from all

process corners. Doing this from one device may not be enough. The good thing is that we only need to do this once for every new design.

Even though the experiment is conducted on Teradyne AWG6000, the jitter tolerance extrapolation technique is generic and can be used on any platform that has jitter injection capability and that can perform BER testing. The technique can rapidly report the actual jitter tolerance value or qualify a jitter tolerance specification.

---

# Chapter 4 – Transmitter Jitter Extraction on ATE

---

## 4.1 Introduction

Transmitter jitter testing has been investigated for years. There are quite a few bench instruments that can make the jitter measurements accurately [91], [92]. There are also some ATE platforms that have transmitter jitter testing capability. However, these solutions have limitations: either their throughput is too low or their accuracy needs to be improved. In addition, almost each existing solution has its own propriety algorithms or patents [93].

To overcome these limitations, we research the transmitter jitter testing on ATE and present a systematic solution for multiple Gbps transmitter jitter characterization and production testing. Our under-sampling based approach can extract jitter either from edge histograms in time domain or from the jitter spectrum in frequency domain. The two approaches can also be combined to achieve more accurate test results.

### 4.1.1 Transmitter Jitter Testing Overview

As discussed in Chapter 2.2.1, most HSSI standards, such as SATA and Fiber Channel, define DJ and TJ specifications separately. Table 4-1 lists the transmitter out-of-band jitter specifications for the SATA II [22]. The TJ of the SATA transmitter should not exceed 0.37UI at  $10^{-12}$  BER level and DJ should not exceed 0.19UI. Though the SATA specification does not specify the RJ limit, we can get the limit by assuming that all TJ is

contributed by RJ. The RJ with 0.37UI peak-to-peak value at  $10^{-12}$  BER level translates into a RJ RMS value of 0.026UI, or 8.8ps at 3Gbps data rate and 4.4ps at 6Gbps data rate. The RJ RMS value is usually used to estimate TJ at  $10^{-12}$  BER level, as it is impossible to directly measure TJ at this BER level in volume production due to long test time – it takes tens of minutes even at 6Gbps data rate.

**Table 4-1:** Transmitter Jitter Specifications for SATA Gen2

TJ	DJ	RJ (RMS)*
0.37UI	0.19UI	0.026UI or 8.8ps@3G, 4.4ps at 6G

\*Deduced from the TJ specification

To economically apply the above test limits in production, we need the jitter test to have the capabilities of:

- Separating jitter components
- Achieving accuracy in sub-picoseconds
- Having the test done in milliseconds

Unfortunately, there is currently no solution on ATE that meets these criteria, even though the jitter measurement and decomposition have been investigated for years [94], [95]. Popular jitter testing solutions include Bit Error Rate Testers (BERT), histogram-based Oscilloscopes, and Time Interval Analyzers (TIA) [34]. These solutions are commonly used for design validation and characterization on bench. However, we cannot directly apply them for at-speed testing in production because of the low throughput.

There are not many systems right now that can do multi-gigabit devices jitter compliance testing in production. Many jitter test solutions are based on extra on-chip circuitry, or add-on modules [40], [41], [96], [97], [98], [99]. The applications of these solutions are limited either by their low throughput, low accuracy, or high design complexity of the device or the loadboard. Because of these limitations, pure ATE-based solutions are preferred in production because of their high portability and high throughput. One approach is to utilize multi-gigabit signal generators and digitizers. The generator and

digitizers are becoming available as fully-integrated ATE instruments. One example is the GigaDig on Catalyst/Tiger ATE from Teradyne [84]. The GigaDig is a digitizer, capable of capturing analog signals with a time resolution better than 1ps. With this kind of instruments, it has become feasible to perform multi-gigabit devices jitter test on ATE [2], [86], even though systematic jitter extraction algorithms on ATE have not matured.

In [100], a transmitter jitter test solution is proposed based on the high-speed digital pins of the Agilent's 93000 ATE. By shifting the compare strobes in the timing axis and level threshold axis, this approach first builds a bathtub curve, and then applies the jitter separation algorithm. However, the test economy of this solution needs to be improved: it takes near 1 second even with 2ps resolution. As jitter is just one of hundreds parameters to be tested on an average device, one second spent for one test is still too long on the ATE environment. In addition, the accuracy also needs to be improved: RJ is close to 1ps higher than the bench result. In [86], an SATA test solution on ATE is presented, which includes transmitter jitter testing. However, the transmitter jitter testing scheme in [86] is not very accurate; it reports higher RJ (1~2 ps) and higher TJ (20ps) than the bench equipment does. In addition, the test parameters in this solution can still be further optimized to achieve better test economy.

#### **4.1.2 Proposed Solution**

In this chapter, we present a new transmitter jitter testing solution based on a high-bandwidth digitizer on ATE [2]. We sensibly make the test setup and develop jitter extraction procedures suitable for running the test fast and accurately. With the current ATE instrument, we achieve sub-picosecond jitter accuracy and can finish the whole transmitter testing in 100ms, which no one else has ever achieved in an ATE environment to our best knowledge. The whole solution has been verified at data rates up to 6Gbps applications. Better performance and higher data rate applications are attainable using our solution with the advances in ATE instruments in the future – they are only limited by the bandwidth and timing resolution of the digitizer. The accuracy of the proposed

solution is verified by both bench equipment and ATE itself, and the test has already been applied in volume production.

In the remainder of the chapter, we first describe the principles of setting instruments and test parameters for data acquisition. Then we present the details of the data processing – how jitter is extracted and decomposed in both the time domain and the frequency domain. After that, the experimental results are presented and limitations are discussed.

## 4.2. Test Setup for Data Acquisition

The digitizer we use for the transmitter testing is GigaDig. The GigaDig is a fully integrated ATE digitizing instrument with a typical under-sampling bandwidth over 9 GHz [84]. Its input voltage range is 64mv to 1.024v, capable of covering most HSSI standards. This chapter concentrates on the SATA transmitter, which has an output range of 400mv~700mv. With a 1 Mega sample memory and 12-bit digitizing resolution, the GigaDig can perform all transmitter function and parameter tests with a single capture of the transmitter output. The following discusses how we sensibly set up the GigaDig for data acquisition.

### 4.2.1 Overview of the Test Setup

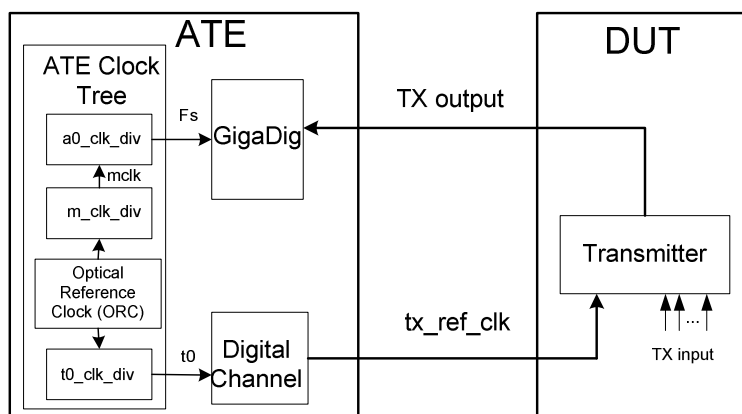


**Figure 4-1:** Transmitter test setup for data acquisition

The test setup is shown in Figure 4-1. The ATE provides a reference clock signal  $tx\_ref\_clk$  to the transmitter; a PLL in the transmitter then locks the transmitter output rate to the reference clock. In our applications, the ideal  $tx\_ref\_clk$  is around 30MHz and the transmitter output data rate  $F_{data}$  can be 1.5G, 3G or 6Gbps. The GigaDig captures the transmitter output with an under-sampling rate  $F_s$  between 5 Mega Samples per second (MS/s) to 10 MS/s.

The under-sampling technique has been used in high-speed testing for years [94]. This technique first captures the output signal of the DUT at a sampling rate  $F_s$  that is lower than the output data rate  $F_{data}$ , and then shuffles the captured samples in a predetermined manner. The shuffled output is a sequence of samples that would have resulted from sampling at a much higher frequency - effective sampling rate  $F_{eff}$  defined by

$$F_{eff} = F_{data} * N_{SPB} \quad (4-1)$$

where  $N_{SPB}$  is the Number of Samples Per Bit (SPB) in the shuffled data.

#### 4.2.2 Principles of Clock Settings

Although the under-sampling principle is simple, the challenge for transmitter jitter testing is to properly set test parameters for data acquisition and to extract jitter information from captured samples. To capture within reasonable test time the transmitter output waveform with an adequate resolution for jitter decomposition, we need to properly set these parameters:

- o Test pattern length  $L_{pattern}$
- o Effective sampling rate  $F_{eff}$
- o Undersampling rate  $F_s$

In order to set the clock properly to capture the transmitter output in an under-sampling environment, we need to first determine the test pattern. To provide adequate test coverage, the test pattern length  $L_{pattern}$  should be at least 20 bits because the width of the parallel data to the transmitter input is 20. On the other hand, the length should be as short as possible in order to save test time and also simplify the data processing. For these

reasons, we choose a 20-bit test pattern 000001111101010011. This pattern includes both high density and low density transitions, with a total of eight edges. The transmitter output (GigaDig input) fundamental frequency  $F_{DUT}$  is defined by

$$F_{DUT} = \frac{F_{data}}{L_{pattern}} \quad (4-2)$$

which generates a 150MHz  $F_{DUT}$  when the data rate  $F_{data}$  is 3GHz and the pattern length is 20.

Our experimental data in Chapter 4.4.3 also demonstrates that the 20-bit test pattern is a very good choice for transmitter jitter testing. It generates similar RJ and DJ compared to a 128-bit PRBS pattern and a clock pattern. The 20-bit pattern provides reasonably good coverage in a production environment.

The required effective sampling rate  $F_{eff}$  is determined by the target test accuracy. To achieve a jitter measurement resolution better than 1ps, we need to have the effective sampling resolution better than 1ps, which corresponds to an effective sampling rate higher than 1000GHz. For 3Gbps data signals, this translates into capturing at least 333 samples per data bit. To leave some margin and also keep the test time short, we choose to capture 400 samples per bit, which gives

$$N_{SPB}=400$$

$$F_{eff}=1200G$$

The under-sampling rate  $F_s$  needs to be calculated based on the GigaDig input fundamental frequency  $F_{DUT}$  and the effective sampling rate  $F_{eff}$ . In order to capture samples coherent with the input signal, we need to satisfy the equation

$$\frac{1}{F_s} = K \frac{1}{F_{DUT}} + \frac{1}{F_{eff}} \quad (4-3)$$

where  $K$  is the number of cycles of  $F_{DUT}$  slipped before the next sample.

According to Equations (4-1) and (4-2), Equation (4-3) can be expressed as



$$\frac{1}{F_s} = \frac{1}{F_{data}} (K * L_{pattern} + \frac{1}{N_{SPB}}) \quad (4-4)$$

As shown in Figure 4-1, ATE provides to the transmitter a reference clock  $tx\_ref\_clk$  with a frequency  $F_{tx\_ref\_clk}$ . The PLL in the transmitter sets the transmitter output data rate by multiplying the reference clock by an integer  $M_{d2ref}$ . Therefore, we have

$$F_{data} = F_{tx\_ref\_clk} * M_{d2ref} \quad (4-5)$$

where  $M_{d2ref}$  is 100 for 3Gbps applications and 200 for 6Gbps applications while  $F_{tx\_ref\_clk}$  is around 30MHz. If the reference clock is exactly 30MHz, the transmitter output rate  $F_{data}$  would be exactly 3GHz. However, the ATE cannot source a clock signal exactly at 30MHz because this clock is derived from the Optical Reference Clock (ORC) divided by  $t0\_clk\_div$ , where ORC is around 50,000THz and  $t0\_clk\_div$  can only be an integer. Similarly,  $F_s$  is also derived by dividing the ORC. According to Figure 4-1, we have

$$F_{tx\_ref\_clk} = \frac{ORC}{t0\_clk\_div} \quad (4-6)$$

$$F_s = \frac{ORC}{m\_clk\_div * a0\_clk\_div} \quad (4-7)$$

Based on Equations (4-5), (4-6), and (4-7), we can rewrite Equation (4-4) to

$$\frac{m\_clk\_div * a0\_clk\_div}{ORC} = \frac{t0\_clk\_div}{ORC * M_{d2ref}} (K * L_{pattern} + \frac{1}{N_{SPB}}) \quad (4-8)$$

By re-organizing Equation (4-8), we can get

$$\frac{t0\_clk\_div}{m\_clk\_div} = \frac{a0\_clk\_div * M_{d2ref} * N_{SPB}}{K * L_{pattern} * N_{SPB} + 1} \quad (4-9)$$

Equation (4-9) is the one that we use to determine the values of all the clock dividers ( $t0\_clk\_div$ ,  $a0\_clk\_div$  and  $m\_clk\_div$ ) in order to capture the transmitter output with the expected resolution. Equation (4-9) applies to all data rates and test patterns. However, if

the data rate and/or reference clock is different,  $M_{d2ref}$  needs to be adjusted accordingly; if the length of the test pattern is different,  $L_{pattern}$  is different.

### 4.2.3 Test Setting Parameter Calculations

Equation (4-9) provides the principle of setting the clock dividers. As an example, we first demonstrate how the clock dividers are set in a 3Gbps application using the 20-bit test pattern. The test setup of the application is shown in Figure 4-1. The reference clock  $rx\_ref\_clk$  needs to be around 30MHz; the intended effective sampling rate  $F_{eff}$  is 1200GHz; the ATE requires that  $mclk$  needs to be between 160MHz to 200MHz and the under-sampling clock  $F_s$  needs to be between 5MHz and 10MHz [84].

If we want  $F_s$  to be around 7.5MHz, once choice is to set  $a0\_clk\_div$  to be 26 and  $mclk$  to be around 195MHz. By replacing  $M_{d2ref}$  with 100,  $N_{SPB}$  with 400 and  $L_{pattern}$  with 20 for the 3Gbps application, we can simplify Equation (4-9) to

$$\frac{t0\_clk\_div}{m\_clk\_div} = \frac{1040000}{8000 * K + 1} \quad (4-10)$$

Basically, Equation (4-10) is a transformation of Equation (4-3) with pre-set parameters based on the application. We can guarantee the coherent sampling by satisfying Equation (4-10). Our next goal is to get the  $K$  value in Equation (4-10). Considering the  $tx\_ref\_clk$  should be around 30MHz and  $mclk$  is expected to be around 195MHz, we can get the rough values of the  $t0\_clk\_div$  and  $m\_clk\_div$ :

$$t0\_clk\_div\_rough = \frac{ORC}{30MHz} \approx 16666666666$$

$$m\_clk\_div\_rough = \frac{ORC}{195MHz} \approx 256410256$$

Therefore, we have

$$\frac{t0\_clk\_div}{m\_clk\_div} \approx \frac{t0\_clk\_div\_rough}{m\_clk\_div\_rough} \approx 6.5 \quad (4-11)$$

According to Equations (4-11) and (4-10), we can solve  $K$  in Equation (4-10) and  $K=20$  gives the best approximation for the expected  $mclk$  and  $tx\_ref\_clk$  frequencies. When  $K=20$ , Equation (4-10) becomes

$$\frac{t0\_clk\_div}{m\_clk\_div} = \frac{1040000}{160001} \quad (4-12)$$

Because  $t0\_clk\_div$  and  $m\_clk\_div$  need to be integers and  $t0\_clk\_div$  should be around 166666666, we can choose

$$t0\_clk\_div = 1040000 * 1602 = 1666080000 \quad (4-13)$$

$$m\_clk\_div = 160001 * 1602 = 256321602 \quad (4-14)$$

Where 1602 is floor of the ratio between  $t0\_clk\_div\_rough$  and 1040000 ( $1666666666/1040000 \approx 1602.564$ ).

Using the clock divider values shown in Equation (4-13) and (4-14) and the  $a0\_clk\_div$  value (pre-set to 26), we can generate the clocks that enable us to capture the 3Gbps signal with 400 samples per bit. Table 4-2 is a summary of the parameters used for the 3Gbps data capture. Table 4-3 lists the actual under-sampling frequency and the transmitter reference clock frequency.

**Table 4-2:** Parameter Settings for 20-bit Pattern 3Gbps Data Capture

Parameter	Description	Value
$F_{data}$	Transmitter output data rate	3GHz
$L_{pattern}$	Length of the data pattern	20
$M_{d2ref}$	Transmitter PLL multiplier	100 (30MHz ref clock)
$F_{DUT}$	Fundamental frequency of Tx output	150MHz
$N_{SPB}$	Number of samples per bit	400
$F_{eff}$	Effective sampling rate	1200GHz
$a0\_clk\_div$	$a0$ clock divider	26
$t0\_clk\_div$	$t0$ clock divider	1666080000
$m\_clk\_div$	$mclk$ divider	256321602

Actually, the above derived clock divider values are just one combination of the possible settings that can be used to capture waveforms with the expected resolution. According to the same procedure, we can get different clock divider settings if we pre-set  $F_s$  and  $mclk$  to different frequencies as long as the derived clocks are in their valid ranges. According to the parameter setting principle and the procedure demonstrated in the 3Gbps example, we can set the parameters for other applications. Table 4-4 lists the parameters for 6Gbps applications using a 20-bit test pattern. Table 4-5 lists the parameters for 5.5Gbps applications using a 20-bit test pattern and a 27.5MHz reference clock.

**Table 4-3:** Actual Clock Frequencies for the 3Gbps Data Application

Parameter	Description	Value
$F_s$	Undersampling clock frequency	$\approx 7.502594\text{MHz}$
$F_{tx\_ref\_clk}$	Tx reference clock frequency	$\approx 30.010564\text{MHz}$
$F_{mclk}$	mclk frequency	$\approx 195.067445\text{MHz}$

**Table 4-4:** Parameter Settings for 6Gbps Data Capture

Parameter	Description	Value
$F_{data}$	Tx output data rate	6GHz
$L_{pattern}$	Length of the data pattern	20
$M_{d2ref}$	Tx PLL multiplier	200 (30MHz ref clock)
$F_{DUT}$	Fundamental frequency of Tx output	300MHz
$N_{SPB}$	Number of samples per bit	400
$F_{eff}$	Effective sampling rate	2400GHz
$a0\_clk\_div$	a0 clock divider	26
$t0\_clk\_div$	t0 clock divider	1666080000
$m\_clk\_div$	mclk divider	256320801

The following is a few highlights of parameters that need to be changed for some other applications:

- If  $F_{data}=5.5\text{GHz}$  and the test pattern is 20 bits in length,  $F_{DUT}$  is 275MHz
- If  $F_{data}=3\text{GHz}$  and the test pattern is 128 bits in length,  $F_{DUT}$  is 23.4375MHz
- If the expected reference clock is different,  $t0\_clk\_div\_rough$  is different

**Table 4-5:** Parameter Settings for 5.5Gpbs Data Capture

Parameter	Description	Value
$F_{data}$	Tx output data rate	5.5GHz
$L_{pattern}$	Length of the data pattern	20
$M_{d2ref}$	Tx PLL multiplier	200 (27.5MHz ref clock)
$F_{DUT}$	Fundamental frequency of Tx output	275MHz
$N_{SPB}$	Number of samples per bit	400
$F_{eff}$	Effective sampling rate	2200GHz
a0_clk_div	a0 clock divider	26
t0_clk_div	t0 clock divider	1817920000
m_clk_div	mclk divider	279680874

The last test setup parameter we need to choose is the required number of samples  $N_{total}$ . The required number of samples can be derived from the pattern length and the effective sampling rate. To build edge transition histograms and to acquire their statistical properties for jitter extraction, we need to capture a certain number of cycles of the test pattern. For a statistics process, the Standard Error of the mean  $SE_m$  is defined by

$$SE_m = \frac{\delta}{\sqrt{n}} \quad (4-15)$$

where  $\delta$  is the standard deviation of the population and  $n$  is the size of the samples [101] [102].

From the statistical confidence point of view, the larger the sample size is, the less likely the error is. On the other hand, we need to minimize the number of samples in an ATE environment in order to minimize the test cost. To play a tradeoff, we choose to capture 20 cycles of the 20-bit test pattern. As we will discuss later, we use all the transition edges to calculate the RJ. There are total 160 edges in 20 cycles of the 20-bit test pattern. Therefore, the statistics error of the RJ is less than 8% according to Equation (4-15). This is an acceptable margin for our test.

Another factor that we need to consider when determining the total number of samples is the Fast Fourier Transformation (FFT) requirement. We will need FFT later for jitter

decomposition in the frequency domain. Twenty cycles of the 20-bit pattern with 400 samples per bit translate into 160k samples in total. The derived number of samples satisfies the FFT requirement.

### 4.3. Jitter Extraction

Jitter is extracted from the transmitter output waveform captured with the test setup and the parameters discussed in Chapter 4.2. Figure 4-2 is an example of the captured waveform of a 3Gbps signal. The waveform consists of 20 cycles of the 20-bit test pattern, with 400 samples in each data bit and 160,000 samples in total. This capture is used to perform transmitter functional and parameter testing. The thesis focuses on jitter extraction. Other measurements, such as transmitter function, rise/fall time and amplitude, are straightforward to perform once we capture the waveform, and their test time is very short compared to the jitter testing.

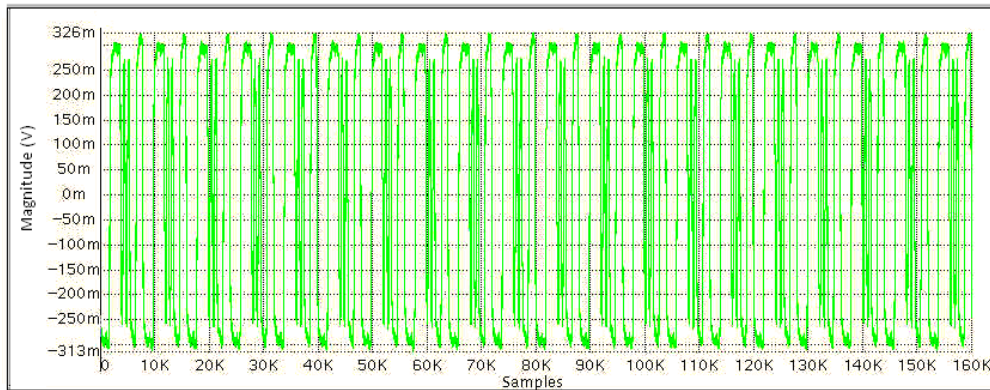


**Figure 4-2:** Captured transmitter output signal

#### 4.3.1 Generating Edge Displacement

Basically, jitter is the edge displacement of the actual edge transition position compared to its ideal position. In our test setup as shown in Figure 4-1, the reference clock *TX\_ref\_clk* determines the data rate of the transmitter. The transmitter ideal edge positions can be calculated by assuming that all the data bits are transmitted without any

jitter. The actual position of each edge transition might deviate from its ideal position due to jitter. Figure 4-3 shows an example of two edge transitions ( $L$  to  $H$  and  $H$  to  $L$ ) captured using the digitizer. As the edge transitions are not smooth, we use a curve fitting technique to extract actual zero crossing positions [103].

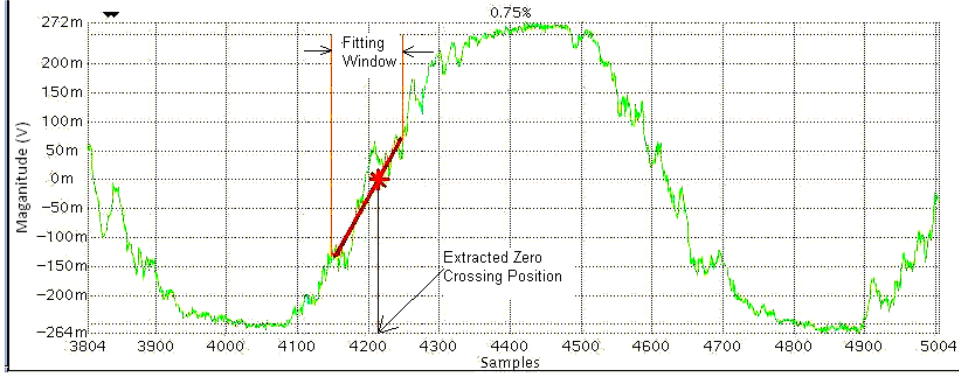


**Figure 4-3:** Actual edge transitions and curve fitting

The curve fitting is done in a window centered in the edge transition period. According to the SATA specification [22], the transmitter rise/fall time (20% - 80%) of 3Gbps signals is between 0.2UI (67ps) and 0.41UI(136ps). When the effective sampling resolution is 400 samples per bit, the number of samples during an edge transition (20% - 80%) period is between 80 and 164. Therefore, we choose a window with 80 samples to perform the curve fitting as shown in Figure 4-3. The first captured zero crossing sample in a transition edge determines the centre of the window that we choose for the curve fitting.

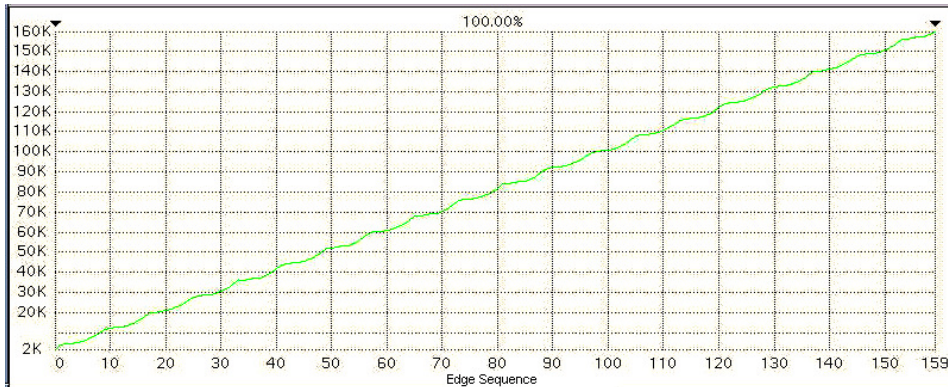


**Figure 4-4:** Derived edge positions from curve fitting

Figure 4-4 plots all the edge transition positions calculated from our curve fitting technique. The  $x$ -axis denotes the edge sequence, which has 160 edges in the captured 400 data bits. The edge position in  $y$ -axis is denoted by the number of samples relative to the first edge.

The edge displacement is obtained from the derived edge position minus the ideal edge position. The ideal position is calculated based on the ideal data rate of the transmitter and the first derived edge position. In this way, we extract 160 samples of the edge displacement data from the 160 derived edge positions. To perform FFT for the jitter spectrum analysis, we need edge displacement information for every data bit. In our implementation, we assume that no jitter is introduced in the data bits where no data transitions occur between two or more bits, so we just insert the edge displacement data from the previous edge transition to interpolate no-transition data bits. We will later eliminate the effect that the interpolation may cause. Figure 4-5 illustrates the edge displacement data of all the 400 captured data bits. With the interpolation, the edge displacement data are equivalent to that obtained with a sampling rate of  $F_{DATA}$ , where  $F_{DATA}=3\text{G}$  for 3Gpbs signals.

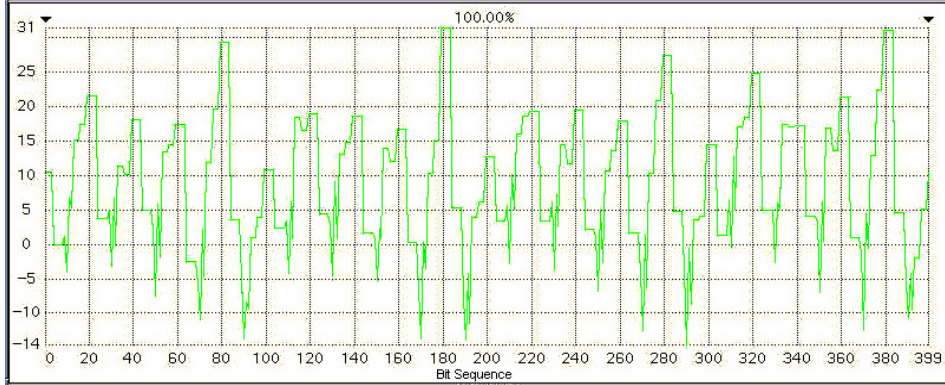


**Figure 4-5:** Edge displacement data after interpolation

Once we get the edge displacement data, we can extract the DJ and RJ components based on their properties in both the time domain and the frequency domain. Then TJ can be obtained based on DJ and RJ. Extracting jitter from the time domain and the frequency domain is not a new topic and there are many existing solutions [92], [93], [104]. Our



contribution is having developed a fast and accurate test approach by sensibly setting test parameters for data acquisition and proposing a jitter extraction procedure suitable in an ATE environment.

### 4.3.2 Time Domain Approach

In the time domain, we build the edge histograms of the test pattern to extract the RJ and DJ information of the device. The histograms are built by folding (overlying) the extracted edge displacement data at a folding frequency

$$f_{fold} = \frac{F_{DATA}}{L_{pattern}} \quad (4-16)$$

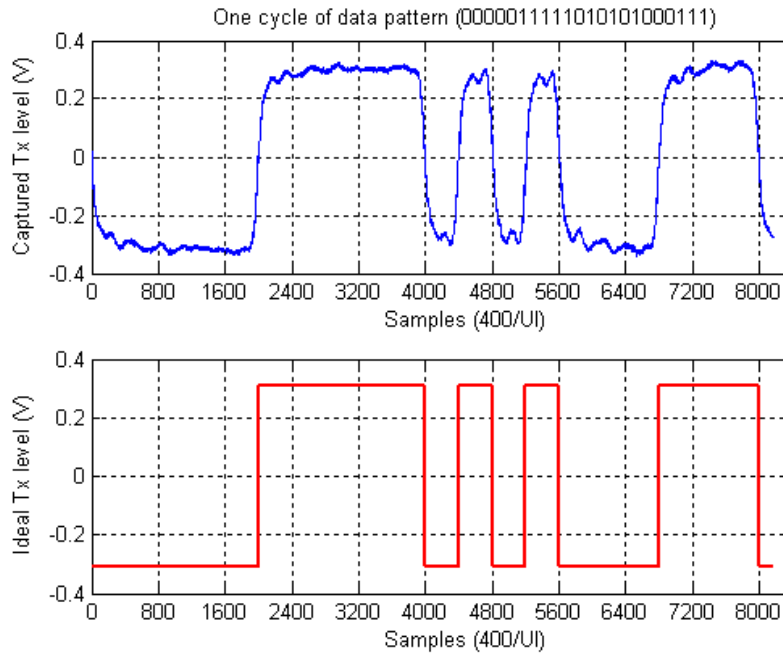


**Figure 4-6:** One cycle of the test pattern

In the 20-bit test pattern ( $L_{pattern}=20$ ), there are eight transition edges. Figure 4-6 plots one cycle of the actually captured 20-bit test pattern and the ideal waveform. Eight consecutive samples of the 160-sample edge displacement data (before interpolation) correspond to one cycle of the test pattern. We obtain the edge histograms by folding the edge displacement data in every 8 samples. The upper part of Figure 4-7 illustrates the

histograms of the eight edges. We can obtain the mean value  $m_i$  and the SD value  $\delta_i$  of each histogram. The mean values are shown in the lower part of Figure 4-7. The histogram information is used to extract the RJ, DJ and TJ of the device.

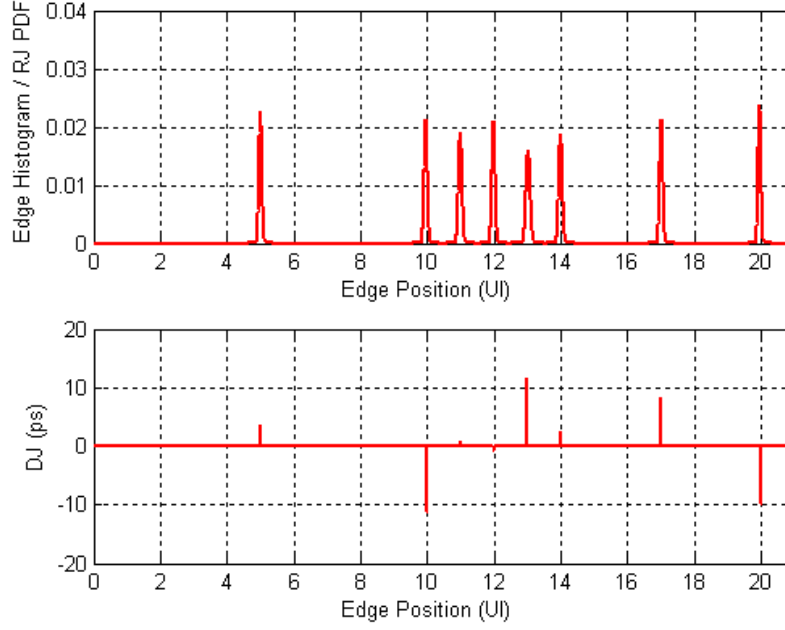


**Figure 4-7:** Histograms and DJ of all eight edges

#### 4.3.2.1 RJ Extraction

RJ is caused by random events, primarily by thermal noise in electrical components. As this kind of events exhibits a Gaussian distribution, we assume RJ is Gaussian [34], characterized by the SD value. The RJ value of the device is obtained by getting the RMS value of the SDs of the eight edge histograms:

$$RJ = \sqrt{\frac{\delta_1^2 + \delta_2^2 + \dots + \delta_N^2}{N}}$$

where  $N = 8$  for the 20-bit test pattern.

The RJ Gaussian property is also demonstrated by the actual edge histograms built from the captured data. As we can see from Figure 4-7 and Figure 4-12 (discussed later), the histograms are very close to Gaussian distributions even though there are only 20 samples

in each edge histogram. Therefore, we represent the RJ at each edge using the Gaussian function

$$p(x) = \frac{1}{\delta\sqrt{2\pi}} e^{-(x)^2/2\delta^2}$$

where  $\delta$  is the SD of the histogram at that edge. The RJ at each of the transition edges can lead us to get the TJ profile of the device once we get the DJ at each edge.

Because of the randomness of RJ, we need a lot of samples at each edge in order to capture the randomness in its histogram. Based on the analysis in Chapter 4.2.3, for the 20-bit test pattern, taking samples on 400 bits can achieve good accuracy (the statistics error is below 8%) within reasonable test time. The choice of capturing 400 bits is also proved to be reasonable by the fact that we still get similar jitter test results while we increase the number of captured bits.

#### 4.3.2.2 DJ Extraction

By definition, the mean value  $m$  of an edge histogram would reflect the DJ at that edge, which gives

$$DJ_i = m_i$$

where  $i$  is the edge index.

The DJ of a device is the maximum value minus the minimum value of the DJ values at all edges, which gives

$$DJ = \max(DJ_1, DJ_2, \dots, DJ_n) - \min(DJ_1, DJ_2, \dots, DJ_n)$$

where  $n$  is the number of total edges and  $n = 8$  in our case. The DJ value at each edge of the 20-bit data pattern is illustrated in the lower part of Figure 4-7. The DJ of the device is the peak-to-peak value of the plot, which is 23.1ps (the DJ at the 13<sup>th</sup> UI minus the DJ at the 10<sup>th</sup> UI).

The lowest DJ frequency that can be cancelled and therefore excluded from the RJ is the folding frequency  $f_{fold}$ . Any DJ whose frequency is lower than  $f_{fold}$  will affect the RJ measurement accuracy. For the 20-bit test pattern ( $L_{pattern}=20$ ) in 3Gbps applications

( $F_{DATA}=3G$ ), according to Equation (4-16) we have  $f_{fold} = 150\text{MHz}$ . In our applications, the dominant fundamental DJ frequency is the word clock frequency (discussed in Chapter 4.3.3 and shown in Figure 4-9), which is same as the folding frequency. Therefore, the DJ components do not leak into RJ.

#### 4.3.2.4 TJ Calculation

TJ is comprised of DJ and RJ. As RJ is unbounded, the TJ specification defined in any communication standard is actually the peak-to-peak value at a certain BER level. Different BER levels give different TJ peak-to-peak values. In order to extract the TJ peak-to-peak value, we need first to construct the TJ profile. As we know the DJ and RJ profile at each transition edge of the data pattern, we can construct its TJ profile through convolution. Table 4-6 lists all the RJ and DJ values at each of the eight edges shown in Figure 4-7.

**Table 4-6:** RJ and DJ Values in Figure 4-7

Position	RJ RMS(ps)	DJ (ps)	Notes
Edge 1: 5 <sup>th</sup> UI	1.64	3.5	
Edge 2: 10 <sup>th</sup> UI	1.73	-11.4	Minimum DJ
Edge 3: 11 <sup>th</sup> UI	1.95	0.7	
Edge 4: 12 <sup>th</sup> UI	1.75	-0.8	
Edge 5: 13 <sup>th</sup> UI	2.32	11.7	Maximum DJ
Edge 6: 14 <sup>th</sup> UI	1.96	2.4	
Edge 7: 17 <sup>th</sup> UI	1.73	8.4	
Edge 8: 20 <sup>th</sup> UI	1.56	-9.9	

As discussed previously, the RJ PDF at each edge can be characterized by

$$RJ\_PDF_i(x) = \frac{1}{\delta_i \sqrt{2\pi}} e^{-(x)^2/2\delta_i^2} \quad (4-17)$$

where  $i$  is the edge index and  $\delta_i$  is the RJ RMS at that edge.

As we know the exact DJ value at each edge, the TJ profile at an edge can be calculated by convoluting RJ and DJ at that edge:

$$TJ\_PDF_i = RJ\_PDF_i \otimes DJ_i \quad (4-18)$$

where  $i$  is the edge index,  $i = 1, 2, \dots, 8$ . If we denote the DJ value at edge  $i$  with  $m_i$ , according to Equations (4-17) and (4-18), the TJ PDF at edge  $i$  is represented by

$$TJ\_PDF_i(x) = \frac{1}{\delta_i \sqrt{2\pi}} e^{-(x-m_i)^2 / 2\delta_i^2} \quad (4-19)$$

To associate the TJ with BER, we need to construct the Cumulative Distribution Function (CDF) of the TJ profile at each edge:

$$TJ\_CDF_i(x) = \int_{-\infty}^x TJ\_PDF_i dx \quad (4-20)$$

The  $TJ\_CDF_i(x)$  represents the probability that the jitter (edge displacement) resides within the range of  $[-\infty, x]$ . For a zero mean Gaussian distribution, we have  $CDF(-\infty)=0$ ,  $CDF(0)=0.5$  and  $CDF(\infty)=1$ . According to Equations (4-19) and (4-20), we have

$$\begin{aligned} TJ\_CDF_i(x) &= \int_{-\infty}^x \frac{1}{\delta_i \sqrt{2\pi}} e^{-(x-m_i)^2 / 2\delta_i^2} dx \\ &= 0.5 + 0.5 * erf\left(\frac{x-m_i}{\delta_i * \sqrt{2}}\right) \end{aligned} \quad (4-21)$$

where  $erf(x)$  denotes the error function, defined as

$$erf(x) = \frac{2}{\sqrt{\pi}} \int_0^x e^{-t^2} dt$$

Once we get the TJ CDF at each edge, the TJ CDF of the device can be represented by

$$TJ\_CDF(x) = \frac{1}{8} \sum_{i=1}^8 TJ\_CDF_i(x) \quad (4-22)$$

According to Equation (4-21), we can re-write Equation (4-22)

$$TJ\_CDF(x) = \frac{1}{8} \sum_{i=1}^8 [0.5 + 0.5 * erf\left(\frac{x-m_i}{\delta_i * \sqrt{2}}\right)] \quad (4-23)$$

Figure 4-8 plots the PDF and CDF of the device TJ. According to the TJ CDF, we can get the TJ peak-to-peak value at a certain BER level by calculating the time difference between  $t_1$  and  $t_2$ :

$$TJ_{peak-to-peak@BER} = t_2 - t_1 \quad (4-24)$$

where  $t_1$  and  $t_2$  satisfy

$$TJ\_CDF(t_2) = 1 - BER / 2$$

$$TJ\_CDF(t_1) = BER / 2 .$$

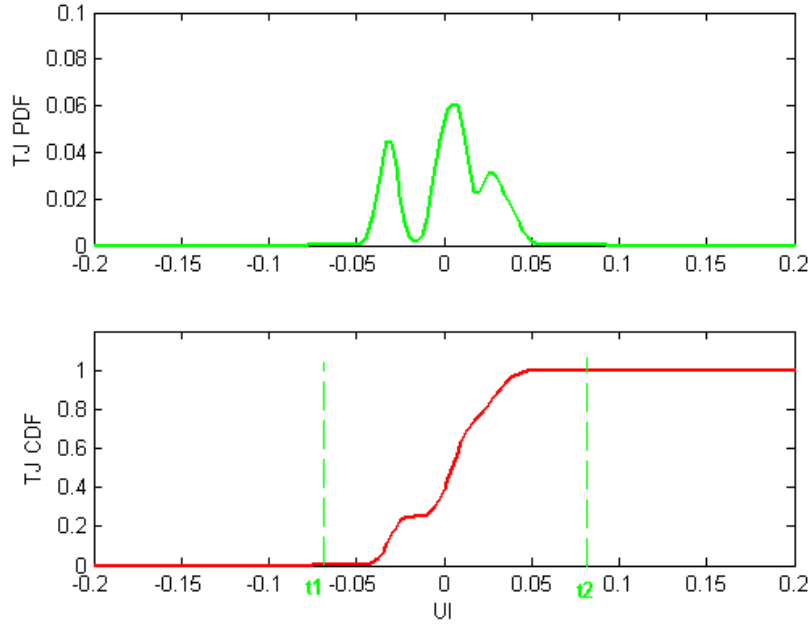


**Figure 4-8:** The PDF and CDF of the device TJ

For the TJ profile shown in Figure 4-8, according to Equation (4-24) we have

$$\begin{aligned} TJ_{pk2pk@10^{-12}} &= 0.08275UI - (-0.06975UI) \\ &= 0.15250UI \end{aligned}$$

The above calculated TJ would reflect the TJ peak-to-peak value of the device at  $BER=10^{-12}$ . In the 3Gbps example, the calculated TJ value is 50.8ps.

As we can see, the above TJ extraction process involves intensive computations and hence takes a lot of time. In production, we can estimate the RJ peak-to-peak value at a

certain BER level by multiplying the RJ RMS value with the Q factor at that BER level. The TJ value can then be obtained by summing the DJ and the RJ peak-to-peak value:

$$TJ = DJ + 2 * Q(BER) * RJ_{RMS}$$

where  $Q(BER)$  is 7.035 at  $BER = 10^{-12}$  [34].

In the above example (RJ and DJ values listed in Table 4-6), the Q factor based TJ estimation gives a TJ value of 49.1ps. This value is very close to the TJ value calculated based on the TJ CDF profile (50.8ps). Therefore, it is acceptable to use the Q factor method for TJ calculation in production.

### 4.3.3 Frequency Domain Approach

In the frequency domain, jitter components are extracted from the jitter spectrum. The TJ spectrum can be obtained by passing the edge displacement data as shown in Figure 4-5 through an FFT. Figure 4-9 illustrates the TJ spectrum of the captured signal shown in Figure 4-2. According to the spectrum, we can get the power at each frequency bin and denote it by  $Ci$ , where  $i$  is from 0 to 199.

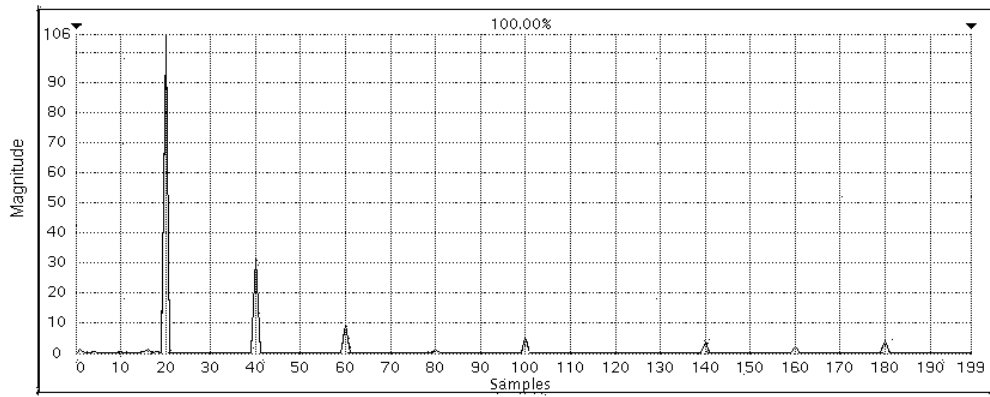


**Figure 4-9: TJ spectrum**

#### 4.3.3.1 RJ Extraction

In the TJ spectrum, RJ is the noise floor while DJ components are the impulses. The RJ RMS value is equivalent to the total noise power in the TJ spectrum. The noise power

spectrum is constructed by replacing all the DJ frequency bins in the TJ spectrum with the average of the non-DJ frequency bins.

To remove the DJ completely for RJ extraction, this approach requires the DJ frequencies to be coherent [103]: all the DJ frequencies need to be exactly multiples of the FFT frequency resolution, as a non-coherent DJ frequency appears to consist of many frequency components in the FFT frequency bins and hence contaminates the RJ spectrum. In our applications, one DJ source is the device reference clock, which is 30MHz. Another DJ source is the word clock of the device, which is 150MHz for 3G signals. The word clock is used in the HSSI to synchronize the parallel data. In addition, the ISI is also a DJ source. For the 20-bit data pattern, the ISI frequencies would be the multiples of 150MHz for 3G signals. For these facts and also according to the TJ spectrum, we know that all the DJ frequencies in our applications are multiples of 30MHz – the device reference clock frequency. In addition, as discussed in Chapter 4-2, our test setup strictly makes the reference clock frequency and the output data rate coherent. In our applications, the FFT frequency resolution is 7.5MHz for 3G signals. Therefore, all the DJ frequencies are multiples of the FFT frequency resolution. Among the 200 frequency bins, 49 of them are DJ bins (all  $C_i$  with  $i \bmod 4 = 0$ ). To calculate the noise floor of the TJ spectrum, we replace all the DJ bins with the average of the RJ bins

$$C_{RJ\_average} = \frac{1}{150} * \left( \sum_{\substack{i=1 \\ i \bmod 4 \neq 0}}^{199} C_i \right)$$

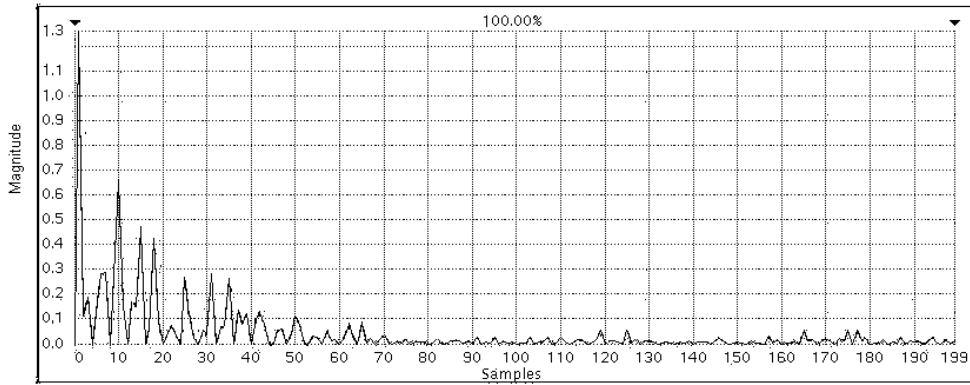


**Figure 4-10: RJ spectrum**



Figure 4-10 plots the spectrum after the above replacement. It represents the RJ spectrum of the device. According to Parseval's theorem [103], the RMS value of the RJ spectrum is the square-root-of-sum-of-power of all bins given by

$$RJ = \sqrt{\sum_{\substack{k=1 \\ k \bmod 4 \neq 0}}^{199} C_k + 49 * C_{RJ\_average}}$$

#### 4.3.3.2 DJ Extraction

In the frequency domain, we extract the device DJ component from its TJ spectrum. Similar to some commercial stand-alone jitter equipment [104], we adopt the following steps for the DJ extraction:

- (1) Obtaining the DJ-only spectrum by setting to zero all bins in the TJ spectrum that are attributable to RJ. In our case, we set to zero all the TJ bins that are not multiples of 4 (bin 4 corresponds to 30MHz)
- (2) Performing an inverse FFT on the DJ-only spectrum to generate the time-domain data. The generated data would reflect the edge displacement that is only contributed by DJ.
- (3) Getting the peak-to-peak value of the data excluding locations that actually do not have edge transitions. The peak-to-peak value is the DJ value of the device.

In step (3), we exclude the locations that actually do not have edge transitions when calculating the final DJ value. This would eliminate the artifacts that might have been introduced when we insert the edge displacement data on no-transition edges in order to perform the FFT.

Due to the DJ coherence constraint, we need to investigate the validity of each new design when using the spectrum approach for jitter extraction. One good thing is that the jitter spectrum is mainly determined by the device architecture (such as CDR and PLL structure) and the test setup (the test hardware and the test pattern). Once a design is

finalized, its jitter spectrum constitutes are constant. Therefore, the validation only needs to be done once for every new design.

#### 4.3.4 Hybrid Approach

For standalone jitter testing equipment, the jitter is extracted on the background and the users have very limited control over the extraction process. The test results may vary from one instrument to another, depending on the jitter profiles in the test signal. For example, if there is uncorrelated DJ, some instruments may bin it to RJ and hence exaggerate RJ. Because we have the total control over the jitter extraction process, when needed, our hybrid approach can use both the time domain and the frequency domain data to provide a more accurate test result

As discussed previously, we can extract the jitter components from either the time domain or the frequency domain. Each approach has its advantages and disadvantages. If the test pattern length  $L_{pattern}$  is small, such as 20, we prefer the time domain approach. The reasons are that we do not need to pay much attention to the actual DJ frequencies and that folding 20-bit data are not too complicated.

However, in some special cases, the limitation of the time domain approach may arise. As discussed in Chapter 4.3.2.2, the time domain approach cannot exclude DJ frequencies below the folding frequency from RJ. When we fold the data every 20 bits in 3Gbps applications, the lowest DJ frequency that can be excluded from RJ is 150MHz ( $F_{fold}$ ). This normally does not cause issues in our applications because 150MHz and its multiples are the dominant DJ frequencies as shown in the TJ spectrum in Figure 4-9. However, we did observe that in some special cases there are DJ components with a frequency lower than  $F_{fold}$ . One example is the reference clock bleeding through. The reference clock (30MHz in our applications) may bleed into the transmitter output through the loadboard ground or inside the device. Figure 4-11 captures in such a case the edge histograms that are folded at 150MHz but contain 30MHz DJ. In this case, the RJ

distribution is not exactly Gaussian any more due to the DJ leakage. If we still use the SD to represent the RJ, the RJ would be exaggerated.

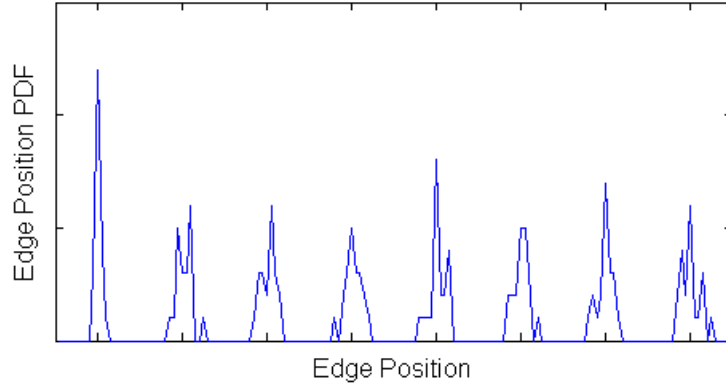


**Figure 4-11:** Histograms with low frequency DJ: SD = 4.08Ps

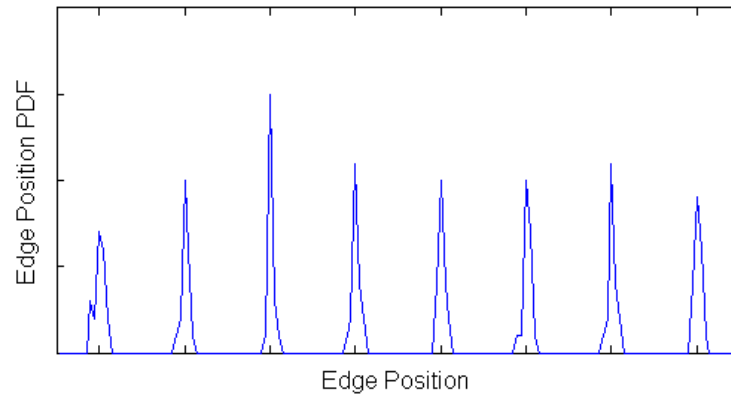


**Figure 4-12:** Histograms after removing low frequency DJ: RJ = SD = 1.70Ps

To exclude the 30MHz DJ frequency from RJ in the time domain, we need  $F_{fold}=30\text{MHz}$ . According to Equation (4-16), for 3Gbps applications we need the folding pattern length  $L_{pattern}=100$ . To build edge histograms, we need to capture at least 2000-bit data, assuming capturing 20 cycles. In production, we cannot afford the long test time required for the acquisition and the processing of such large amount of data. Instead of lowering the folding frequency, we solve this problem by removing the low frequency DJ from the edge displacement data before building edge histograms. We set the specific low frequency DJ components in the jitter spectrum to zero and then perform an inverse FFT

to get the edge displacement data that does not contain the low frequency DJ. Figure 4-12 plots the histograms where the low frequency DJ has been removed. The standard deviation of the histogram would reflect the true RJ of the device. This approach is also useful when we cannot get accurate RJ measurements using the frequency domain approach because DJ components are not coherent. We can use the hybrid approach to remove the uncorrelated jitter bins before calculating RJ.

### 4.3.5 Limitations of Each Approach

As already mentioned, there are advantages and disadvantages in each of the two jitter extraction approaches presented. To achieve a high accuracy, the frequency domain approach needs DJ components to be constant and also be coherent with the FFT frequency resolution. Our TJ spectrum demonstrates that this requirement is satisfied in our applications. However, in some applications, the DJ frequencies may not be coherent and even may vary from device to device. In this case, the frequency leakage may degrade the jitter test accuracy if we only rely on the frequency domain approach.

The time domain approach requires that the major DJ frequencies are multiples of the folding frequency in order to avoid DJ leakage. If we have low frequency DJ, the folding frequency must be also low. It therefore requires capturing a larger number of data bits and hence needs longer test time. Although the hybrid approach can save some test time in this case, it still requires that the low frequency DJ components are consistent.

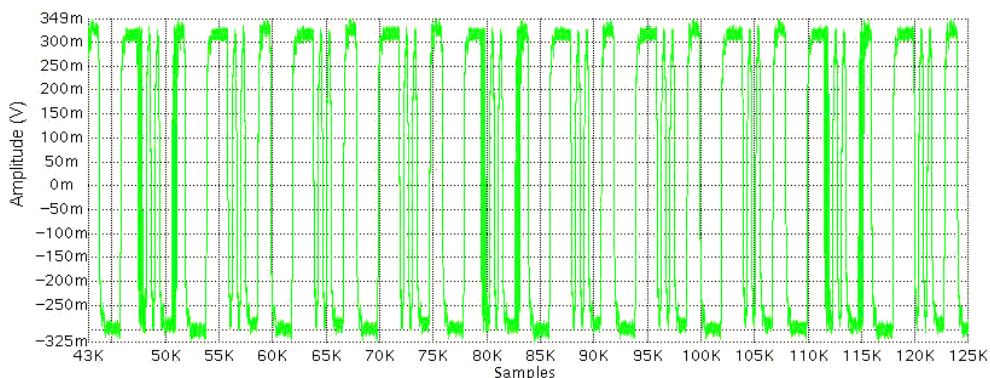


**Figure 4-13: DJ leakage**

To detect the possible DJ leakage and uncorrelated DJ, we also implement a simple eye mask test. Figure 4-13 shows an example of captured waveform with DJ leakage. We calculate the eye mask by extracting the zero-crossing width of each edge and then overlay them together. The eye mask includes all kinds of jitter components, including non-Gaussian RJ.

## **4.4 Experimental Results**

To evaluate a jitter test solution used in mass production, throughput and accuracy are the two most important criteria. Our experimental results demonstrate the superiority of our proposed solution in both throughput and accuracy. In the ATE environment, every millisecond adds to the cost of the product. As discussed in Chapter 4-2, all the test parameters (pattern length, effective sampling rate, number of samples, and undersampling rate) in our solution have been optimized to keep the test time as short as possible while still capable of accurately capturing all the information we need for the transmitter tests. For both 3Gbps and 6Gbps applications, we managed to finish the entire transmitter testing within 100 milliseconds, including the data capture, the jitter extraction and other transmitter tests, such as transmitter function and rising/falling time tests.

Accuracy shows how close the measured jitter value is to its true value. The true value is usually obtained using a bench instrument whose accuracy has been verified and is widely accepted. Repeatability shows whether the test gives the same or similar result from run to run and from time to time for the same device while other conditions, such as supply voltages and temperature are the same. We have conducted intensive exploration of the repeatability and accuracy of our solution.

### **4.4.1 Bench Correlation**

We have correlated our ATE jitter test results with the results obtained using the commercially available jitter test instrument Tektronix J1T3. Tektronix J1T3 is favored by

many test/application engineers for its excellent jitter extraction ability and accuracy. Table 4-7 shows the results from 3 correlation devices. The ATE data in this table records the jitter mean values from the time domain approach with 20 runs for each device in a 3Gbps application. The repeatability of our ATE solution is discussed later.

**Table 4-7: Jitter Measurement Results between ATE and Bench**

Jitter/ Device	Device 1		Device 2		Device 3	
	Bench	ATE	Bench	ATE	Bench	ATE
RJ	1.9	1.92	2.05	1.83	2.02	1.81
DJ	19.9	21.5	27.3	29.4	25	26.5
TJ	40.8	48.38	49.3	55.02	45.8	51.84

As we can see, the RJ difference between the bench and ATE is within 0.2ps; the DJ difference is within 3ps (DJ from ATE is consistently slightly higher than that from the bench equipment). As we know, absolute correlation in numbers for different jitter test solutions rarely happens. Considering this is done on ATE with a completely different instrument and setup from the bench environment, the correlation result is very good.

One reason for the higher DJ on ATE is that the signal path on ATE is longer than that on bench. The longer signal path can introduce more ISI, and hence results in higher DJ on ATE. In addition, the different TJ extrapolation algorithms between the bench and ATE also introduce difference in the final TJ report.

In Table 4-7, the three correlation devices generate similar amounts of jitter. We further conduct the correlation between ATE and bench equipment using an alternative reference clock to generate higher RJ and DJ. More details and correlation data are presented in Chapter 4.4.4.

## 4.4.2 Correlating Two RJ Approaches

As we have discussed, the RJ can be extracted from both the time domain and the frequency domain. The frequency domain approach is less pattern-dependent as it does

not involve building histograms. This approach is preferred on ATE if we need to investigate the jitter performance with different test patterns. However, the results from this approach need to be verified as the extraction process involves data interpolation and jitter component replacement. These steps might introduce errors as the assumptions for these steps may become invalid at a certain condition. In addition, the frequency domain approach requires that the DJ frequency leakage is negligible, which may not be satisfied in some cases.

On other hand, the time domain approach is very straightforward. It can be used to correlate the test results from the frequency domain. Figure 4-14 shows the test results of a device with 20 runs on ATE, where *RJ\_Spectrum* is the RJ value from the frequency domain approach, and *RJ\_Timing* is the RJ value from the time domain approach. It demonstrates that both approaches exhibit good repeatability and the correlation is also very good.

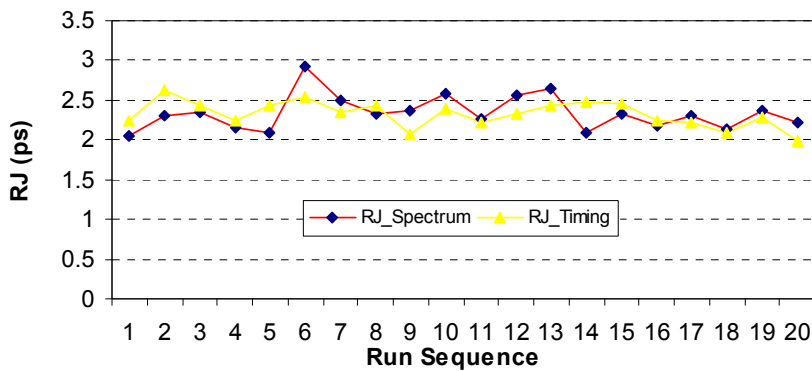
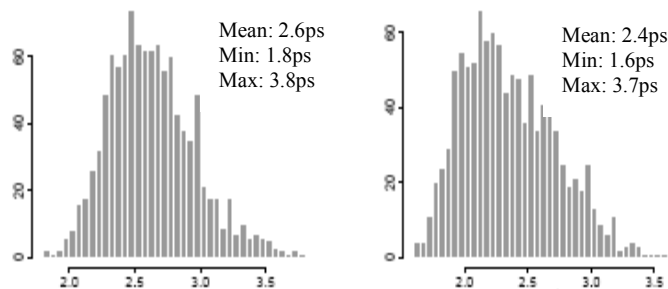


**Figure 4-14:** RJ repeatability and correlation

We also evaluated the correlation between the two approaches across PVT corners. Figure 4-15 plots the jitter distribution across the PVT corners from both approaches, where the *x*-axis denotes the measured RJ values and the *y*-axis represents the number of hits. The difference between the two approaches is very small: the measured jitter mean difference is only 0.2ps and distribution profiles are very similar.



(a) RJ\_Spectrum distribution      (b) RJ\_Timing distribution

**Figure 4-15:** Jitter distribution across PVT corners

As we can see, the device-to-device correlation between the bench and the ATE time domain approach is very good. On ATE, the time domain and frequency domain approaches also correlate well from either multiple runs for a single device or a larger number of devices across all conditions. These experiments demonstrate the excellent accuracy and repeatability of our jitter test solution.

### 4.4.3 Impact of Test Patterns

In our testing up, we use a 20-bit test pattern. Even though the test pattern includes both high transition density and low transition density data, the length of the pattern is short and the actual data in real applications has more variations. In order to make sure that the test results using the 20-bit pattern can represent the performance of the device in a real environment, we investigate the test pattern impact to jitter measurement results. Table 4-8 lists the jitter measurement results using the 20-bit test pattern, the 128-bit PRBS pattern discussed in Chapter 3 and a clock pattern (101010..) respectively.

We take the measurements from an ATE loadboard. Instead of connecting the transmitter output to the digitizer on ATE, we connect the transmitter outputs to the bench instrument JIT3 to investigate the impacts of the test patterns. There are three main benefits of this approach:

- 1) It adopts the real production environment and hence can directly use the results to evaluate our ATE solution



- 2) Measurement results from bench equipment in general are more acceptable and give more confidence level to the overall experiment results
- 3) There is no need to develop ATE test program for new test patterns.

**Table 4-8: Jitter Measurement Results Using Different Test Patterns**

Jitter/Pattern	20-bit	PRBS	1010
RJ	2.07	1.99	2.25
DJ	41.3	48.8	34.5
PJ	26.3	30.25	23.1
DCD	1.09	0.84	2.37
ISI	13.9	17.75	9.37
TJ	60.8	65.34	56.5

As we can see, the jitter numbers from all the three test patterns are very close. The 20-bit test pattern generates a similar RJ value compared to the 128-bit PRBS pattern or the clock pattern. It also generates moderate DJ: slightly lower (less than 5ps) than the PRBS pattern and slightly higher than the clock pattern (the difference is caused by ISI). Therefore, the jitter measurements from the 20-bit test pattern we used provide a good representation of the true jitter performance of the device.

#### 4.4.4 Impact of the Reference Clock

As shown in Figure 4-1 -- Transmitter Test Setup for Data Acquisition, the HSD on ATE provides a reference clock to the transmitter PLL. The transmitter output data are synchronized by an internal transmitter clock generated by the PLL. The quality of the reference clock can affect the jitter in the transmitter output signal.

To investigate the reference clock impact to the final transmitter jitter numbers, instead of using the HSD clock, we create another clock using the AWG6000 on the ATE as the reference clock to the transmitter. The AWG clock is generated by directly storing consecutive zeros and ones in the AWG according to the transmitter reference clock

frequency requirement. We then measure the transmitter jitter using the two different reference clocks. Table 4-9 shows the measurement results using the bench equipment JIT3 and our jitter extraction techniques on ATE.

**Table 4-9:** Reference Clock Impacts to Transmitter Jitter Measurement.

Jitter / Device	HSD clock		AWG clock	
	Bench	ATE	Bench	ATE
RJ	2.07	2.3	5.7	5.9
DJ	41.3	29.07	50.6	41.06
TJ	60.8	67.0	112.1	127.8

As we can see, using the reference clock generated by AWG (AWG clock), the transmitter exhibits higher jitter than using the reference clock generated by an HSD channel (HSD clock). One reason is that the AWG has much higher bandwidth than the HSD channel, and hence more high frequency jitter in the AWG clock transfers into the transmitter clock. Table 4-9 also further verifies our ATE jitter extraction techniques: the ATE results correlate with the bench results under different jitter levels.

The intrinsic jitter in reference clocks can be reduced. A method is presented in [130] to reduce jitter in clock signals at the cost of extra hardware. It uses real-time averaging to combine multiple signals in order to produce one output signal with much lower random jitter. The reduced jitter can be expressed theoretically by

$$\delta_{output} = \frac{\sqrt{\delta_1^2 + \delta_2^2 + \dots + \delta_N^2}}{N}$$

where  $\delta_{output}$  is the jitter of the output signal,  $N$  is the number of combined signals and  $\delta_i$  ( $i=1, 2, \dots, N$ ) is their jitter. The experimental result in [130] shows a 3x reduction in jitter (from 4ps to 1.3ps) by combining eight signals. This is very close to the above theoretical analysis. Interestingly, similar to our CTL Gaussian generator from Chapter 5.4.1, it exploits the central limit theorem.

Even though a better reference clock can help report better transmitter jitter numbers, in production we need to try mimicking the real application environment, where the reference clock is usually provided by a crystal oscillator. We correlate the ATE result (the reference clock is provided by an HSD on ATE) with the bench evaluation board result where the reference clock is generated by a crystal oscillator, and the results are very close.

#### 4.4.5 Extending to 6 Gbps Applications

Although our previous discussion and experiments concentrate on 3Gbps applications, our approach applies to any data rates as long as the digitizer bandwidth is sufficient. Because the bandwidth of our ATE instrument is above 9 GHz, we can extend our transmitter jitter test solution from 3Gbps applications to 6Gbps applications. For 6Gbps applications, we only need to adjust the reference clock and the under-sampling clock according to the data acquisition principles discussed in Chapter 4-2 and the test setup parameters listed in Table 4-4. Figure 4-16 shows part of the 6Gbps waveform captured using our solution.

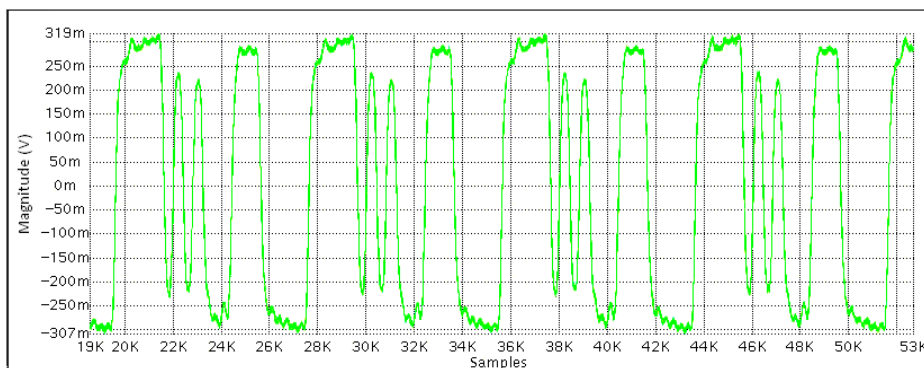


**Figure 4-16:** Captured 6G waveform (only 45 bits shown)

Based on the above waveform, we can extract the jitter components using exactly the same scheme as discussed for 3G signals. Figure 4-17 shows the measured jitter at 6G from one device with 20 runs, where the upper part plots both DJ and RJ and the lower part plots RJ only.

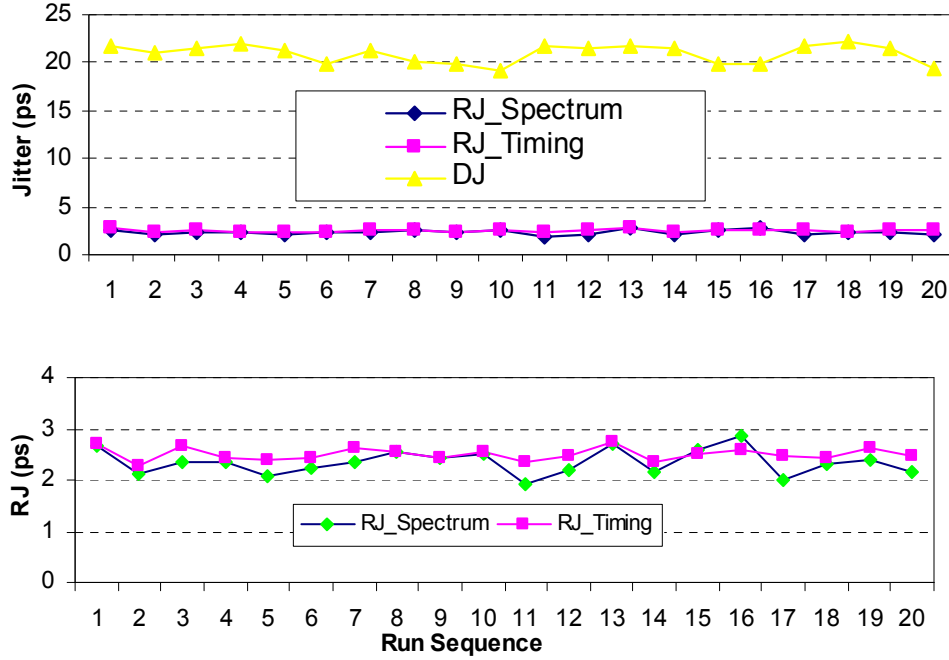


**Figure 4-17: RJ and DJ at 6G data rate**

At 6Gbps data rate, our solution still provides similar accuracy and repeatability to that at 3G applications. As shown in Figure 4-17, the RJ variation from run to run is within  $\pm 0.5$ ps. The measured jitter on ATE also correlates well with bench results.

## 4.5 Summary

In this Chapter, we have presented a systematic approach to extract transmitter jitter. By just capturing an adequate number of samples with adequate resolution, we can achieve the whole transmitter testing within 100ms while keeping sub pico-second jitter accuracy. We make it feasible to run the time-consuming jitter test in an ATE environment with data rates up to 6Gbps.

To extract jitter, we first obtain the edge displacement data by comparing the actual zero-crossing points with their ideal positions. According to the edge displacement information, we can extract jitter from either time domain or frequency domain. To

guarantee accuracy while keeping test time short, we also propose a hybrid approach to prevent low frequency DJ from bleeding into RJ. Experimental data demonstrates the validity of our approaches.

---

# Chapter 5 – Testing HSSIs with or without ATE Instruments

---

As we discussed in Chapter 3 and Chapter 4, the ATE-based solutions greatly speed-up the receiver jitter tolerance and transmitter jitter qualifications. However, there are two major limitations in applying the ATE-based approaches for HSSI qualifications.

The first one is the number of ATE instruments available. For each HSSI, we need an AWG and a digitizer in order to do parallel testing. Nowadays, there are some devices with a few tens or even more than 100 HSSIs. No ATE platform can accommodate so many AWGs and Digitizers. In addition, the AWGs and Digitizers that can handle multiple GHz signals are very expensive. The AWG/Digitizer approach is prohibitive from the cost point of view for devices with multiple HSSIs.

The second limitation is the lack of high-speed instruments for the latest HSSI receiver testing. AWG6000 is the best AWG on ATE from what we know in terms of speed, but it can only perform jitter tolerance testing up to 3Gbps. Several ATE suppliers have provided production pin-card solutions up to 6Gbps. However, for higher speed applications, such as 10Gbps and above, systematic ATE solutions are not mature yet even though there is research in that direction [131].

To overcome these limitations, this chapter presents HSSI testing techniques that do not necessarily rely on ATE instruments. We first introduce an FPGA-based bit error detection scheme for HSSI function validation. We then present a low-cost loopback-based testing scheme, where a novel jitter injection method is proposed using the latest phase delay lines. The loopback scheme can be applied to test HSSIs with data rates up to

12.5Gbps. It is also suitable for multi-lane HSSI testing. By using state-of-the-art high-speed relays, we combine the ATE solutions and the loopback solution along with the FPGA-based BERT to provide a more versatile scheme for HSSI validation and testing. In addition, we further investigate the amplitude noise affect on the BER and explore the unparallel advantages of our noise generator in generating noise samples for low BER evaluation [6].

## 5.1 FPGA-based Bit Error Detection

In Chapter 3.3, we present two mechanisms to detect bit errors. The ATE based solution utilizes high-speed digital channels on ATE to compare the receiver recovered parallel data with the expected data. There are two limitations for this approach. First, it is very difficult to achieve synchronization between the DUT and ATE -- it depends on some special macros from the ATE vendor. In addition, it requires many high-speed digital channels, which are expensive and sometimes might not be available. Even though the DFT-based approach almost does not need any ATE instruments, it needs extra silicon area and design effort to implement and has to be planned before the HSSI is designed. In addition, once the design is finished, we can only choose the patterns that have been designed into the DFT; we do not have the ability to program new patterns.

To overcome these limitations, we explore FPGA-based approaches. In recent years, FPGAs have been widely used in testing applications because of their strong capabilities in generating test patterns, providing high-speed interfaces and performing configurable user-defined functions [53], [96], [135], [138]. One important FPGA application is Built-Off-Self-Test (BOST), where the test or BIST circuit is implemented in an FPGA that is placed off the chip on the test fixture [105]. One example of the BOST approach is presented by Sunter and Roy in [72], where an FPGA on a DUT interface board is used to test HSSIs. This BOST approach implements three BIST techniques [44], [106], [107] in the FPGA. In this section, we introduce a BOST approach for bit error detection [6]. Implemented in an FPGA, our approach performs similar function as the DFT feature discussed in Chapter 3.3.2 does, but the user has the freedom to set the test pattern. The

solution does not need any ATE instrument or any DFT feature, and can be used to test almost any HSSI.

As discussed in Chapter 2.1.2, the basic concept of BER measurement is as follows: the pattern generator sends a data stream to a DUT; the error detector conducts a bit-by-bit comparison of the received signal from the DUT and records bit errors. According to applications, a BER tester (BERT) can be either serial or parallel.

### 5.1.1 Implementing a Serial BERT

A serial BERT sends serial bit sequences to a DUT and evaluates the output from the DUT. The DUT can be any serial digital communication link. The structure of a serial BERT is proposed and shown in Figure 5-1. In this scheme, the shift register shift\_reg1 and the gate XOR1 form a LFSR. As the pattern generator of the serial BERT, the LFSR generates pseudo random bit sequences (PRBSs). These sequences are then sent to the DUT.

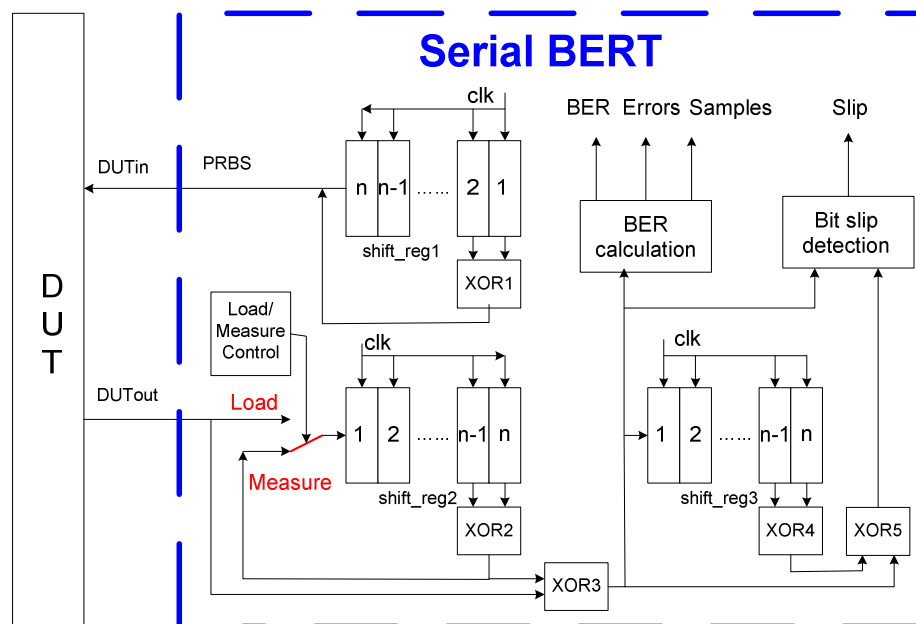


**Figure 5-1:** Block diagram of a serial BERT



Before a measurement begins, the load/measure switch is set to be in load state until the shift\_reg2 is full loaded with the contents of the shift\_reg1. The switch is changed to measure state to start the BER measurement. The shift register shift\_reg2, the switch and the gate XOR2 are used for synchronization. They generate a reference pattern by replicating the PRBS from the shift\_reg1, but delaying the phase. During the synchronization process, it is assumed that all the bits are correctly transmitted. The gate XOR3 serves as a comparator. It compares the pattern from the DUT to the reference pattern. If the test pattern is correctly transmitted by the DUT, then the two inputs of XOR3 should be the same value in each clock cycle. In a real BER measurement, the output of XOR3 is monitored every clock cycle: if a '1' is detected, a transmission error is counted; otherwise, the transmission is error-free.

In a real communication system, the transmission errors are in forms of a single-bit error, error bursts or bit slips. Bit slips result from a bit loss or a bit repeat. If a bit slip happens, only the repeated or lost bits should be counted as errors. We employ a mechanism to distinguish between error bursts and bit slips and to eliminate false long-term errors. In Figure 5-1, the shift register shift\_reg3 and the gates XOR4 and XOR5 perform bit slip detection. The solution is based on the fact that the addition or superimposition of two PRBSs shifted in phase relative to each other produces another PRBS [108]. By monitoring the output of XOR3 and XOR5, it can be determined whether a bit slip happens.

### **5.1.2 Implementing a Parallel BERT**

A parallel BERT is used to test communication interfaces that transmit parallel data. The implementation of the parallel BERT is based on the serial BERT. We build a  $k$ -bit parallel BERT using  $k$  independent serial BERTs, where  $k$  is the width of the parallel data (bit0 ~ bit( $k$ -1)). The parallel BERT sends pseudo-random word sequences (PRWSs) to the DUT. In order to achieve randomness in the generated sequences, the independence of each serial BERT is important. Therefore, the lengths of the shift registers in the serial BERTs should be different in order to have different periods [109].

We need to remove the circuit redundancy when  $k$  independent serial BERTs are directly put together to implement a parallel BERT. Each of the serial BERTs has circuits for the load/measure switch control and bit slip detection. However, the *load/measure* switches for the parallel data bits should change the state at the same time. Therefore, only one of the  $k$  such control circuits is needed for the switch control and word slip detection. Figure 5-2 shows the structure of the proposed parallel BERT. In the design, the serial BERT control circuitry for bit0 is used for the load/measure switch control and the word slip detection.

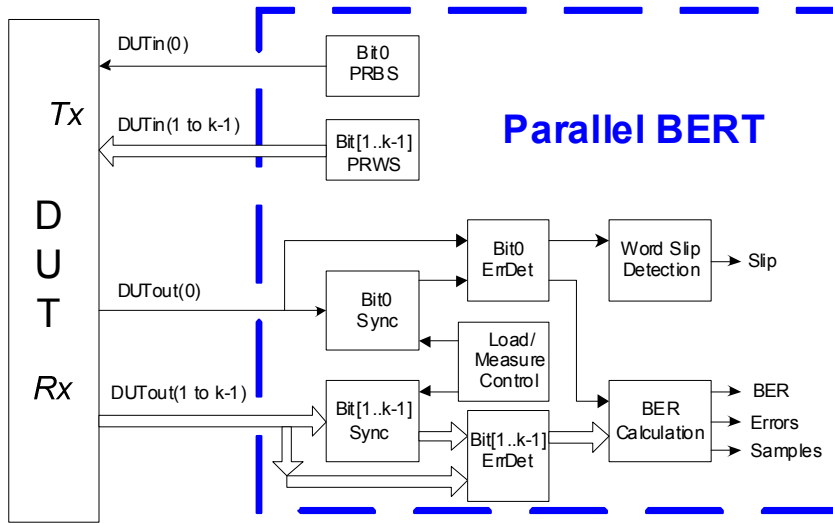


**Figure 5-2:** Block diagram of the parallel BERT

### 5.1.3. HSSI Testing Demonstration

The BERT design has been built in VHDL, and can target almost any FPGA devices. To demonstrate the functionality of the BERT, we use it to test the HSSI in the Altera Mercury FPGA EP1M120F484C7 [10]. The Mercury HSSI can transmit and receive high-speed serial data streams with speed up to 1.25Gbps. Figure 5-3 shows the setup used to test the HSSI.

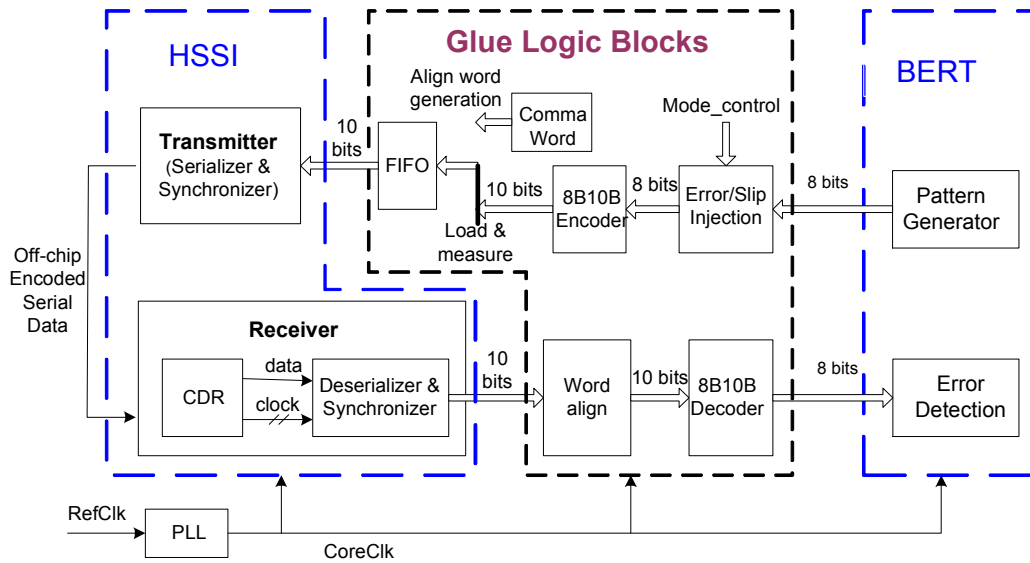


**Figure 5-3:** HSSI testing setup to verify BERT functionality

In the testing setup, the HSSI is built by instantiating the Altera Mercury Gigabit Transceiver MegaCore [110]. The data width of the BERT is 8 bits. The glue logic is developed to interface the BERT and the HSSI. The Error/Slip Injection block inserts errors or word slips and could be used to test/verify the BERT. The 8B10B encoder encodes the 8-bit sequences to 10-bit sequences to ensure enough bit transitions in the serial link for data recovery as discussed in Chapter 2.1.1. A FIFO is used to ensure that there is always data ready for transmission after a testing begins. Comma words are inserted at the start of the testing for word alignment. The 8B10B decoder recovers the 8-bit PRWSs sent by the BERT.

The whole testing setup (the HSSI, BERT and the glue logic blocks) is implemented in VHDL, targeting the EP1M120F484C7 device using Quartus II software. The synthesized results are downloaded onto an Altera Mercury CDR Demo board. The outputs of the transmitter are connected to the inputs of the receiver by two Sub-Miniature type-A (SMA) cables. In this setup, the data signal is running at 1.5Gbps. Higher data rates can be realized using higher performance FPGAs.

We obtained zero BER both from simulations and from running real tests on the board when no error or bit slip was injected. We also captured the transmitter output signal using a scope and verified the sequence was what we expected. When the slip was injected on the test board, the Error Detector detected bit errors and the slip output was asserted. When only bit errors were injected, the BERT reported bit errors but bit slip output was not asserted. The experiment results demonstrate that the Mercury HSSI can successfully serialize the parallel data, transmit the high-speed serial data over the cables, and recover the serial data sequence back to the original parallel data. The experiment also verifies the FPGA-based bit error detection scheme. Further experiments using the BERT will be demonstrated in Chapter 5-4.

## **5.2 Loopback Testing with Jitter Injection**

### **5.2.1 Testing Setup**

In Chapter 3, we present an ATE-based HSSI receiver testing scheme, where controllable amounts of jitter are injected through the AWG. This approach can successfully test the jitter tolerance performance for data rates up to 3Gbps. For data rates above 3Gbps, we cannot use the AWG-based jitter injection approach because the maximum sampling rate of the AWG is limited to 6Giga samples per second.

To overcome the ATE instrument limitation, we propose a loopback testing scheme. By looping the transmitter output back to the receiver input either internal or external, loopback testing has been widely used to check the functionality of HSSIs [69], [111]. The HSSI testing demonstrated in Chapter 5.1.3 is one example of the external loopback. Traditional loopback approaches do not have the capability to qualify design parameters, such as transmitter jitter and receiver jitter tolerance. Recent research shows the directions that use external loopback to verify design parameters. However, they need either special DFT features or extra special instrument modules [98], [99].

Our approach does not rely on any DFT features or special instruments; it only needs a few extra components that can fit into a testing loadboard. The approach is especially attractive for testing multiple-lane HSSIs or HSSIs with data rates above 6Gbps, where mature ATE solutions are not available. Figure 5-4 shows the block diagram of the proposed loopback testing. In this approach, we inject controllable amount of jitter to the output of the transmitter signal using a phase delay line and then loop the signal back to the input of the receiver. When the injected jitter is below a certain level, the receiver should be able to recover the transmitted data. Otherwise, the device is defective. The details of the phase delay based jitter injection are discussed in Chapter 5.2.2.

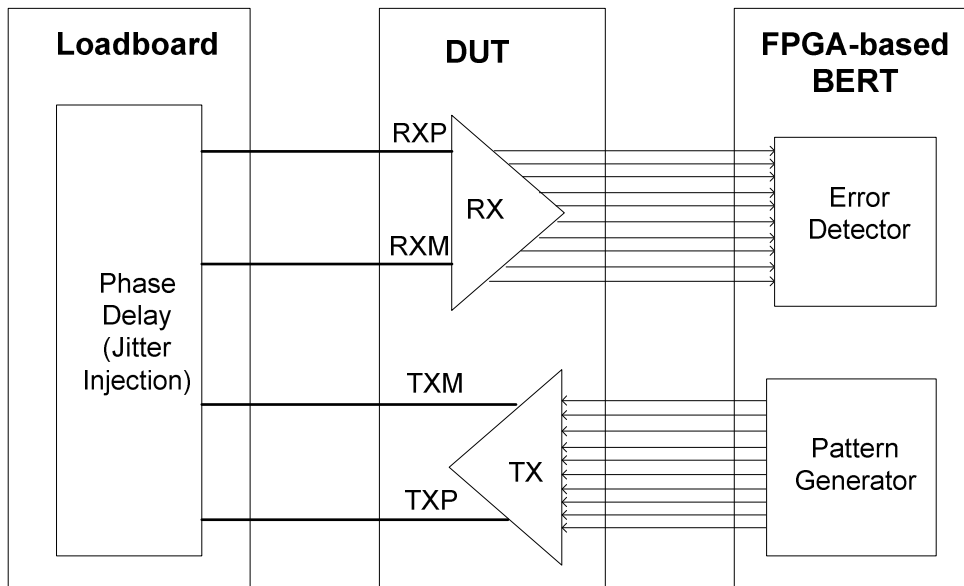


**Figure 5-4:** Loopback-based jitter testing

In the above loopback testing scheme, we use the FPGA-based BERT discussed previously. The Pattern Generator in the FPGA provides parallel data to the transmitter. The Error Detector compares the recovered data with the transmitted data and records errors. The FPGA may also need to provide some glue logic. The FPGA-based BERT is not needed if we can still detect bit errors using the digital channels on ATE [2] or DFT features if they are available.

### 5.2.2 Phase Delay Based jitter Injection

A delay line or a phase delay line is a component where the input signal reaches the output of the component after a known period of time has elapsed [112]. The elapsed time or delay time ranges from femtoseconds to microseconds. Delay lines or phase delay lines have been widely used in electronics and derivative fields such as telecommunications and testing [97], [133].

Early delay lines were implemented with a RC-based ramp generator and a comparator that transitioned the delay line output when the ramp generator reached a certain voltage level. Calibration was done at the factory by blowing a serial fuses until the desired delay was achieved. The RC-based delay lines normally did not have temperature compensation provision. More sophisticated delay lines then were developed using a VCDL in conjunction with a compensation circuit to reduce delay variation across process, voltage and temperature [113].

Today, ultra wideband phase delay lines have been developed using III-V technologies, such as InGap or InP Heterostructure Bipolar Transistor (HBT) devices [116]. InGap HBT is a proven reliable technology that has been widely used in large volume wireless applications. It exhibits characteristics such as high cutoff frequency, high linearity and temperature stability, suitable for ultra wideband device design. InP HBT has the highest cutoff frequency among the III-V available technologies [114], [115]. One unique product on the market is the phase delay line iT4036. It was developed by GigOptix [39] using high speed HBT Emitter Coupled Logic (ECL) topology realized in InP [116].

The iT4036 is ultra-wideband, operating at speeds up to 12.5Gbps for data signals and 11.7GHz for clock signals. It can provide tunable phase delay up to 120-ps in a single device. Delay control can be either differential or single-ended and the delay control bandwidth is up to 1GHz. Its output amplitude is 400mVpp in single-ended mode and 800mVpp in differential mode. Figure 5-5 shows the device diagram of the iT4036 [116].

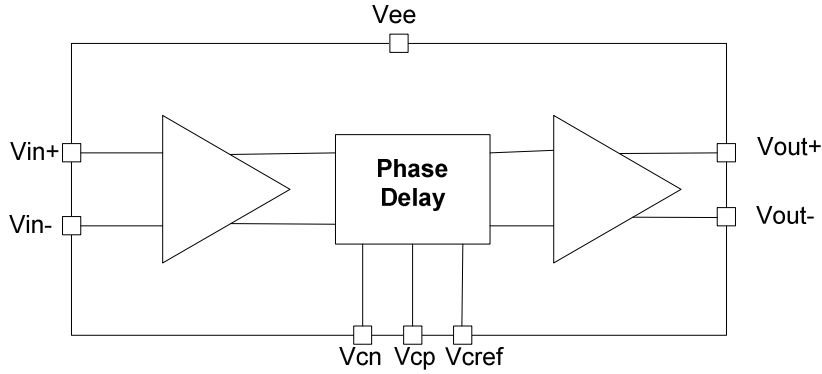
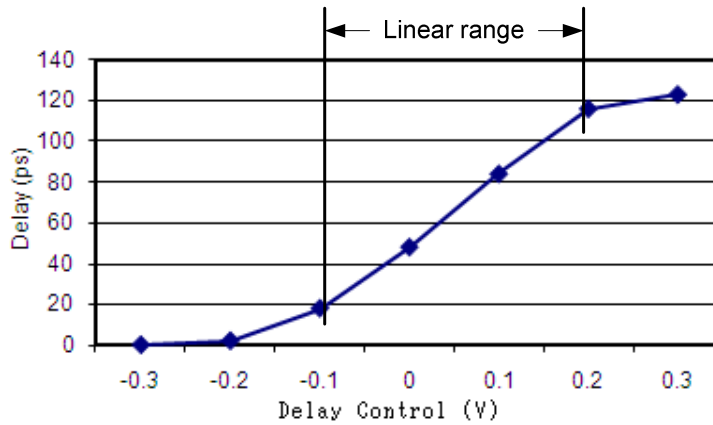


**Figure 5-5:** Block diagram of iT4036

Traditionally, a phase delay line is only used to provide a constant delay controlled by a constant voltage in the delay control input. Considering the high bandwidth both in the signal path and the delay control path, we propose using the phase delay line for jitter injection to test HSSIs. The ideal is to apply an AC signal to the delay control pins. The delay for each data edge may be different, depending on the amplitude of the control signal at the instance of each edge. This is equivalent to injecting deterministic jitter to the input signal. Because the delay control bandwidth is up to 1GHz, we can inject DJ with frequencies up to a few hundreds MHz, suitable for HSSI jitter testing and characterization.

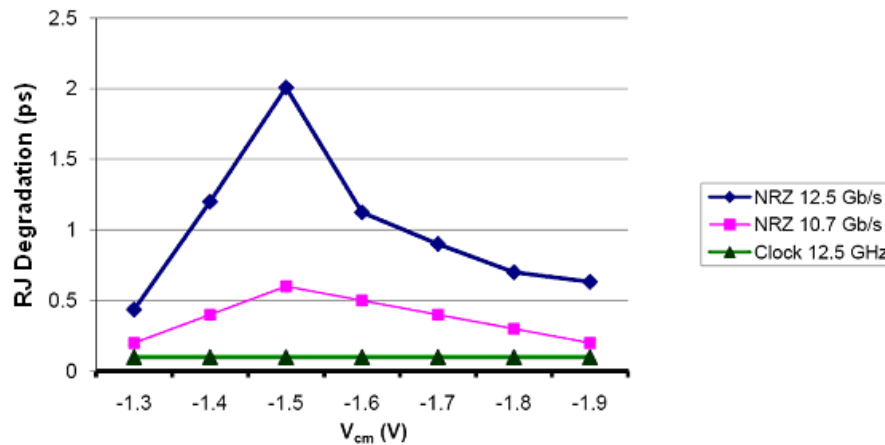
In our proposed jitter injection scheme, we connect the HSSI transmitter output to the input of the delay line. Then the output of the delay line is connected to the input of the HSSI receiver. Jitter is injected by connecting an AC control signal to its delay control pins  $V_{cn}$  and  $V_{cp}$  to dynamically control the phase delay between the input signal and output signal. By adjusting the amplitude of the delay control signal, we can control the DJ injected to the data signal.

Figure 5-6 shows the relationship between the delay control signal and the phase delay [116]. The relationship between the delay control voltage and the phase delay is very close to linear between the 20ps to 110ps delay range. Therefore, we can conveniently control the amount of injected DJ through adjusting the amplitude of the AC signal on the delay control pins in this linear range, and the following discussion refers to this range.



**Figure 5-6:** Delay vs. delay control

To linearly control the injected TJ, we need to consider the RJ degradation. The RJ degradation is the RJ introduced by the phase delay line. It can be characterized by obtaining the difference in RJ between the input signal and the output signal of the phase delay line. Figure 5-7 shows the RJ degradation for 12.5Gbps NRZ, 10.7Gbps NRZ and 12.5Gbps clock signals at different control voltage levels with  $V_{cp}$  tied to  $V_{ref}$  [116].



**Figure 5-7:** RJ degradation vs.  $V_{cm}$  (courtesy of GigOptix)

Because the phase delay line shows a linear relationship between the injected DJ and the delay control magnitude, the RJ degradation needs to be constant in order to also keep a constant offset between the injected DJ and TJ. As discussed in Chapter 3.4, a constant



offset between injected DJ (or PJ) and TJ, such as the one shown in Figure 3-17, enables us to translate TJ tolerance testing into DJ/PJ tolerance testing. To maintain a constant offset between the injected DJ and TJ, according to Figure 5-7, a clock signal is preferred when we use the phase delay based new jitter injection technique at the 10Gbps data rate range.

### 5.2.3 Experimental Results



**Figure 5-8:** Phase delay line iT4036 evaluation board (courtesy of GigOptix)

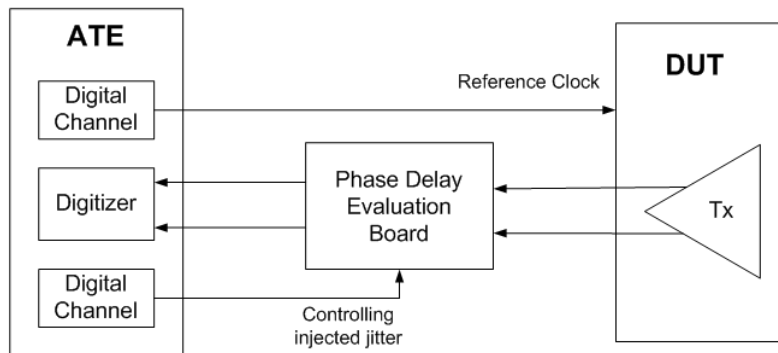


**Figure 5-9:** Phase delay evaluation setup

We demonstrate the phase delay line-based jitter injection technique on an iT4036 evaluation board as shown in Figure 5-8. The input and output signals of the delay line on the evaluation board are routed to SMA connectors. In our experiments, we connect the transmitter output of the DUT to the input of the delay line through cables and then capture the output of the delay line using the digitizer available on ATE (the digitizer was discussed in Chapter 4). The delay control signal is provided by a digital channel on the ATE. Figure 5-9 shows the test setup. The digital channel provides a clock signal and the

injected jitter can be adjusted by changing the  $V_{oh}$  and  $V_{ol}$  levels of the digital channel. The injected jitter frequency can also be adjusted according to test requirements.

Figure 5-10 plots the captured waveform of a 6 Gbps NRZ data signal from the output of the delay line with 400 samples for each bit. As we can see, the output signal is very clean. The rise/fall time is very short as specified in the delay line specification. The plot shows the output amplitude around 900mVpp, which is also close to the delay line specification (800mVpp).

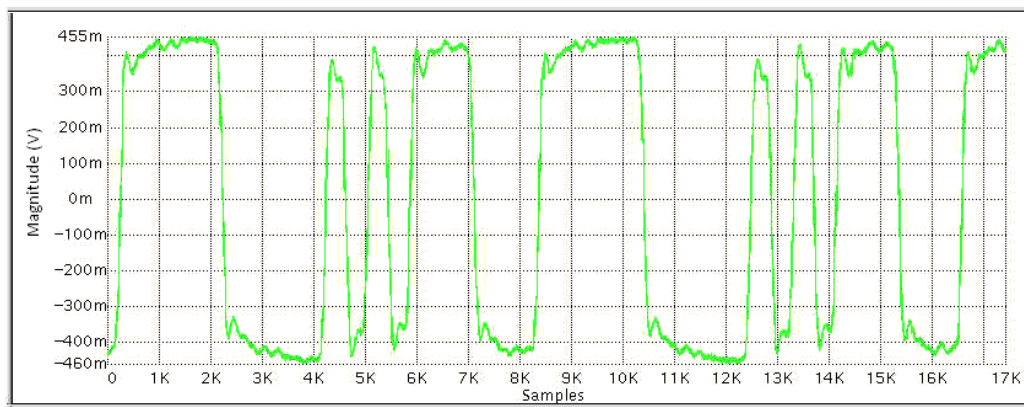


**Figure 5-10:** The transmitter output waveform after the delay line

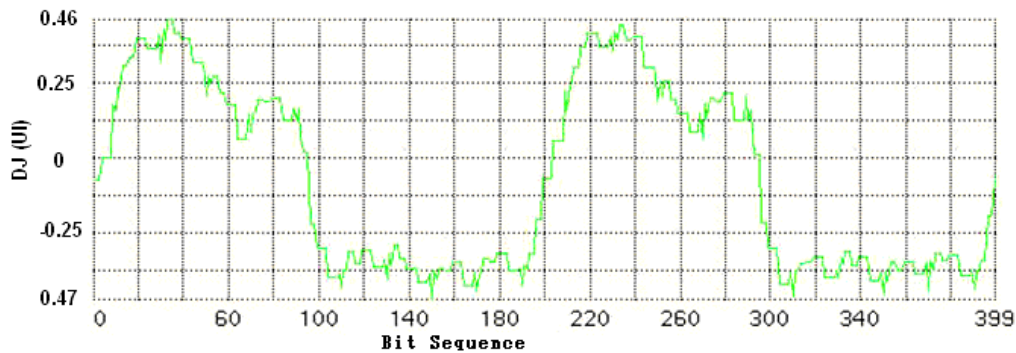


**Figure 5-11:** Extracted DJ profile from captured data signal.

Figure 5-11 plots the extracted DJ profile from the captured data signal using the transmitter jitter extraction scheme proposed in Chapter 4.3. In the 400-bit 6Gbps data signal, the DJ profile repeats twice. Therefore, the DJ dominant frequency is 30MHz. As we can see, the DJ profile is close to a square waveform, which is the profile of the jitter

source – a 30 MHz clock signal. There is a minor distortion at the second half of the high logic level, which is most likely caused by the intrinsic PJ of the device. The extracted DJ profile contains all DJ components, including the injected DJ and the device intrinsic DJ. As discussed in Chapter 4.3.4, the device also has an intrinsic PJ component at 30 MHz. This is why the DJ profile in Figure 5-11 is not exactly the same square waveform as we inject.

Figure 5-12 shows the extracted DJ values at different amplitude levels of the delay control signal. As we can see, we have an almost linear control of the injected DJ. We can calibrate the DJ and TJ of the test signal at different delay control amplitudes using either bench equipment or the digitizer on ATE. Then we can use the same jitter tolerance extrapolation algorithm presented in Chapter 3.4 to accelerate the jitter tolerance testing. The difference in the extrapolation process is that instead of varying the injected PJ to vary the TJ of the test signal discussed in Chapter 3, we vary the magnitude of the delay control to vary the TJ of the test signal in the proposed loopback testing scheme.

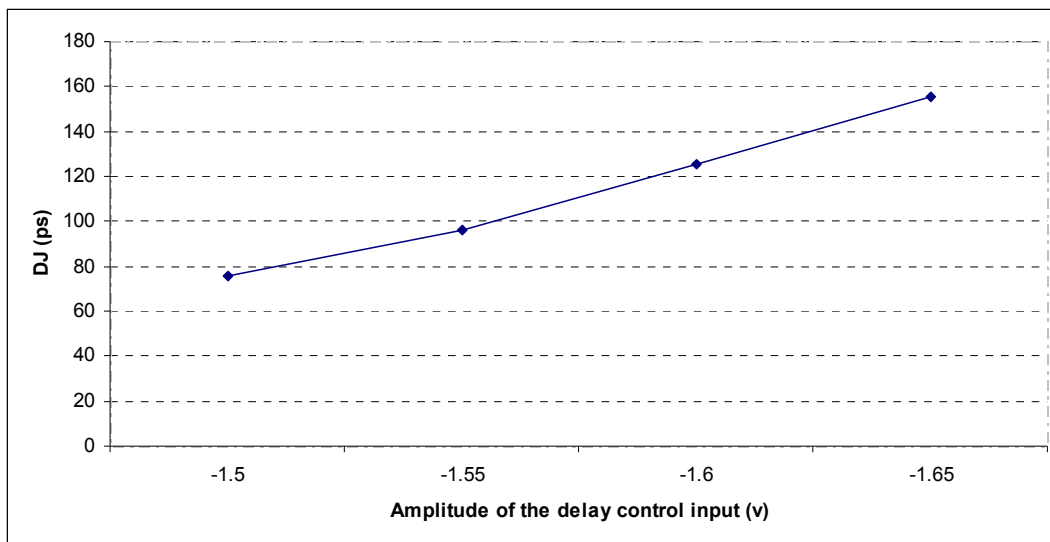


**Figure 5-12:** Extracted DJ from the phase delay output

According to Figure 5-7, the clock pattern is preferred in the test setup because it has a constant RJ degradation over a wide range of delay control amplitudes and hence can keep a constant offset between the injected DJ and TJ. However, NRZ data signals can

still be used in some applications, such as pass/fail testing, as we still can control the amount of injected TJ. Because the control is not linear for NRZ signals above 10Gbps, we cannot use NRZ signals for jitter tolerance characterization, where we need to report a jitter tolerance number as discussed in Chapter 3.4.2.

### 5.3 A Versatile HSSI Testing Scheme

In Chapter 3 and Chapter 4, we introduce ATE based HSSI test approaches. To overcome some limitations of the ATE-based solutions, we present an external loopback based testing solution using a new jitter injection technique in Chapter 5.2. By utilizing high-speed relays, we combine all the solutions in Chapters 3, 4 and 5.2, and propose a versatile scheme in this section. The scheme provides more functionality and flexibility in post-silicon validation, characterization, testing and debugging of HSSIs. Figure 5-13 shows the block diagram of the proposed scheme.

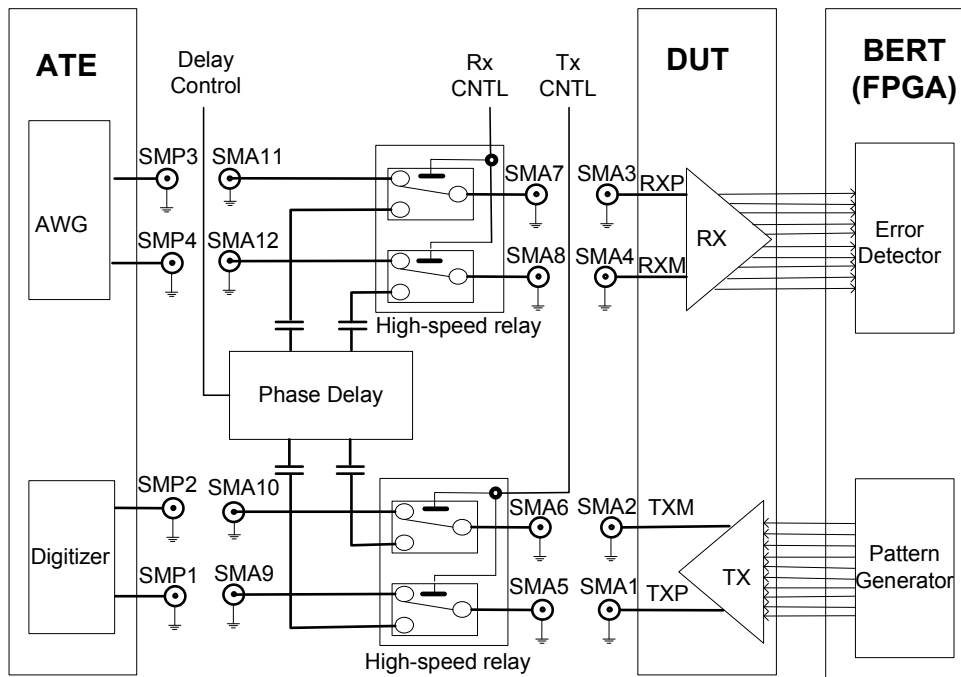


**Figure 5-13:** A versatile scheme for HSSI validation and test

### 5.3.1 Major Functions of our Setup

In Figure 5-13, the phase delay line and relays are incorporated on the testing loadboard. The relays are connected to either the phase delay line or SMA connectors. By changing the cable connections and controlling the relays, we can configure the proposed setup to realize different functions for testing, validation and debugging of HSSIs.

#### A. Testing, Validation and Debugging on ATE

In this configuration, the transmitter output is connected to the digitizer on the ATE, and the output of the AWG on the ATE is connected to the receiver input. Cables are used to:

- Connect SMA1 to SMP1, and SMA2 to SMP2
- Connect SMA3 to SMP3, and SMA4 to SMP4

This is the test setups discussed in Chapters 3 and 4. Figure 5-14 plots this test configuration. The whole HSSI functionality and most design specifications can be qualified in less than one second in production [3], [4]. In this approach, we can accurately control the parameters in the receiver test signal, such as injected jitter, amplitude and test patterns. We can also capture the transmitter output waveform and extract transmitter parameters in a few tens of milliseconds.

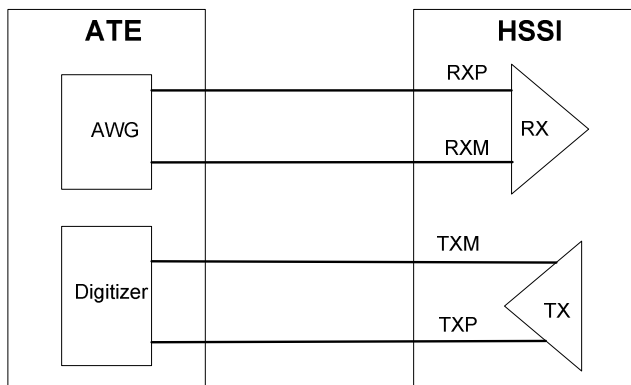


**Figure 5-14:** Testing HSSIs on ATE

The ATE-based solution can also facilitate the HSSI validation and debugging process. For example, if we find receiver jitter tolerance is too low, we can quickly debug it by

measuring the jitter tolerance at different conditions, such as varying the amplitude of the receiver input signal, changing the equalizer and PLL settings, turning on/off the transmitter block, sweeping supplying voltages, etc. All the measurement results are stored automatically and can be analyzed using ATE software. Using the ATE-based configuration, these kinds of debugging and validation procedures can be done more than 1000 times faster than traditional bench approaches [3].

## B. External Loopback with Jitter Injection

This is the test setup shown in Figure 5-4 and discussed in Chapter 5.2. In the loopback configuration, Rx CNTL and Tx CNTL are set to low (the relays switch to lower throw). Delay Control can be connected to a digital channel on ATE or another resource to control injected jitter. Cables are used to:

- Connect SMA1 to SMA5, and SMA2 to SMA6
- Connect SMA3 to SMA7, and SMA4 to SMA8

## C. Other Configurations

1) External loopback without jitter injection: the DUT transmitter output is directly connected to the input of receiver. Cables are used to connect SMA1 to SMA3, and SMA2 to SMA4. This provides a quick way to check the functionality of the HSSI.

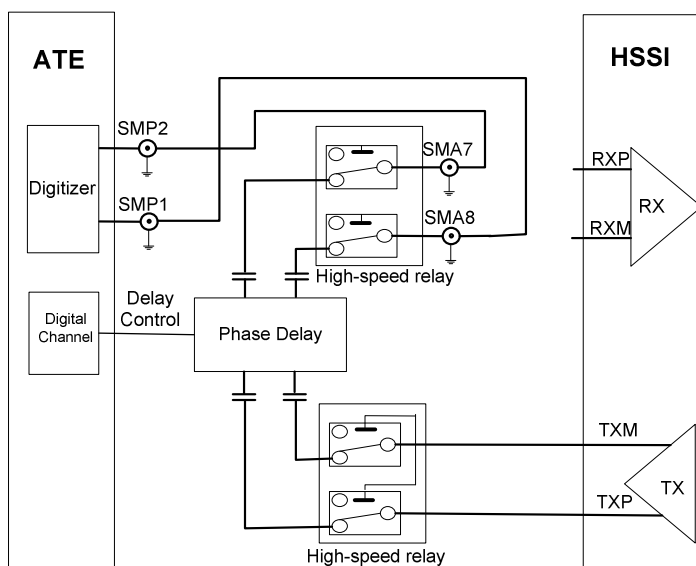


**Figure 5-15:** Characterizing the relay and the phase delay using the digitizer

- 2) Characterize Relay and Delay line using the Digitizer. The following lists the control settings and cable connections. Figure 5-15 plots the simplified connections of this configuration.
- Set Rx CNTL and Tx CNTL to low
  - Connect SMA1 to SMA5, and SMA2 to SMA6
  - Connect SMA7 to SMP2, and SMA8 to SMP1
- 3) Characterize relays only using the digitizer. The following list the control settings and cable connections. Figure 5-16 plots the connections of this configuration.
- Set Tx CNTL to high
  - Connect SMA1 to SMA5, and SMA2 to SMA6
  - Connect SMA9 to SMP1, and SMA10 to SMP2

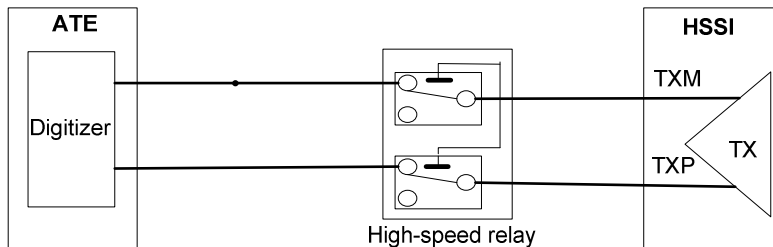


**Figure 5-16:** Characterizing the relay using the digitizer

- 4) Characterize relays only or both the relay and the delay line using external instruments: Instead of connecting to the Digitizer in 2) and 3), we can connect bench instruments to calibrate the relay and delay line.

In the above configurations, RF cables are used in order to maximize the configuration flexibility for validation, testing, debugging and calibration. This is very beneficial when we are in the debugging stage for a validation or test solution, such as evaluating the relay and the phase delay line. Once the solution is finalized, many cables can be replaced by PCB traces.

### 5.3.2 High Speed Relays

In the proposed versatile testing scheme, high-speed relays are used to switch between instruments (ATE or bench equipment) and loopback paths. When investigating signals with data rates at 6Gbps and above, it is challenging to maintain the signal integrity with relays inserted in the signal paths. One requirement for the relay is the bandwidth: it needs to be high enough to keep the signal characteristics after the signal passes through the relay.

There are a few kinds of relay technologies and each technology has its advantages and disadvantages in bandwidth, size, cost, reliability and life expectancy. A thorough survey of the relay technologies can be found in [117]. Considering we need to put the relays on the loadboard for high-speed applications, size and bandwidth are two major considerations. We concentrate our experiments on two kinds of relays: Micro-Electro-Mechanical System (MEMS) relays and electro-mechanic relays.

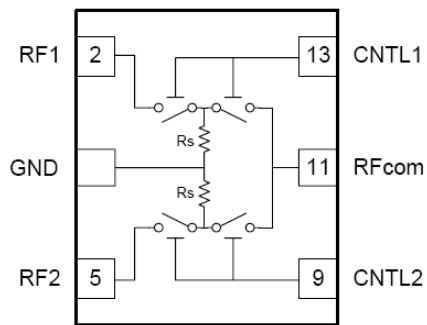


**Figure 5-17:** TT1244 functional block diagram

MEMS relays have received a lot of attention lately because of its high bandwidth and small size [118]. One disadvantage of the MEMS relays is that they are susceptible to damage from high in-rush currents or hot switching. When we started investigating the relay applications in multiple-Gigabit data applications, TeraVista was developing a new MEMS relay TT1244. This relay offers unparallel RF performance in bandwidth (DC to



26.5GHz), insertion loss, and linearity. Figure 5-17 illustrates the block diagram of the MEMS and Figure 5-18 shows its measured performance by TeraVista [119].

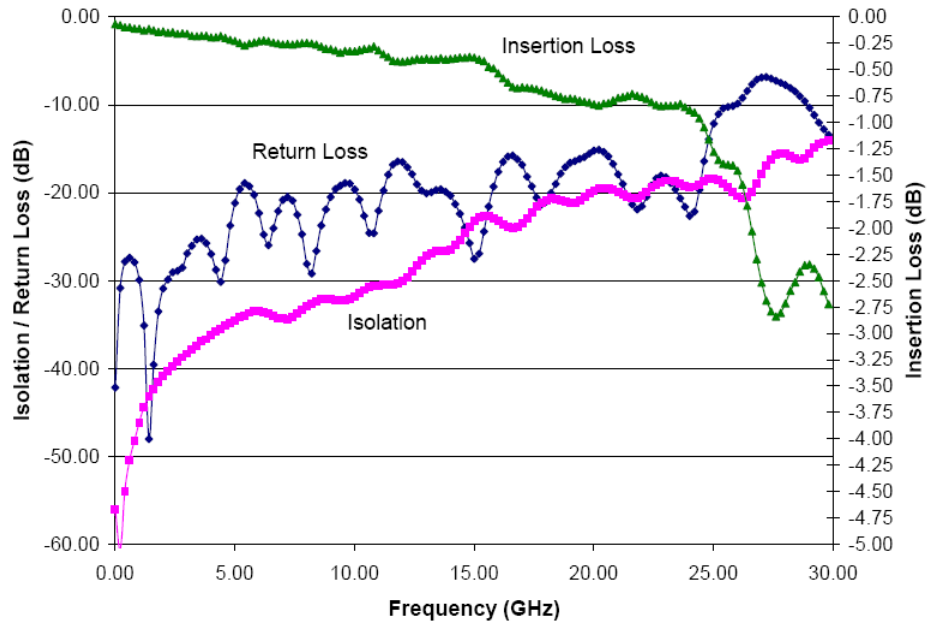


**Figure 5-18:** TT1244 measured performance by TeraVista

While the data rate of the HSSIs is continuing to increase and has reached above 10 Gbps, this switch provides the means for us to address signal integrity issues that are inherently very difficult to solve [120]. In addition, this switch has very small footprint: it is a standard surface mount micro BGA chip scale package. We therefore explored how TeraVista's DC to 26.5 GHz switches can enable us to extend our test system's capabilities and keep pace with the increased frequency requirements of our new products. While TeraVista was still developing the prototype of this switch, we developed our loadboard to include this switch and its control circuitry so we can evaluate the new product in a real ATE environment.

For MEMS switches, the control voltage is usually higher than that of other types of relays. The DC gate control voltage to CNTL1 and CNTL2 of TT1244 needs to be between 66v to 67v. Our ATE and loadboard do not have such a high voltage. Therefore, we used a charge pump to generate the high control voltage. Figure 5-19 is the charge

pump circuitry. The charge pump TT6820 only needs a power supply between 3v to 5v, which can be provided by any tester. The input signals (*In1~In6*) can come from any digital channels of the ATE or from an FPGA if no ATE instruments are available. The output signals (*CNTL1~CNTL6*) can directly control the MEME relays.

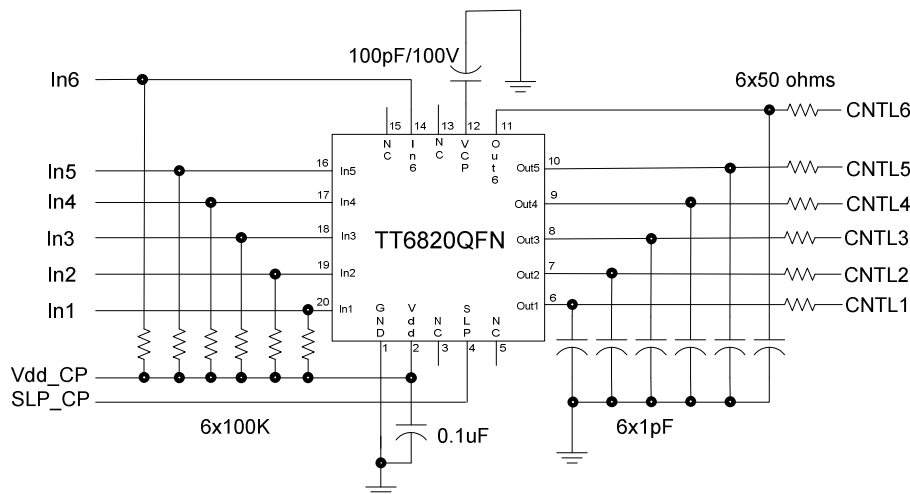


**Figure 5-19:** Charge-pump circuit for the MEMS

When the TT1244 prototype was available, we were the first user evaluating the MEMS switch on a real loadboard. We put the switch in a 6Gbps signal path and compared the signal integrity of the path to the same length signal path without a switch. We did not observe any noticeable signal integrity degradation – the switch is nearly transparent.

However, we did see some issues. The major one is the reliability. The MEMS relay worked well at the beginning, but it stopped working after a number of switching cycles. We carefully controlled our program to avoid the possible damage advised by the MEMS provider, but the MEMS relay still could get damaged. Even though the MEMS TT1244 product did not succeed, the performance it exhibited was very promising. MEMS would be a good direction to explore for applications with data rates at 10Gbps and above.

Currently, the data rate of the mainstream HSSI products is still below 10Gbps. Considering the issues in the MEMS switches and the current requirements, we choose a hermetic electro-mechanic relay, Teledyne GRF300, for HSSI product testing after

comparing performance, reliability and size [121]. Figure 5-20 shows the schematic and recommended layout [122]. The relay features a unique ground shield for each lead to ensure excellent isolation. The unique ground connection pushes the RF performance up into the 10Gbps data rates for signal integrity applications. In addition, its ultra-miniature size, high reliability and surface mount features make it a perfect choice for current HSSI testing applications.

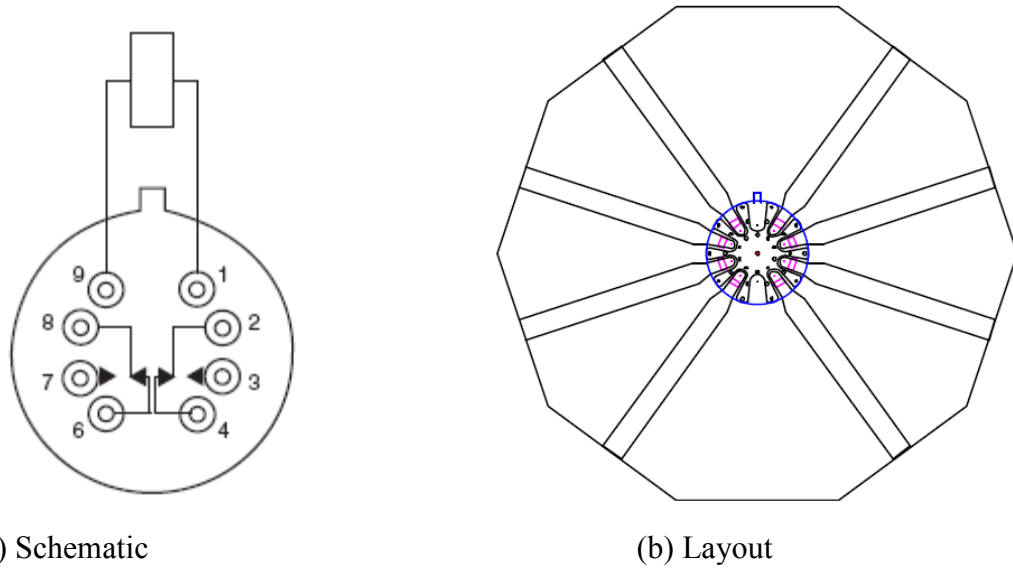


**Figure 5-20:** GRF300 relay (Courtesy of Teledyne)

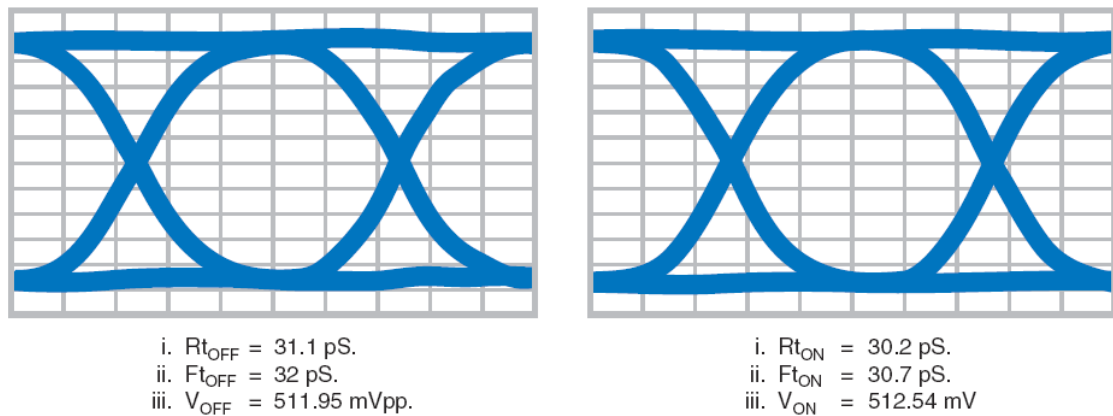


**Figure 5-21:** Typical signal integrity performance at 10Gbps (courtesy of Teledyne)

Figure 5-21 shows the typical signal integrity characteristics of GRF300 [121]. The eye diagram was captured by Teledyne using the Agilent AG86100 Digital Communication Analyzer. The data rate was set to 10Gbps and a  $2^{31}-1$  PRBS signal was used. The relay

was mounted on an evaluation board. In the measurement, two 3-foot long RF cables were used to connect the evaluation board and the analyzer. .

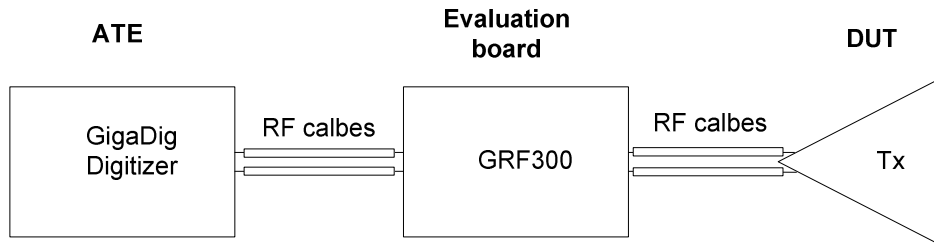
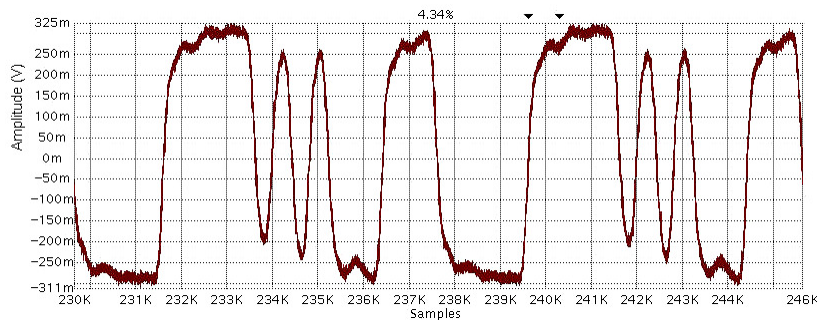
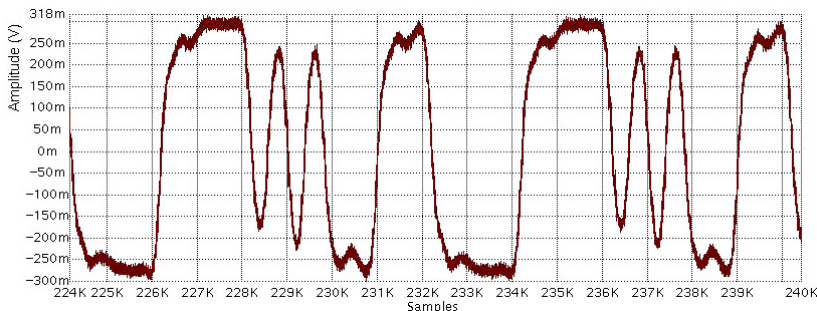


**Figure 5-22:** GRF300 relay evaluation setup.

We evaluated the signal integrity performance of the relay in our ATE environment. Figure 5-22 shows the evaluation setup. In this setup, the differential output signals of the transmitter are connected to the poles of the relay through RF cables. The signals are then routed to a Gigabit digitizer on the ATE through the relay. The digitizer is used to capture the RF signal and extract the signal integrity parameters as discussed in Chapter 4



(a) Without relay in the signal path



(b) With Relay inserted in the signal path

**Figure 5-23:** Captured waveforms on ATE

In our setup, we set the data rate of our device to its maximum – 6Gbps. We capture the waveforms of the transmitter output after it passes through different signal paths. Figure 5-23 shows the captured waveforms with the relay inserted and bypassed respectively in the signal path. Table 5-1 lists the extracted signal parameters after the transmitter output passes through different signal paths.

**Table 5-1:** 6Gbps Signal Parameters in Different Signal Paths.

Signal Path /Parameters	Original	Extra 20-inch cable	Extra 50-inch cable + Relay
Amplitude (mV)	610	595	572
Rise (ps)	60	63.4	71.2
Fall (ps)	64	66.3	75.5
DJ (ps)	11.2	19.1	21.5
RJ (ps)	1.8	1.8	1.9

As we can see, the signal still keeps similar characteristics after passing through an extra 50-inch cable and the relay compared to the signal passing through only an extra 20-inch cable. The slight rising time increase is more likely caused by the extra length cable according to the difference between the original signal and the signal passing through an extra 20-inch cable.

### 5.3.3 Limitations and Further Considerations

The proposed loopback testing scheme in this chapter removes the need for expensive high-speed ATE instruments. It is especially suitable for multiple-line HSSI testing due to its low cost. Low cost testing has always been attractive the industry [79], [99], [137]. Our scheme also overcomes the ATE instrument limitation for data rates above 6Gbps. However, there are also limitations and some special considerations need to be taken.

In the delay-line based loopback approach, one thing we need to consider is the amount of jitter that needs to be injected. In [3], we set the amount of injected jitter using a jitter extrapolation algorithm based on calibrated test signals. In the loopback approach,

because the transmitter jitter may vary from device to device, the jitter in the receiver test signal is not constant anymore even with the same amount of injected jitter. The loopback test cannot differentiate between the transmitter failure and receiver failure. To minimize the possibility of skipping bad devices or failing good devices, we need to characterize the transmitter jitter performance in order to set a proper amount of injected jitter. We can achieve a more accurate testing by using a gold device or by measuring the transmitter jitter and then setting the injected jitter accordingly. However, the test setup and the test program in both cases become complicated.

In addition, when implementing the loopback test in production, we also have to take the following into considerations:

- When multiple loadboards are used in a mass production environment, it is required to characterize the delay line to make sure that the characteristics variations of all the delay lines are within a permitted range.
- We need to calibrate the delay line on a regular basis to make sure its performance does not drift over time until the confidence to the new component is established.
- We need to characterize the delay line to get its delay control voltage vs. injected jitter relationship for each data pattern we plan to use.
- We still need to explore more sophisticated relays, such as MEMS for data rates above 10Gbps to minimize the signal integrity degradation.

For the FPGA-based bit error detection scheme discussed in Chapter 5.1, one drawback is that an FPGA device or board is needed if the current board does not have one. However, the FPGA can provide more testing power than just acting as a BERT. The BERT only takes a small portion of the FPGA resources [6]. We can implement new testing or reduce the cost of the current testing solutions using the remaining FPGA resources.

## **5.4 BER Testing Under Noise**

In the jitter tolerance testing, we stress the receiver using signals with controllable amounts of injected jitter. We accelerate the qualification of the jitter tolerance

characteristics at  $10^{-12}$  BER level by evaluating it at higher BER levels. Similar to the jitter tolerance testing, we stress the system with controllable amounts of amplitude noise to test the BER performance under noise conditions. In jitter tolerance testing, one challenge is how to inject controllable amounts of jitter to the test signals. For BER testing under noise, the challenge becomes developing a noise generator with performance that meets test requirements. In this section, we present the implementation details of our AWGN generator, an application example in accelerating BER evaluation and the advantages of our generator.

## 5.4.1 Our AWGN Generator

### 5.4.1.1 Hardware Implementation

We implement our AWGN generator based on Polar Method [65], which is explained in Algorithm 2 in Chapter 2.3.3. The block diagram of the Polar method for two AWGN generators is developed and shown in Figure 5-24. It can easily be simplified to a single generator. We use eight independent LFSRs to generate two 4-bit uniformly distributed random variables,  $U_1$  and  $U_2$ . All bits represent fractions, so  $U_1$  and  $U_2$  are uniformly distributed over  $[0, 0.9375]$ . The number inside the LFSR represents its length.  $V_1$  and  $V_2$  are generated using signed adders. As computing  $S$  involves lots of additions and multiplications, we use a ROM-based design, where the concatenation of  $U_1$  and  $U_2$  is set to be the address and  $S$  is set to be the data stored in the ROM. If computed  $S \geq 1$ , zero is stored in the ROM.

As the Polar method does throw out some data, the Do Loop runs faster than line 7 and line 8 in Algorithm 2. We insert a synchronizing FIFO to achieve a constant output rate. Two clock signals are used in the FIFO,  $clk1$  for writing and  $clk2$  for reading. Writing is enabled when  $S$  is not equal to 0, while reading is always enabled. The LFSRs are disabled when the FIFO is full. The FIFO is 20 bits in width. By setting the depth of the FIFO to be 16 and  $clk2$  to be half of  $clk1$ , we achieve a constant output rate.

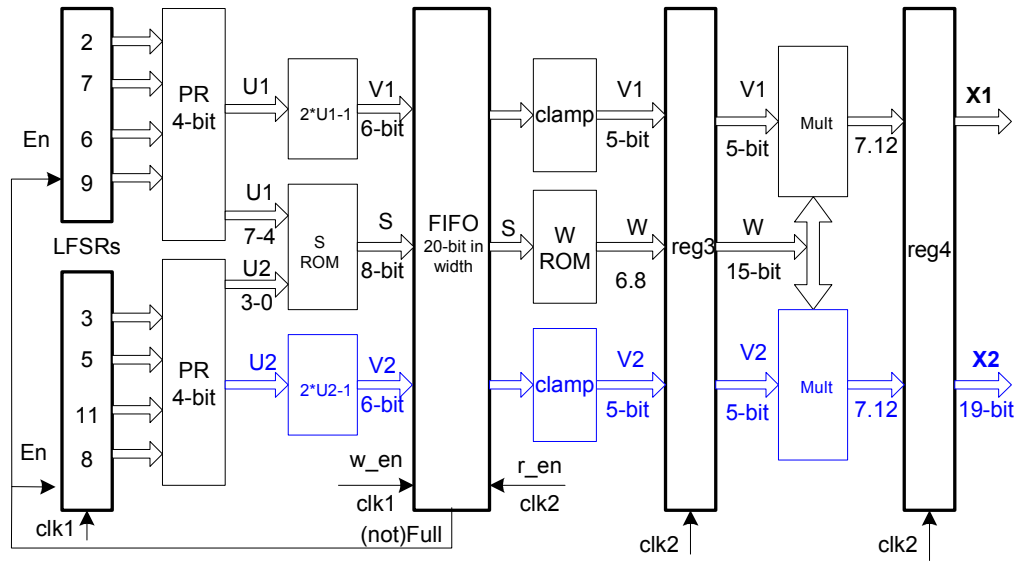


**Figure 5-24:** Block diagram of the Polar method

We also use a ROM-based design to calculate  $W$ , where  $S$  denotes the address and  $W$  denotes the data stored in the ROM. As  $S$  is between  $[0.00390625, 0.99609375]$ ,  $W$  is between  $[53.2835, 0.0886]$ , which can be denoted using 6 bits for the integer part and 8 bits for the fractional part (6.8). Finally, two signed multipliers are used to generate two Gaussian variables,  $X_1$  and  $X_2$ . Each variable is 19 bits in width: 7 bits for sign and integer, and 12 bits for fraction (7.12). The width can be truncated according to applications.

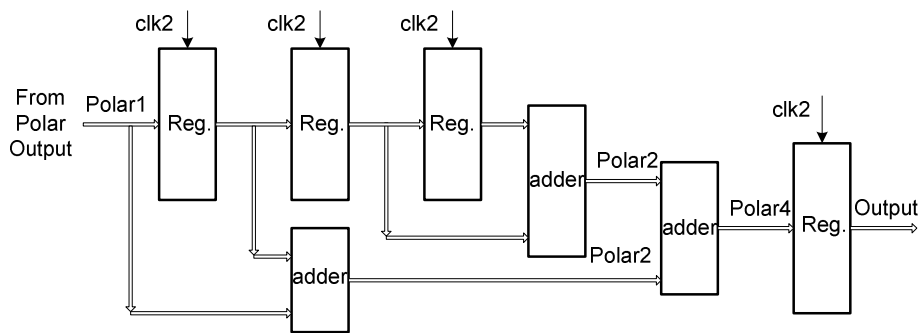


**Figure 5-25:** Our CLT method ( $N=4$ )

We use our CTL method to further improve the performance of our noise generator. Traditionally, the CLT method employs an accumulator, which slows down the output



speed by a factor of  $N$ , where  $N$  is the number of accumulated variables [47]. We propose our CLT method, shown in Figure 5-25, which does not exhibit the speed penalty while improving accuracy. Instead of accumulating data in one stage, the pipelined architecture takes data from previous stages and hence can output data every clock cycle.

#### 5.4.1.2 Statistical Properties

There are a few methods that are used to analyze the statistical properties of a noise generator. The chi-square test and the Anderson-Darling (A-D) test are two goodness-of-fit tests adopted to evaluate some emulators [123], [124], [63]. For the chi-square test, the axis is first quantized into segments. Then the actual number and expected number of samples appearing in each segment are determined. Based on the numbers of the samples, a single number is derived to serve as an overall quality metric of the generator. The chi-square test essentially compares the measured histogram to the theoretical histogram. The A-D test concentrates more on the continuous properties of a generator. It is a modification of Kolmogorov-Smirnov (K-S) test and gives more weight to the tails than the K-S test does [125]. Other statistical methods include calculating  $Q(x)$  and Kurtosis values.

The implementation of our AWGN generator is almost a direct map of the Polar algorithm without any partition or weighting [6]. Because the Polar algorithm has been widely accepted for Gaussian variable generation, the statistics properties of our generator should be favorable. Nevertheless, for property evaluation, we explore the  $Q(x)$  values and the *Kurtosis* value.

Statistical properties of an AWGN generator should be based on evaluating samples from at least one period of the generator. The period of our generator may reach  $2^N$ , where  $N$  is the sum of the lengths of all LFSRs shown in Figure 5-24. Even though the lengths of the LFSRs in Figure 5-24 are very short, the sum  $N$  reaches 51. Statistically evaluating  $2^{51}$  samples requires a lot of hardware resources and time. We show next that the statistical results of thousands of samples are a good approximation. We first evaluate the  $Q$  factor

accuracy of our AWGN generator, which is very important for BER testing and can easily be tested. Table 5-2 shows the  $Q(x)$  accuracy of our generators with 10,000 and 500,000 samples. The samples are taken from a simulator, and then passed to a UNIX workstation to do statistical analysis. Even for the 500,000 samples, it takes the workstation a whole night to finish the evaluation.

**Table 5-2:**  $Q(x)$  Relative Error of Our Generators

$x$	Theory $Q(x)$	Relative Error of Our AWGN Generators		
		Figure 5-24 10,000 Samples	Figure 5-24 + Figure 5-25	
			10,000	500,000
0	0.5000	2.76 %	1.02 %	0.24%
0.2	0.4207	-2.50 %	0.50 %	0.42%
0.4	0.3446	1.69 %	0.26 %	0.55%
0.6	0.2743	-0.10 %	1.06 %	0.80%
0.8	0.2119	1.88 %	1.74 %	1.09%
1.0	0.1587	4.70 %	3.21 %	1.20%
1.2	0.1151	-7.17 %	3.99 %	1.49%
1.4	0.0808	-4.29 %	4.95 %	1.85%
1.6	0.0548	-3.06 %	6.57 %	2.37%

We can see that our method with the parameters shown in Figure 5-24 (simplified to a single generator) implements a high precision AWGN generator. Our CLT method shown in Figure 5-25 can further reduce the variation of the distribution. Also note that the relative error of  $Q(x)$  decreases when the number of samples increases. The limited number of samples is the main reason for the error.

*Kurtosis* is also used to evaluate the Gaussian distribution [126], [127]. It is a measure of the flatness or peakedness of the probability distribution of a real-valued random variable. The *Kurtosis* value is often defined as the fourth standardized moment. For a sample of  $n$  values, the sample *Kurtosis* is

$$g_2 = \frac{m_4}{m_2^2}$$

$$= \frac{\frac{1}{n} \sum_{i=1}^n (x_i - m)^4}{\left(\frac{1}{n} \sum_{i=1}^n (x_i - m)^2\right)^2}$$

Where  $m_4$  is the fourth sample moment above mean  $m$ ,  $m_2$  is the second sample moment (variance),  $x_i$  is the  $i^{\text{th}}$  value and  $m$  is the sample mean [128].

The *Kurtosis* value of an idea Normal distribution is 3. A *Kurtosis* value greater than 3 indicates that the distribution has a sharper peak and fatter tails, and the distribution is leptokurtic. If the *Kurtosis* value is less than 3, the distribution has a more rounded peak and thinner tails, and the distribution is platykurtic. Based on the 500,000 samples from the output of our AWGN generator, we calculated a Kurtosis value of 2.95, which is less than 2 percent off the theoretical value.

### 5.4.2 BER Testing Demonstration

To test the BER under noise conditions, an AWGN generator with a variable gain is used to emulate an AWGN communication channel. The output of the variable gain AWGN generator is added to the output of the transmitter. The composed signal is then sent to the input of the receiver. We can use a BERT to generate test signals and compare recovered errors. Figure 5-26 shows the setup.

In the test setup, the BERT can be a general purpose testing instrument that many companies provide [55], [56]. We can also use the FPGA-based BERT we present in Chapter 5.1. The DUT can be any communication interface or system that receives bit or word sequences and then restores the sequences after some signal processing or format changes. Some DUT examples include an HSSI and the integration of an encoder and a decoder.

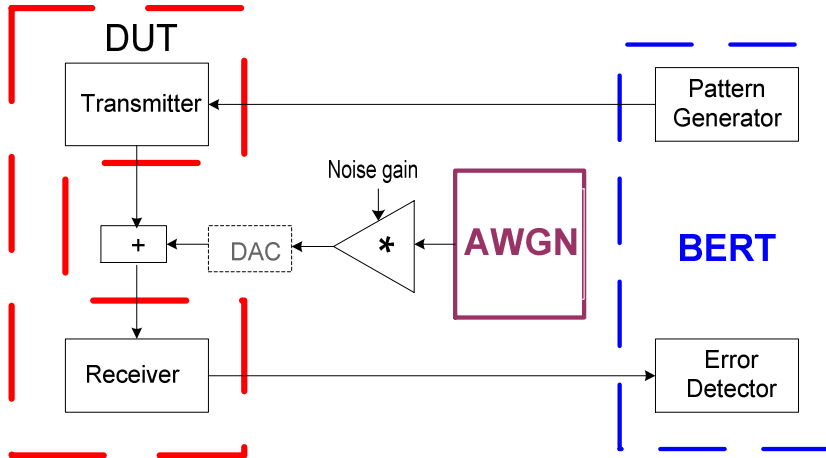


**Figure 5-26:** Setup of testing BER under noise

The amplitude of the AWGN generator is programmable. Hence, we can emulate an AWGN channel in which signals are transmitted with different SNRs. The proposed setup can be used to test the BER performance of a real DUT in real operations under different SNR conditions. Because the output of our AWGN is digital, a Digital-to-Analog Converter (DAC) is needed if the AWGN output is added to an analog data signal. If the data signal is digital, the DAC is not needed.

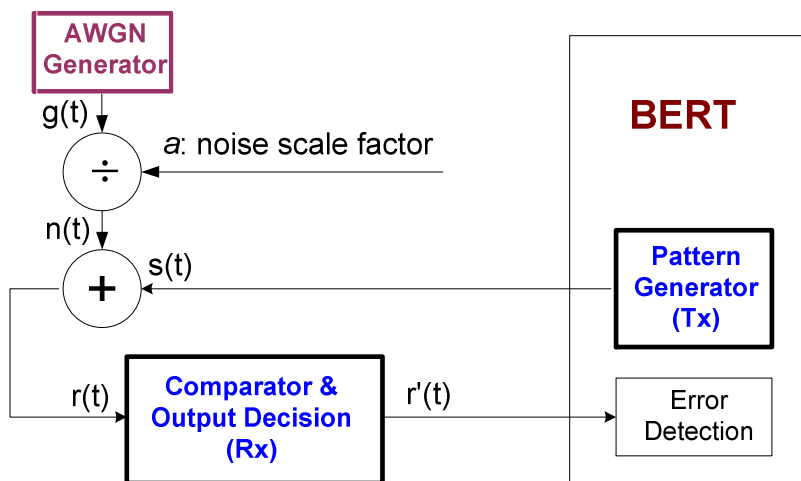


**Figure 5-27:** BER testing setup for digital baseband transmission

Figure 5-27 demonstrates the application of our AWGN generator in BER testing for digital baseband, where no DAC is needed. In a digital baseband communication system,

one is used to transmit data ‘1’ and zero is used to transmit data ‘0’. The BER and SNR are related according to Equation (2-11)

$$BER = Q\sqrt{SNR}$$

Assuming that data 1s and 0s have equal probability of occurrence in this digital baseband system, the average energy of the transmitted signals  $s(t)$  is

$$E = (E_0 + E_1) / 2 = 0.5 .$$

In the testing setup, the AWGN Generator has zero mean and unity standard deviation. The generator output is scaled by the noise scale factor  $a$ . In this case, the energy of the noise  $n(t)$  is

$$N_o = 2 / a^2 .$$

As a result, we have

$$SNR = E / N_o = a^2 / 4 \quad (5-2)$$

**Table 5-3:** BER Measurements for Digital Baseband

$a$	SNR (dB)	Total bits	Our BER	Agilent BER	Error (%)
2	0.6	2024	1.62e-1	1.65e-1	1.85
3	4.1	12448	6.58e-2	6.61e-2	0.45
4	6.6	12448	2.32e-2	2.40e-2	3.33
5	8.5	20000	5.65e-3	5.32e-3	4.32
6	10.1	1000000	1.20e-3	1.31e-3	8.40
7	11.5	1000000	1.76e-4	1.83e-4	3.83
8	12.6	10000000	1.62e-5	1.78e-5	8.99

As shown in Figure 5-27, the Pattern Generator, which also serves as the transmitter, sends out a digital baseband data signal  $s(t)$ , and the data signal is corrupted by the noise signal  $n(t)$ . Then the noise corrupted data signal  $r(t)$  is sent to the input of the receiver. The receiver is actually a comparator, which decides whether the received bit is 1 or 0. If the noise corrupted signal  $r(t)$  is bigger than the threshold voltage (0.5 in this case),  $r'(t)$  is set to 1; otherwise,  $r'(t)$  is 0. Table 5-3 lists the BER results at different noise scale

factors. The measurements were taken while running the testing setup on an Altera Mercury FPGA board. The measurement was first done using our BERT, and then an Agilent BERT.

Figure 5-28 shows the plot of the theoretical BER, the measured BERs using our BERT and an Agilent 81200 BERT as a function of input SNR.

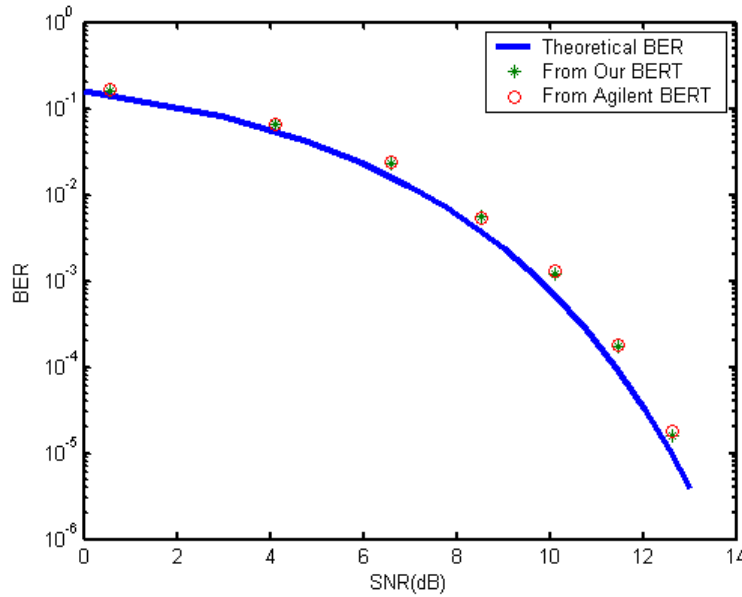


**Figure 5-28:** Measured BER vs. theoretical BER

As indicated in Figure 5-28, the measured BER using our BERT perfectly coincides with that from the expensive Agilent BERT, and is close to the theoretical BER. The plot demonstrates the validity of the AWGN generator and the testing scheme. In the testing setup, the pattern is generated using an LFSR, which produces more 1s than 0s, as all zeros is not a valid pattern while all ones is. Therefore, the actual signal energy is bigger than the theoretical value 0.5; for example, if the length of the LFSR is 3, the signal energy it produces is 4/7. We take this factor into consideration when calculating the SNRs in Table 5-3.

In the above testing, it takes less than one second to generate the point at  $1.62 \times 10^{-5}$  BER, while software simulations take hours. Furthermore, regardless of the noise generation

scheme, going down to low error rates requires many samples just to exhibit errors - for  $10^{-12}$  BER at 1 Gbps data rate, it takes three hours (assuming running  $10^{13}$  bits). In production, the normal practice to qualify the BER performance at such low levels is through extrapolation [2]. However, if direct BER measurements at  $10^{-12}$  or lower are needed, our AWGN is a good candidate as we will discuss in the next section.

Although the above experiment is based on testing a digital baseband system, the proposed BER testing scheme can be applied to other AWGN transmission system. Depending on the modulation scheme of the system, other components, such as a digital-to-analog convertor and an attenuator, might be needed. Furthermore, the AWGN module can be modified to emulate more complex channels, such as Rayleigh channels.

### 5.4.3 Advantages of Our AWGN Generator

For the AWGN generator we developed and discussed in Chapter 5.4.1, there are a few advantages compared to other implementations. The prominent advantage is its large maximum output value. Theoretically, the tail of an AWGN distribution should extend towards infinity and the maximum output value is infinity. In reality, it is impossible to generate an infinity number. For an AWGN emulator, the tail is bounded by its maximum output value  $m$ .

Most existing standalone AWGN emulators are based on the Box-Muller Algorithm introduced in Chapter 2.3.3, which is difficult to achieve a large maximum output value. Utilizing the Box-Muller method presented in [47], a commercial AWGN core has been developed [60]. This core is only capable of generating a maximum  $m$  value of 4.7. Two years later, Lee et al. advanced the Box-Muller method [61] and increased the maximum  $m$  value to 6.7. This improved a bit the tail distribution of the AWGN generator. However, the price paid for this improvement is in quadrupled hardware resources, while the speed is halved. In 2005, this value was increased to 8.2 by using sophisticated FPGAs and implementation techniques [129]. The most recent advance in implementing AWGN generators in FPGAs based on the Box-Muller Algorithm is presented by

Alimohammad *et al.* from University of Alberta in [63], where the tail distribution is extended to  $\pm 15$  times of the standard deviation  $\delta$ . The paper [63] also gives a comprehensive overview of Gaussian noise generation algorithms and related work on implementing the generators in hardware.

As a key advantage, the Polar method we developed can easily achieve high maximum output values with little hardware. As indicated in Algorithm 2 in Chapter 2.3.3, the maximum output value is calculated as a logarithm of the minimum value of the square operation of the random variables  $U_1$  and  $U_2$ . In contrast, the Box-Muller method calculates a logarithm of the random variable  $x_1$  directly as shown in Algorithm 1, which requires a tremendous amount of hardware to achieve a big output value. In our implementation, we can produce a maximum output value of 53.3 by using only 4 bits (all for the fraction) to represent each uniform random variable ( $U_1$  and  $U_2$  in Algorithm 2). To achieve such a high maximum output value using the Box-Muller method, we need to use more than 1000 bits to represent the uniform random variable  $x_1$  in Algorithm 1, which is almost impossible to implement in hardware.

A noise generator with a large maximum output value is essential for low BER evaluation. According to Equation (2-11), the BER and SNR are linked by Q factor:

$$BER = Q(\sqrt{SNR})$$

Therefore, low BERs require high SNRs. In an AWGN communication system, the SNR is determined by the standard deviation  $\delta$  of the AWGN generator when the output of the generator is added to a data signal with constant energy. In order to emulate a low BER system, we usually scale down the distribution of the Gaussian generator to achieve a low standard deviation. However, some samples of the noise generator output must be large enough to produce bit errors. The lowest BER that an AWGN generator can emulate is determined by the tail distribution of the AWGN generator, or more specifically limited by the maximum output value  $m$  of the noise variable. For a digital system where data “0” and data “1” are transmitted, the maximum output of the noise generator is required to be bigger than the threshold (usually 0.5) in order to generate bit errors.



Most existing hardware AWGN generators (e.g., [47], [60], [61] and [62]) only have a maximum output value of 7. If we use such generators in baseband transmission evaluation, they can only generate a theoretical maximum SNR of 16.9dB by being scaled by a factor of 14 (the noise scale factor  $a$ ) according to Equation 5-2. The 16.9dB SNR can be translated into a BER around  $10^{-12}$  according to Equation (2-11), but such generators are only suitable for exploring channel behavior at BERs down to the range of  $10^{-9}$  to  $10^{-10}$  [61]. For any AWGN generator with bounded output, the distribution near its maximum output value is not Gaussian anymore and cannot be used because ideal Gaussian distribution is unbounded (the maximum output value is infinity). Hence, the tail distribution of these AWGN generators needs to be improved for applications with low BERs, such as  $10^{-12}$ .

The latest AWGN generator presented in [63] can generate a maximum output value of 15. The generator is capable of evaluating BERs below  $10^{-12}$ . Our AWGN generator further increases the maximum output value to 53.3. Therefore, our AWGN generator is a good candidate for very low BER applications.

Besides the maximum output value, another advantage of our AWGN generators is that it is highly scalable. In the implementation discussed in Chapter 5.4.1.1, we only use 4 bits to represent the uniformly distributed random variables. The lengths of the LFSRs used to generate each bit are also short. They can be easily increased to achieve better performance if needed. In addition, our noise generator is relatively straightforward to implement. One challenge of the Polar method implementation is to convert the variable output rate to a constant output rate. We resolve it by inserting a dual clock FIFO. Other function implementation is almost a direct map to Algorithm 2 – no further partition, rounding or approximation is needed.

---

# Chapter 6 – Conclusions and Future Work

---

## 6.1 Conclusions

This thesis has presented schemes that can accelerate the qualifications of jitter characteristics and BER performance for HSSIs. We have developed a systematic ATE solution for the characterization and compliance qualification of receiver jitter tolerance and transmitter output jitter.

For the receiver jitter tolerance testing, we propose a jitter tolerance extrapolation algorithm, capable of accelerating jitter tolerance testing >1000 times. This makes it possible to run the time-consuming jitter tolerance test in production. The test signal is generated by the AWG on ATE. The BER can be monitored either by digital channels on ATE or by BIST circuitry. The approach does not need any add-on modules. Based on the AWG6000, we conduct jitter tolerance testing investigation on 1.5Gbps and 3Gbps signals. Higher speed applications are attainable using a higher performance AWG.

For transmitter jitter testing, we have proposed three approaches to extract jitter components. With the proposed approaches, we manage to have the whole transmitter test done within 100ms and achieve a jitter accuracy within  $\pm 0.5$ ps (run-to-run variation, and the difference between bench and ATE measurement results), which no one else has ever achieved, to the best of our knowledge. Extensive experiments have been done on 3Gbps and 6Gbps signals to verify the accuracy and test repeatability. Based on a high-

bandwidth digitizer available on ATE, the solution does not need any add-on circuitry. The methodology can be applied to test any HSSI transmitter.

Even though the thesis only addresses the transmitter jitter testing and receiver jitter tolerance testing, other HSSI tests are either simply by-products of the two tests or very straightforward to conduct. For most other transmitter related tests, they can directly be done based on the captured transmitter waveform. For example, the transmitter function can be verified by comparing the captured values to expected values; the transmitter level can be obtained by checking the captured level difference between 00000 and 11111, and the rise/fall time can be obtained from any edge with a full swing (low transition density areas). In addition, we can easily add more captured samples to test other transmitter functions/parameters, such as transmitter Output Enabled (OE), common mode level and pre-emphasis.

The receiver jitter tolerance test actually also covers the receiver function. If the receiver does not function, we could not get any jitter tolerance data. Other receiver parameter tests can be done using the same test setup with some minor adjustments. For example, for the receiver tracking range test, we only need to adjust the sampling frequency of the AWG to source a signal with a frequency offset that we need; for the Out of Band (OOB) test, we only need to change the AWG pattern and amplitude for different turn-on/turn-off level settings.

The whole transmitter and receiver testing solution can be used to test any HSSI devices. It is independent of the detailed structure of the device to be tested. In addition, the proposed solution is highly scalable. The scheme applies to any speed. Its application is only limited by the performance of the ATE instrument. Higher speed applications (such as 10Gbps) are attainable in the future with the advance in ATE instrument.

The proposed ATE approaches have been successfully used in production to test millions of devices. They also have been used for the validation of new designs to quickly find design issues and search for the worst case devices across PVT corners. With the

approaches, we have provided a lot of invaluable characterization data within very short time. All these are impossible to achieve by just relying on bench work. Our work has made the ATE play a more and more important role in validation and characterization besides its traditional role in production testing.

We also propose non-ATE based HSSI jitter qualification solutions. Using the state-of-the-art phase delay lines, we can inject controllable amounts of jitter to test HSSIs with data rates up to 12.5 Gbps. The low cost solution not only eliminates the need for expensive high-speed ATE instruments, it also meets the test need for applications with data rates above 6Gbps where no ATE instruments are available. In addition, we also present FPGA-based BERTs that can be used to check the bit errors and verify the functionality of HSSIs.

Finally, we also investigate the amplitude noise impact to BER. Further studies on the digital AWGN generator that we previously proposed suggest excellent properties of our noise generator.

## **6.2 Future Investigations**

### **6.2.1 PLL and CDR Characteristics Analysis**

In the jitter tolerance testing experiments discussed in Chapter 3, we demonstrate injecting PJ at a single frequency to investigate the receiver jitter tolerance. We can extend our experiments to investigate the characteristics of the PLL and CDR by applying test signals with different jitter frequencies. One example is to investigate the jitter transfer characteristics. As we discuss in Chapter 2.1.2, the jitter tolerance performance of a CDR is mainly determined by the PLL. The PLL has low-pass characteristics as shown in Figure 2-6: the recovered clock can track the in band jitter in the input data, but cannot track the out-of-band jitter. We can perform the PLL jitter transfer characterization on ATE using the test signals we generated. Figure 6-1 shows the test setup.

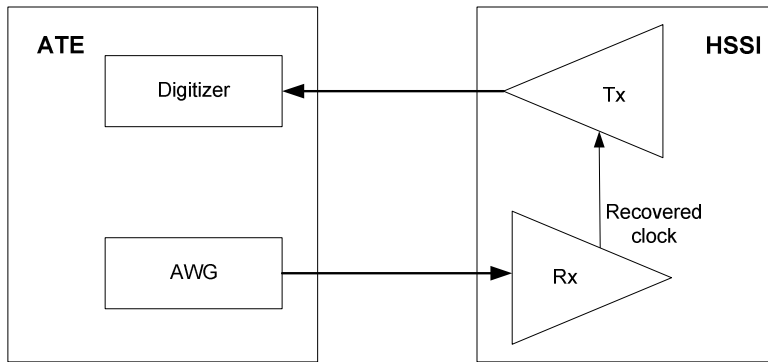


**Figure 6-1:** Test setup for the PLL jitter transfer characterization

In the test setup, the AWG sources test signals to the receiver input. The test signals from the AWG have a known constant amount of injected PJ. The receiver recovered clock is used by the transmitter to align its output. A digitizer on the ATE is used to capture the PJ in the transmitter output. The PLL jitter transfer function can be derived by sweeping the injected PJ frequencies and then comparing the injected PJ in the AWG with the captured PJ from the transmitter output. Figure 6-2 shows an example of the PLL jitter transfer experimental result, where the normalized transmitter output jitter is the ratio of the transmitter output PJ to the receiver input PJ.

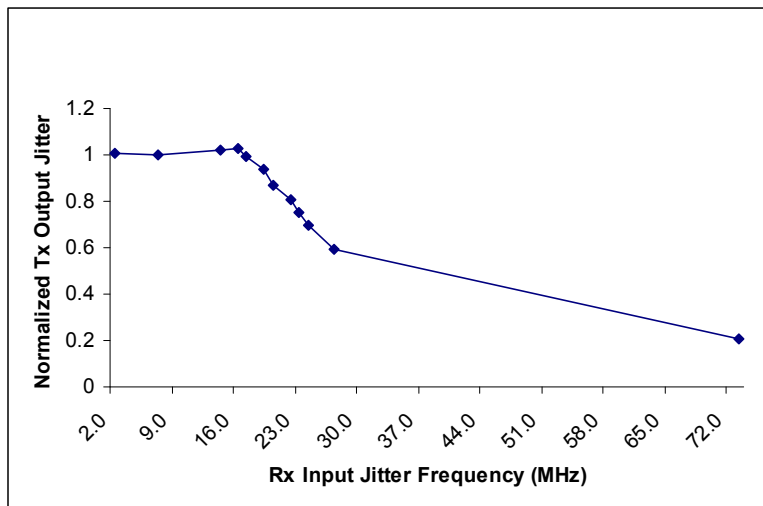


**Figure 6-2:** Measured PLL jitter transfer characteristics

As we can see from the plot, when the frequency of the receiver input jitter is below the receiver PLL bandwidth, which is around 20MHz in the above example, the transmitter

output jitter tracks the receiver input jitter. This is because the receiver recovered clock tracks the jitter in the AWG signals and therefore passes the injected jitter to the transmitter output. When the jitter frequencies are above the PLL bandwidth, the receiver recovered clock cannot track the injected jitter. Therefore the out-of-band jitter gets attenuated at the transmitter output.

Another example is to study the jitter tolerance frequency characteristics of the CDR. Figure 6-3 is an example of the frequency response of a CDR we obtained. As we can see, the frequency response is not flat. It has higher jitter tolerance at low frequencies. When the frequency increases, the jitter tolerance decreases and reaches to a minimum around 50MHz. This type of frequency sensitivity investigation is extremely time-consuming with traditional jitter tolerance test methods. It takes days to accurately characterize a device using traditional techniques. Our proposed accelerated jitter tolerance test scheme can significantly reduce the time needed for this type of characterization.

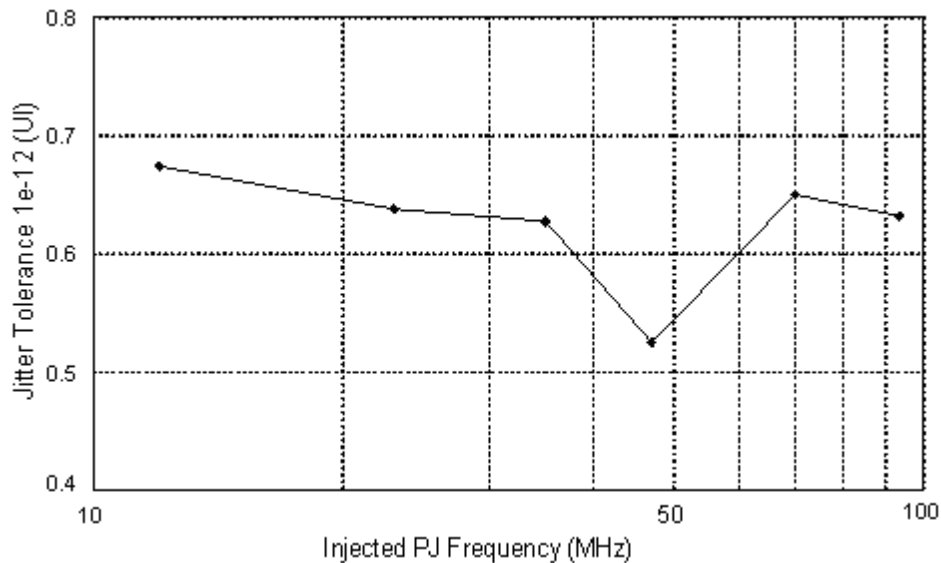


**Figure 6-3:** Jitter tolerance frequency response

In addition, our proposed scheme provides a method to develop CDR models. From the testing point of view, the CDR is just a black box. With our scheme, we can easily stress

the CDR using test signals with different frequencies and jitter profiles and check its response. Based on this kind of experiments, it is possible to make an accurate CDR model, through which the performance of the CDR can be predicted. For example, for the jitter tolerance frequency response shown in Figure 6-3, it shows a low-pass characteristic when the jitter frequency is below 50MHz. This is understandable according to the CDR characteristics discussed in Chapter 2.1.2. However, it is not intuitive why the jitter tolerance gets better at 70MHz. Further investigation is needed to understand the overall CDR behavior. The proposed scheme can speed up this kind of investigations.

### **6.2.2 Further Phase Delay Line Performance Evaluation**

In Chapter 5.2, we present an external loopback testing scheme, where the jitter is injected through a new phase delay line. According to the datasheet [116], the delay line offers unparallel delay control bandwidth and data bandwidth, suitable for injecting jitter to test HSSIs with data rates up to 12.5GHz. We evaluate the performance using a 6Gbps data signal with 30MHz injected jitter. The experimental result shows a linear relationship between the injected DJ and the delay control amplitude, which is what we expected. However, the performance at higher data rates (up to 12.5Gbps) and higher jitter frequencies (up to 1G) have not been evaluated. We need to evaluate them when the signal generator is available to generate the high speed data signal.

In addition, we still need to calibrate the relationship between the TJ and the delay control amplitude in order to apply the scheme to the final production. According to the datasheet, the RJ degradation is constant for clock signals. We should be able to transfer the linear relationship between the injected DJ and the delay control amplitude to a linear relationship between the TJ and the delay control amplitude. Theoretically we can use the same jitter extrapolation algorithm as discussed in Chapter 3.4 and it should generate similar extrapolation accuracy. However, these predictions have not been verified.

### 6.2.3 AWGN Generator Implementation

In Chapter 5.4, we present the great advantage of our method in implementing Gaussian noise generators for low BER evaluation. We evaluate the  $Q(x)$  performance of our generator with 500,000 samples, but the distribution around its tail has not been fully evaluated mainly because of the limited computing hardware resources. We need to take a much bigger number of samples. Analyzing the data requires a lot of hardware resources and is extremely time-consuming. The shortage of manpower is also another reason -- this research concentrates more on jitter qualifications.

The full advantages of implementing Gaussian noise generators using our method still need to be explored. The performance of our generators can be further improved from several directions:

- Improve the tail distribution by increasing the number of bits used to represent the uniformly distributed random numbers.
- Achieve better randomness by increasing the length of the LFSRs
- Increase the throughput by using higher performance FPGAs



---

# References

---

- [1] Y. Fan and Z. Zilic, "Qualifying Serial Interface Jitter Rapidly and Cost-effectively," *Springer Journal of Electronic Testing: Theory and Applications*, Volume 26, 2010, 17 pages, DOI: 10.1007/s10836-009-5131-5
- [2] Y. Fan, Y. Cai, L. Fang, A. Verma, B. Burcanowski, Z. Zilic and S. Kumar, "An Accelerated Jitter Tolerance Test Technique on ATE for 1.5GG/s and 3GB/s Serial-ATA," *Proceedings of IEEE International Test Conference*, Oct. 2006
- [3] Y. Fan and Z. Zilic "Accelerating Jitter Tolerance Qualification for High Speed Serial Interfaces," *Proceedings of the 10th International Symposium on Quality Electronic Design*, ISQED'09, March. 2009
- [4] Y. Fan, Y. Cai and Z. Zilic, "A High Accuracy, High Throughput Jitter Test Solution on ATE for 3 Gbps and 6 Gbps Serial-ATA," *Proceedings of IEEE International Test Conference*, Oct. 2007
- [5] Y. Fan and Z. Zilic, "A Versatile Scheme for Validation, Testing and Debugging of High Speed Serial Interfaces," *Proceedings of IEEE High Level Design Validation and Test Workshop*, HLDVT'09, Nov. 2009
- [6] Y. Fan and Z. Zilic, "Bit Error Rate Testing of Communication Interfaces," *IEEE Transactions on Instrumentation and Measurements*, Vol. 57, No. 5, pp. 897-906, May 2008
- [7] M. P. Li, *Jitter, Noise, and Signal Integrity at High-Speed*, Prentice Hall, 2007
- [8] ITRS. *The International Technology Roadmap for Semiconductors*, 2007 Edition
- [9] IEEE 802.3 Ethernet Working Group. <http://www.ieee802.org/3/>
- [10] Altera Corporation. *Mercury Programmable Logic Device Family Data Sheet*, San Jose, California, January 2003
- [11] Altera Corporation. *Stratix IV Device Datasheet*, December 2008  
[http://www.altera.com/literature/hb/stratix-iv/stx4\\_5v4\\_01.pdf](http://www.altera.com/literature/hb/stratix-iv/stx4_5v4_01.pdf)

- [12] Xilinx, Inc. *Introducing Virtex-6 and Spartan-6 FPGA Families*,  
<http://www.xilinx.com/products/v6s6.htm>
- [13] Texas Instruments Incorporated <http://www.ti.com>
- [14] Cisco Systems Inc. <http://www.cisco.com>
- [15] P. Noel, F. Zarkeshvari and T. Kwasniewski, "Recent Advances in High-Speed Serial I/O Trends, Standards and Techniques," *Proceedings of 18th Canadian Conference on Electrical and Computer Engineering*, 2005
- [16] H. Johnson and M. Graham, *High-Speed Signal Propagation Advanced Black Magic*, Prentice Hall PTR, 2003
- [17] A. Hajimiri and T. H. Lee, *The Design of Low Noise Oscillators*, Kluwer Academic Publishers, 1999
- [18] T. Miyazaki, M. Hashimoto and H. Onodera, "A Performance Prediction of Clock Generation PLLs: A Ring Oscillator Based PLL and an LC Oscillator Based PLL," *IEICE Transactions on Electronics* 2005 E88-C (3): 437-444
- [19] Altera Corporation, *Innovating with a Full Spectrum of 40-nm FPGAs and ASICs with Transceivers*, white paper
- [20] P. Patra, "On the Cusp of a Validation Wall," *IEEE Design & Test*, volume 24, Issue 2, PP.193-196, Mar.-Apr. 2007
- [21] Altera Corporation, *The Evolution of High-Speed Transceiver Technology*, White Paper, San Jose, California, 2002
- [22] Serial ATA International Organization: Serial ATA Revision 3.0. Gold Revision, June 2, 2009
- [23] National Committee for Information Technology Standardization (NCITS) T11.2/Project 1316-DT/Rev 3.1: "Fiber Channel – Methodologies for Jitter and Signal Quality Specification", October 2001
- [24] IEEE Draft P802.3ae/D3.3, "Supplement to Carrier Sense Multiple Access with Collision Detection (CSMA/CD) Access Method & Physical Layer Specifications," XGMII Extended Sublayer (XGXS) and 10 Gigabit Attachment Unit Interface (XAUI), October 2001
- [25] SATA-IO, Serial ATA International Organization. <http://www.sata-io.org/>

- [26] "Serial ATA: Meeting Storage Needs Today and Tomorrow - Introducing SATA 6Gb/s and the Serial ATA Revision 3.0 Specification," SATA-IO SATA Rev 3.0 Presentation, May 27-June 6, 2009. <http://www.serialata.org/documents/SATA-Rev-30-Presentation.pdf>
- [27] "Economic Crisis Response: Worldwide 2008-2012 Forecast Update," IDC Doc #215614, December 2008
- [28] E. A Newcombe and S. Pasupathy, "Error Rate Monitoring for Digital Communications," *Proceedings of the IEEE*, volume 70, Issue: 8, Aug.1982, pp.805-828
- [29] D.H. Wolaver, "Measure Error Rate Quickly and Accurately," *Electronic Design*, pp.89-98, May 30, 1995
- [30] S. Berber, "An Automated Method for BER Characteristics Measurement," *IEEE Transactions on Instrumentation and Measurement*, VOL. 53, No. 2, April 2004
- [31] A. Papoulis, *Probability, Random Variables, and Stochastic Processes*, New York: McGraw-Hill, 1984
- [32] K. S. Shanmugan and A.M. Breipohl, *Random Signals: Detection, Estimation, and Data Analysis*, New York, John Wiley and Sons, 1988
- [33] Maxim Integrated Products, Inc. *HFTA-05.0: Statistical Confidence Levels for Estimating Error Probability*, Application Notes, 2007
- [34] Y. Cai, S. Werner, G. Zhang, M. Olsen, and R. Brink, "Jitter Testing for Multi-gigabit Backplane SerDes – Techniques to Decompose and Combine Various Types of Jitter," *Proceedings of IEEE International Test Conference*, 2002, p700-709
- [35] John Patrin and Mike Li, "Comparison and Correlation of Signal Integrity Measurement Techniques," DesignCon 2002
- [36] "Jitter Fundamentals," Wavecrest Corporation, Rev.1. July 6, 2005. [http://www.wavecrest.com/technical/pdf/jittfun\\_hires\\_sngls.pdf](http://www.wavecrest.com/technical/pdf/jittfun_hires_sngls.pdf)
- [37] A. Kuo, T. Farahmand, N. Ou, S. Tabatabaei, and A. Ivanov, "Jitter Models and Measurement Methods for High-Speed Serial Interconnects," *Proceedings of IEEE International Test Conference*, 2004
- [38] J. G. Proakis, *Digital Communications*, McGraw-Hill High Education, 2001
- [39] GigOptix, <http://www.gigoptix.com>.

- [40] B. Laquai and Y. Cai "Testing Multilane Gigabit SerDes Interfaces with Jitter Injection," *Proceedings of IEEE International Test Conference*, 2001
- [41] M. Hafeed, D. Watkins, C. Tam, and B. Pishdad, "Massively Parallel Validation of High-speed Serial Interfaces Using Compact Instrument Modules," *Proceedings of IEEE International Test Conference*, 2006
- [42] D.C. Keezer, D. Minier, and P. Ducharme, "Source-Synchronous Testing of Multilane PCI Express and HyperTransport Buses," *IEEE Design & Test of Computers*, January 2006
- [43] <http://www.advantest.de/dasat/index.php?cid=100354&conid=100984&>
- [44] S. Sunter and A. Roy, "Structural Tests for Jitter Tolerance in SerDes Receivers," *Proceedings of IEEE International Test Conference*, 2005
- [45] M. S. Toden, *Analog and Digital Communication Systems*, Discovery Press, Los Angeles, California, 2001
- [46] The MathWorks, Inc. Natick, Massachusetts. <http://www.mathworks.com>
- [47] A. Gazel, E. Boutillon, J.L. Danger, G. Gulak, and H. Lamaari, "Design and Performance Analysis of a High Speed AWGN Communication Channel Emulator," *Proceedings of IEEE PACRIM Conference*, Aug. 2001
- [48] Altera Corporation, San Jose, California, <http://www.altera.com>
- [49] Xilinx, Inc. San Jose, California, <http://www.xilinx.com>
- [50] M. Courtoy, "Rapid System Prototyping for Real-time Design Validation," *Proceedings of Ninth International Workshop on Rapid System Prototyping*, 1998, pp. 108-112
- [51] T. Matsumura, N. Yamanaka, T. Yamaguchi, and K. Ishikawa, "Real-time emulation Method for ATM Switching Systems in Broadband ISDN," *Proceedings of seventh IEEE International Workshop*, Jun 1996
- [52] Wai-Kei Mak and D. F. Wong, "Board-level Multiterminal Net Routing for FPGA-based Logic Emulation," *ACM Transactions on Design Automation of Electronic Systems (TODAES)*, April 1997
- [53] J. Chen, J. Moon and K. Bazargan, "A Reconfigurable FPGA-Based Readback Signal Generator for Hard-Drive Read Channel Simulator," *Proceedings of ACM/IEEE Design Automation Conference*, June 10-14, 2002

- [54] C. Change, K. Kuusilinna, B. Richards and R.W. Brodersen, "Implementation of BEE: a Real-time Large-scale Hardware Emulation Engine," *Proceedings of the International Symposium on Field programmable Gate Arrays*, February 2003
- [55] Agilent Technologies, Agilent 81200 Data Generator/Analyzer Data sheet, 2002
- [56] Anritsu Corporation, 48 Gb/s BER Test System Datasheet. Atsugi-shi, Kanagawa, Japan, 2002
- [57] M. F. Schollmeyer and W. H. Tranter, "Noise Generators for the Simulation of Digital Communication Systems," *Proceedings of the 24th Annual Simulation Symposium*, April 1-5, 1991, pp. 264 – 275
- [58] P. Kabal, "Generating Gaussian Pseudo-random Deviates", Tech. Rep., Department of Electrical and Computer Engineering, McGill University, 2000
- [59] D. B. Thomas, W. Luk, P. Leong, and J. D. Villasenor, "Gaussian Random Number Generators," *ACM Computing Surveys*, Vol. 39, No. 4, October 2007
- [60] Xilinx Inc., "Additive White Gaussian Noise (AWGN) Core v1.0", Production Specification, Oct. 2002
- [61] D. Lee, W. Luk, J. Villasenor, and P. Y. K. Cheung, "A Gaussian Noise Generator for Hardware-Based Simulators," *IEEE Transactions on Computers*, Vol. 53, No. 12, December 2004
- [62] A. Alimohammad, B.F. Cockburn, and C. Schlegel, "An iterative hardware Gaussian noise Generator," *Proceedings of IEEE Pacific Rim Conference on Communications, Computers and Signal Processing*, Aug. 2005
- [63] A. Alimohammad, S.F. Fard, B.F. Cockburn, and C. Schlegel, "A compact and accurate Gaussian Variate Generator," *IEEE Transactions on Very Large Scale Integration (VLSI) Systems*, Vol.16, No.5, May 2008
- [64] P. Atinirarnit, Design and implementation of an FPGA-based adaptive filter single-use receiver, M. Sc. Thesis, Virginia Polytechnic Institute, 1999
- [65] D. E. Knuth, *The Art of Computer Programming*, Addison-Wesley, 1998
- [66] S. Aouini and G. W. Roberts, "A Predictable Robust Fully Programmable Analog Gaussian Noise Source for Mixed-Signal/Digital ATE," *Proceedings of IEEE International Test Conference*, 2006

- [67] Y. Fan and Z. Zilic, "A Novel Scheme of Implementing High Speed AWGN Communication Channel Emulators in FPGAs," *Proceedings of 2004 International Symposium on Circuits and Systems*, Volume: 2, 23-26, May 2004
- [68] Henry H. Y. Chan and Zeljko Zilic, "Modeling Simultaneous Switching Noise-Induced Jitter for System-on-Chip Phase-Locked Loops," *Proceedings of ACM/IEEE Design Automation Conference*, June 2007
- [69] Y. Cai, B. Laquai, and K. Luehman, "Jitter Testing for Gigabit Serial Communication Transceivers," *IEEE Design & Test of Computers*, Vol. 19, Issue 1, Jan, 2002
- [70] "Fibre Channel - Methodologies for Jitter and Signal Qualify Specification - MJSQ Technical Report, Revision 12.2," Ed. Bill Hamn, January 2004
- [71] M. Li, "Statistical and System Approaches for Jitter, Noise, and Bit Error Rate (BER) Tests for High Speed Serial Links and Devices," *Proceedings of IEEE International Test Conference*, 2005
- [72] S. Sunter and A. Roy, "A Self-Testing BOST for High-Frequency PLLs, DLLs and SerDes," *Proceedings of IEEE International Test Conference*, 2007
- [73] R. Walker, "Designing Bang-bang PLLs for Clock and Data Recovery in Serial Data Transmission Systems," <http://www.omnisterra.com/walker/pdfs.papers/BBPLL.pdf> White Paper, 2003
- [74] Behzad Razavi, "Challenges in the Design of High-Speed Clock and Data Recovery Circuits," *IEEE Communication Magazine*, August 2002
- [75] D. Hong and K.T. Cheng, "Bit-Error Rate Estimation for Bang Bang Clock and Data Recovery Circuitry in High-Speed Serial Links," *Proceedings of 26th IEEE VLSI Test Symposium*, 2008
- [76] Working Draft American National Standard, Serial Attached SCSI-2 (SAS-2), Revision 5a, 21 July 2006
- [77] T. Palkert, "SFI-5 Proposed Electrical Specifications," Optical Internetworking Forum (OIF2001.033), January 2001
- [78] "High Frequency Serial Communication: Technology Requirement", Test and Test Equipment Section, ITRS: International Technology Roadmap for Semiconductors, Nov, 2004

- [79] D.C. Keezer, J.S. Davis, S. Bezos, D. Minier, M.C. Caron, K. Bergman, and O. Liboiron-Ladouceur, Low-Cost Strategies for Testing Multi-Gigahertz SOPs and Components, *Proceedings of IEEE 5th Electronics Packaging Technology Conference*, 2003
- [80] M. Li and J. B. Wilstrup, "On the Accuracy of Jitter Separation from Bit Error Rate Function," *Proceedings of IEEE International Test Conference*, 2002, p710-716
- [81] P. R. Trischitta and E. L. Varma, *Jitter in Digital Transmission Systems*, Artech House, 1989
- [82] Bellcore, SONET OC-192 Transport System Generic Criteria, GR-1377-CORE, Issue 5, 1998
- [83] T.J. Yamaguchi, M. Soma, M. Ishida, H. Musha, and L. Malarsie, "A New Method for Testing Jitter Tolerance of SerDes Devices Using Sinusoidal Jitter," *Proceedings of IEEE International Test Conference*, 2002
- [84] Teradyne, Inc. <http://www.teradyne.com>
- [85] H. Werkmann, "Enabling the PCI Express Ramp - ATE Based Testing of PCI Express Architecture," Euro DesignCon 2004 Also available at [www.verigy.com](http://www.verigy.com)
- [86] Y. Cai, A. Bhattacharyya, J. Martone, A. Verma, and W. Burchanowski, "A Comprehensive Production Test Solution for 1.5GB/S and 3GB/S Serial-ATA," *Proceedings of IEEE International Test Conference*, 2005
- [87] Y. Cai, T. P. Warwick, S. G. Rane, and E. Masserrat, "Digital Serial Communication Device Testing and Its Implications on Automatic Test Equipment Architecture," *Proceedings of IEEE International Test Conference*, 2000
- [88] E.S. Erdogan and S. Ozev, "A Robust, Self-tuning CMOS Circuit for Built-in Go/No-Go Testing of Synthesizer Phase Noise," *Proceedings of IEEE International Test Conference*, 2006
- [89] E.S. Erdogan and S. Ozev, "An ADC-BiST Scheme Using Sequential Code Analysis," *Proceedings of the conference on Design, Automation and Testing in Europe*, 2007
- [90] M. Li and J. Chen, "New Methods for Receiver Internal Jitter Measurements," *Proceedings of IEEE International Test Conference*, 2007

- [91] Tektronix, "Jitter Measurement and Timing Analysis," Product guideline, [http://www.tek.com/applications/serial\\_data/jitter.html](http://www.tek.com/applications/serial_data/jitter.html)
- [92] Agilent Technologies, "Jitter Solutions for Telecom, Enterprise, and Digital Designs," Cooperate literature, <http://cp.literature.agilent.com/litweb/pdf/5988-9592EN.pdf>
- [93] B.A. Ward, K. Tan, and M.L. Guenther, "Apparatus and Method for Spectrum Analysis-Based Serial Data Jitter Measurement," US Patent No. 6832172, issued on December 14, 2004
- [94] W. Dalal and D. Rosenthal, "Measuring Jitter of High Speed Data Channels Using Undersampling Techniques," *Proceedings of IEEE International Test Conference*, 1998
- [95] M. Li, J. Wilstrup, R. Ressen and D. Petrich, "A New Method for Jitter Decomposition through Its Distribution Tail Fitting," *Proceedings of IEEE International Test Conference*, 1999
- [96] S. Sunter, A. Roy, and J. Cote, "An Automated, Complete, Structural Test Solution for SERDES," *Proceedings of IEEE International Test Conference*, 2004
- [97] A. H. Chan and G. W. Roberts, "A Jitter Characterization System Using a Component-Invariant Vernier Delay Line," *IEEE Transactions on VLSI Systems*, Volume 12, Issue 1, Jan. 2004
- [98] A. Meixner, A. Kakizawa, B. Provost, and S. Bedwani, "External Loopback Testing Experience with High Speed Serial Interfaces," *Proceedings of IEEE International Test Conference*, Oct. 2008
- [99] W. Fritzsche and A. Haque, "Low Cost Testing of Multi-GBit Device Pins with ATE Assisted Loopback Instrument," *Proceedings of IEEE International Test Conference*, Oct. 2008
- [100] G. Hansel, K. Stieglbauer, K. Schulze and J. Moreira, "Implementation of an Economic Jitter Compliance Test for a Multi-Gigabit Device on ATE", *Proceedings of IEEE International Test Conference*, 2004
- [101] Standard Error (Statistics) [http://en.wikipedia.org/wiki/Standard\\_error\\_\(statistics\)](http://en.wikipedia.org/wiki/Standard_error_(statistics))



- [102] "Standard Error of the Mean," material from Brighton Webs Ltd, statistical and data services for industry. [http://www.brighton-webs.co.uk/statistics/standard\\_error.asp](http://www.brighton-webs.co.uk/statistics/standard_error.asp)
- [103] M. Burns and G. W. Roberts, *An Introduction to Mixed-Signal IC Test and Measurement*, Oxford University Press, 2001
- [104] Analyzing Jitter Using a Spectrum Approach, Tektronix Application note
- [105] J. Dorsch, "The Softer Side of Test: Software Products to Star at International Test Conference," *Electronic News*, September 1999
- [106] S. Sunter, C. McDonald and G. Danialy, "Contactless Digital Testing of IC Pin Leakage Currents," *Proceedings of International Test Conference*, 2001
- [107] S. Sunter and A. Roy, "Purely Digital BIST for Any PLL or DLL," *Proceedings of European Test Symposium*, May 2007
- [108] R. Kiefer, *Test Solutions for Digital Networks*, Huthig GmbH, Heidelberg, 1998
- [109] S. Brown and Z. Vranesic, *Fundamentals of Digital Logic with VHDL Design*, McGraw-Hill Higher Education, 2000
- [110] Altera Corporation, Mercury Gigabit Transceiver MegaCore Function User Guide, February 2002
- [111] T. Yamaguchi, "Loopback or Not," *Proceedings of IEEE International Test Conference*, 2004, p. 1434
- [112] [http://en.wikipedia.org/wiki/Delay\\_line](http://en.wikipedia.org/wiki/Delay_line)
- [113] [http://www.maxim-ic.com/appnotes.cfm/an\\_pk/209](http://www.maxim-ic.com/appnotes.cfm/an_pk/209), "How Delay Lines Work," Application notes
- [114] K.W. Kobayashi, "A DC-40 GHz InP HBT Gilbert Multiplier," *Proceedings of IEEE Gallium Arsenide Integrated Circuit (GaAs IC) Symposium*, 25th Annual Technical Digest 2003
- [115] [http://www.gigoptix.com/pdf/whitepapers/Optical\\_Interconnection\\_rev6.pdf](http://www.gigoptix.com/pdf/whitepapers/Optical_Interconnection_rev6.pdf), "Semiconductor Technologies for Optical Interconnection, from Ultra Long Haul to Very Short Reach," white paper by GigOptix
- [116] [www.hikari-trading.com/opt/gigoptix/file/it4036/it4036\\_data.pdf](http://www.hikari-trading.com/opt/gigoptix/file/it4036/it4036_data.pdf), "iT4036 Wideband Phase Delay Preliminary Datasheet"

- [117] J. Moreira, H. Barnes and G. Hoersch, "Analyzing and Addressing the Impact of Test Fixture Relays for Multi-Gigabit ATE I/O Characterization Application," *Proceedings of IEEE International Test Conference*, 2007
- [118] D.C. Keezer, D. Minier, P. Ducharme, D. Viens, G. Flynn, and J.S. McKillop, "Multi-GHz Loopback Testing Using MEMS Switches and SiGe Logic," *Proceedings of IEEE International Test Conference*, October 2007
- [119] "TT1244: SPDT 265.GHz RF MEMS Switch", Data Sheet, TeraVista, [http://www.rapidtek.net/spec/mems/DS-TT1244\\_1.3.pdf](http://www.rapidtek.net/spec/mems/DS-TT1244_1.3.pdf)
- [120] "TeraVista Announces Availability of DC to 26.5 GHz SPDT MEMS Switch," Press Release, TeraVista Technologies, Inc., Austin, Texas, April 30, 2007. <http://news.thomasnet.com/fullstory/518285>
- [121] <http://www.teledynereleys.com/pdf/electromechanical/grf300grf303.pdf>, GRF300 Series data sheet
- [122] <http://www.teledynereleys.com/pdf/SurfacemountingGRF300.pdf>, "Surface Mounting GRF300 and GRF303 relays", Application Note
- [123] R. D'Agostino and M. Stephens, *Goodness-of-Fit Techniques*, Marcel Dekker Inc., 1986
- [124] D. Lee, W. Luk, J. Villasenor, G. Zhang and P. Leong, "A Hardware Gaussian Noise Generator Using the Wallace Method," *IEEE Transactions on Very Large Scale Integration (VLSI) Systems*, Vol. 13, No. 8, August 2005
- [125] D. Knuth, *The Art of Computer Programming, Seminumerical Algorithms*, 3rd Edition Ser. Addison-Wesley, 1997 Vol. 2
- [126] D. Ruppert, "What is Kurtosis? An Influence Function Approach," *The American Statistician*, Vol. 41, No. 1, pp. 1-5, Feb. 1987
- [127] D.N. Joanes and C.A. Gill, "Comparing Measures of Sample Skewness and Kurtosis," *Journal of the Royal Statistical Society (Series D): The Statistician* 47 (1), 183–189, 1998
- [128] <http://en.wikipedia.org/wiki/Kurtosis>
- [129] D. Lee, J. Villasenor, W. Luk and P. Leong, "A Hardware Gaussian Noise Generator Using the Box-Muller Method and Its Error Analysis," *IEEE Transactions on Computers*, 2006

- [130] D. C. Keezer, D. Minier and P. Ducharme, "Method for Reducing Jitter in Multi-Gigahertz ATE," *Proceedings of the Conference on Design, Automation and Test in Europe*, 2007, Pages 701-706
- [131] D. C. Keezer, C. Gray, A. Majid and P. Ducharme, "A Development Platform and Electronic Modules for Automated Test Up to 20Gbps," *Proceedings of IEEE International Test Conference*, 2009
- [132] M. Shimanouchi, "Periodic Jitter Injection with Direct Time Synthesis by SPP ATE for SerDes Jitter Tolerance Testing in Production," *Proceedings of IEEE International Test Conference*, 2003
- [133] M. Hafeed, N. Abaskharoun and G. W. Roberts, "A Stand-Alone Integrated Test Core for Time and Frequency Domain Measurements," *Proceedings of IEEE International Test Conference*, 2000
- [134] S. Tabatabaei, M. Lee and F. Ben-Zeev, "Jitter Generation and Measurement For Test of Multi-GBPS Serial IO," *Proceedings of IEEE International Test Conference*, 2004
- [135] J.S. Davis, D.C. Keezer, O. Liboiron-Ladouceur and K. Bergman, "Application and Demonstration of a Digital Test Core: Optoelectronic Test Bed and Wafer-level Prober," *Proceedings of IEEE of the International Test Conference*, 2003
- [136] M. Ishida, T. J. Yamaguchi, and Mani Soma, "A Method for Testing Jitter Tolerance of SerDes Receivers Using Random Jitter," DesignCon 2007
- [137] D.C. Keezer, J.S. Davis, M. Haris, S. Bezos, D. Minier, M.C. Caron, K. Bergman, and O. Liboiron-Ladouceur, "Recent Advances in Low-Cost Multi-GigaHertz Testing," *Proceedings of Napa KDG Packaging and Test Workshop*, 2003
- [138] C. Gray, O. Liboiron-Ladouceur, D.C. Keezer, and K. Bergman, "Co-Development of Test Electronics and PCI Express Interface for a Multi-Gbps Optical Switching Network," *Proceedings of IEEE International Test Conference*, 2007
- [139] B. R. Veillette and G. Roberts, "Reliable Analog Bandpass Signal Generation," *Proceedings of IEEE International Symposium on Circuits and Systems*, 1998
- [140] IEC 61280-2-8, "Fibre Optic Communication Subsystem Test Procedures – Digital Systems – Part 2-8: Determination of low BER using Q-factor Measurements," Feb 2003

- [141] K. Willox, "Q Factor: The Wrong Answer for Service Providers and Equipment Manufactures," *IEEE Communications Magazine*, Feb. 2003